# Probing Conventional and Unconventional Superconductivity by Ultra-Low-Temperature Scanning Tunneling Spectroscopy

**Anshu Sirohi**

**A thesis submitted for the partial fulfilment of the degree of**

**Doctor of Philosophy**


**Department of Physical Sciences**

**Indian Institute of Science Education and Research Mohali**

**July, 2019**

**Dedicated to**
**my parents, brother**
**and**
**husband**

# Declaration

The work presented in this thesis has been carried out by me in the guidance of Dr. Goutam Sheet at Indian Institute of Science Education and Research (IISER) Mohali. This work has not been submitted to any other institution or university in part or in full for a degree, a diploma, or a fellowship. Whenever contributions of others are involved, every effort is made to indicate this clearly, with due acknowledgment of collaborative research and discussions. This thesis is a bonafide record of original work done by me and all sources listed within have been detailed in the bibliography.

Date:
Place:

Anshu Sirohi (PH14021)
(Candidate)

In my capacity as the supervisor of the candidate's doctoral thesis, I certify that the above statements by the candidate are true to the best of my knowledge.

Dr. Goutam Sheet
(Supervisor)

**Acknowledgements**

A very special sincere gratitude goes to my supervisor, Dr. Goutam Sheet for his guidance and innovative support. I genuinely appreciate him for giving me the opportunity to work in this wonderful lab and for the continuous support in research work. I am really grateful to him for the efforts he made during scientific discussions related to my project. I would like to express my gratitude towards his endless motivation, for his patience and immense knowledge. His constant reassurance, endless encouragement, and valuable suggestion boosted me at each and every step of my research work. I really appreciate him for his never giving up attitude. His guidance helped me in all the time of research and writing of this thesis.

Besides my advisor, I would like to express my sincere gratitude to my doctoral committee members Dr. Yogesh Singh and Dr. Sanjeev Kumar for their insightful comments, encouragement and helpful discussions, and also for the hard questions which incented me to widen my research from various perspectives.

My sincere thanks also goes to my collaborators and coauthors in the publications: Dr. Tanmoy Das, Dr. Satyabrata Patnaik, Prof. Umesh V Waghmare, Dr. Yogesh Singh, Dr. Mukul Kabir, Prof. Ashok K Ganguli, Prakriti Neha, Surabhi Saha, Chandan K. Singh, Karn S. Jat, Vishal K. Maurya and Gohil S. Thakur for their support in the theoretical work and for providing the best quality crystals.

I appreciate the financial support provided by IISER Mohali. I would also like to acknowledge DST, CSIR and CICS India for providing partial financial support to attend the APS March Meeting-2017 and 2019 in the USA.

I am grateful to my fellow lab mates and former lab members in the group: Ritesh, Shekhar, Avtar Singh, Aslam, Gayen da, Shilpa di, Balal, Abhishek, Leena, Preetha, Lalit, Mrityunjay, Sandeep, Suman, Aashi, Mamta, Soumya, Aastha, Deepti, Monika, Veerpal and Soumyadip for their help during experimental measurement, scientific discussion and for all the fun we had in the lab.

I am also thankful to my friends Richa, Jyotsna, Namrata, Anzar, Amit, Shama, Gopal ji, Harleen, Shudhanshu, Avinash, Ankit, Arnob, Shalender, Sumit, Aman and Umang for making my years enjoyable at IISER Mohali. Also, I thank my friends Himanshi, Harshit, Rahul, Sanjeev, and Ravi outside the IISER. Special thanks go to Kavita, Manju, Vinshi, Sangeeta, and Pawan for always motivating me, I really loved your company.

My parents have always been there to support me to encourage me and to make me believe

that I can do. I would never be able to thank them for their efforts. I appreciate their unconditional love and support. My deepest appreciation to my younger brother for making crazy and joyful moment at home.

I wish to thank my father and mother for not being father-in-law and mother-in-law. I appreciate your understanding and freedom which you have given to me. Mukul, I can not thank you. Your understanding, patience and unconditional love really supports me a lot.

## List of publications:

1. Multi-band superconductivity driven by a site selective mechanism in $Mo_8Ga_{41}$,
   **Anshu Sirohi**, Surabhi Saha, Prakriti Neha, Shekhar Das, Satyabrata Patnaik, Tanmoy Das & Goutam Sheet, (Phys. Rev. B 99, 054503 (2019)) *Phys. Rev. B* 99, 054503 (2019).

2. Low-energy excitations and non-BCS superconductivity in $Nb_xBi_2Se_3$,
   **Anshu Sirohi**, Shekhar Das, Prakriti Neha, Karn S. Jat, Satyabrata Patnaik & Goutam Sheet *Physical Review B* 98, 094523 (2018).

3. Mesoscopic Superconductivity above 10 K in Silicon Point Contacts,
   **Anshu Sirohi**, Sirshendu Gayen, Mohammad Aslam & Goutam Sheet, *Applied Physics Letters* 113, 242601 (2018).

4. Mixed type I and type II superconductivity due to intrinsic electronic inhomogeneities in the type II Dirac semimetal $PdTe_2$,
   **Anshu Sirohi**, Shekhar Das, Priyo Adhikary, Rajeswari Roy Chowdhury, Amit, Yogesh Singh, Sirshendu Gayen, Tanmoy Das, & Goutam Sheet, *J. Phys. Condens. Matter* 31, 085701 (2019).

5. Transport spectroscopy on trapped superconducting nano-islands of Pb: signature of unconventional pairing,
   **Anshu Sirohi**, Preetha Saha, Sirshendu Gayen, Avtar Singh & Goutam Sheet *Nanotechnology* 27, 285701 (2016).

6. High spin polarization and the origin of unique ferromagnetic ground state in CuFeSb,
   **Anshu Sirohi**, Chandan K. Singh, Gohil S. Thakur, Preetha Saha, Sirshendu Gayen, Abhishek Gaurav, Shubhra Jyotsna, Zeba Haque, L. C. Gupta, Mukul Kabir, Ashok K. Ganguli & Goutam Sheet *Applied Physics Letters* 108, 242411 (2016).

7. Conventional superconductivity in the type-II Dirac semimetal $PdTe_2$,
   Shekhar Das, Amit, **Anshu Sirohi**, Lalit Yadav, Sirshendu Gayen, Yogesh Singh and Goutam Sheet *Physical Review B* 97, 014523 (2018).

8. Discovery of highly spin-polarized conducting surface states in the strong spin-orbit coupling semiconductor $Sb_2Se_3$,
   Shekhar Das, **Anshu Sirohi**, Gaurav Kumar Gupta, Suman Kamboj, Aastha Vasdev, Sirshendu Gayen, Prasenjit Guptasarma, Tanmoy Das & Goutam Sheet, *Physical Review B* 97, 235306 (2018).

9. Suppression of transport spin-polarization of surface states with emergence of ferromagnetism in Mn-doped $Bi_2Se_3$,
   Suman Kamboj, Shekhar Das, **Anshu Sirohi**, Rajeswari Roy Chowdhury, Sirshendu Gayen, Vishal K. Maurya, Satyabrata Patnaik & Goutam Sheet, *Journal of Physics: Condensed Matter* 30, 355001 (2018).

10. A series of s-block (Ca, Sr and Ba) metal–organic frameworks: synthesis and structure–property correlation,
    K. S. Asha, Madhuri Makkitaya, **Anshu Sirohi**, Lalit Yadav, Goutam Sheet & Sukhendu Mandal *CrystEngComm* 18, 1046 (2016).

11. Generation of strain-induced pseudo-magnetic field in a doped type-II Weyl semimetal,
    Suman Kamboj, Partha Sarathi Rana, **Anshu Sirohi**, Aastha Vasdev, Manasi Mandal, Sourav Malik, Ravi Prakash Singh, Tanmoy Das & Goutam Sheet, *Physical Review B* 100, 115105 (2019).

12. Enhanced, homogeneously type-II superconductivity in Cu-intercalated $PdTe_2$
    Aastha Vasdev, **Anshu Sirohi**, M K Hooda, C S Yadav & Goutam Sheet, *Journal of Physics: Condensed Matter* 32, 125701 (2019).

# Abstract

Primarily, in this thesis, the focus has been to study superconductivity in certain topologically non-trivial materials using scanning tunneling microscopy and spectroscopy (STM/STS). Scanning Tunneling Spectroscopy (STS) is a powerful tool to probe the quasi-particle density of states in a conducting solid. A spectral gap, if any, can thus be directly probed by this technique. We have used an ultra-low temperature (down to 300 mK) and ultra-high vacuum (10-11 mbar) STM to study the nature of pairing in some of the candidate exotic superconductors. The major results, procured in this work are highlighted below.

**Multiband superconductor $Mo_8Ga_{41}$**: $Mo_8Ga_{41}$ is a compound of endohedral gallide family and the compound of the highest critical temperature in the family. The highest critical temperature in this compound is a consequence of the competition between valence electron counts and the lattice structure variation. The high $T_c$ of $Mo_8Ga_{41}$ is, in fact, a deviation from the rules proposed by Mathias in terms of electron counts. We found clear and direct evidence of two gap superconductivity in $Mo_8Ga_{41}$. The electron-phonon coupling in this system is found to be weak.

**The type II Dirac semimetal $PdTe_2$:** $PdTe_2$ is known to be a material where topologically non-trivial bands and superconductivity co-exist. The recent observation of type II Dirac fermions in $PdTe_2$ indicates the possibility of non-trivial Cooper-pairing when this compound undergoes superconducting transition below 1.75 K. We have shown that despite such unique coexistence, the superconducting phase is, in fact, conventional BCS type in nature [Ref. Shekhar Das et al., Phys. Rev. B 97, 014523 (2018)]. The superconducting phase in $PdTe_2$ is further interesting because it also displays the distribution of critical fields on the surface where we observed domains of type I and type II superconductivity in the presence of magnetic fields. We show that such inhomogeneity in the superconducting phase is related to the electronic inhomogeneity in the normal state.

**A candidate topological superconductor $Nb_x$-$Bi_2Se_3$:** $Bi_2Se_3$ is a famous topological insulator. When $Bi_2Se_3$ is intercalated with elemental metals (e.g. Cu, Sr, and Nb) the resulting compound becomes superconductor with the critical temperatures of 3 K. Among all, $Nb_x$-$Bi_2Se_3$ (x = 0.25) is a stronger possible candidate for topological superconductivity. Here, through STM spectroscopy we show that the tunneling spectra deviate from a BCS-like behavior, and the tunneling conductance at low bias is large. Our results are in good agreement with the idea of topological superconductivity in $Nb_x$-$Bi_2Se_3$.

**Tip-induced superconductivity in silicon**: Surprisingly, when the STM tip makes metallic contact with the highly doped silicon crystal, a unique superconducting phase appears underneath the tip. The critical temperature of this phase was significantly higher ( 11 K). We employed Point-Contact Andreev Reflection (PCAR) spectroscopy for further investigation of superconducting phase in silicon and found that the superconductivity is conventional in nature

which thoroughly follows BCS theory.

**To justify the above works, we have chosen the following thesis plan:**

**Chapter I** is an introduction to the work presented in this thesis. This thesis deals with the superconducting phase of topologically trivial as well as non-trivial systems. This chapter highlights the main key points of BCS theory of superconductors for conventional superconductors and the discussion of topological insulators, Dirac and Weyl semimetals.

**Chapter II** describes the details of the experimental methods used to probe the superconducting phase of materials. The Scanning Tunneling Microscope (STM) is extensively used in most of the experiments in the work presented in this thesis. The experiments are carried out down to 300 mK temperatures with up to 11 T magnetic field. The sample preparation is done in-situ. Point Contact Andreev Reflection Spectroscopy (PCAR) is also employed in some of the experiments. All the experiments are carried out using a home-built point-contact probe down to 400 mK temperatures. A theoretical analysis part is also included in this chapter.

The main experimental observations of my research work as discussed above have been included as a chapter III, IV, V and VI respectively. At the end of this thesis, I will be discussing some of the important works carried out by me and included in the appendices (A and B).

# Contents


**1 Overview of superconductivity and topological materials** **1**

1.1 Introduction . . . 1

1.2 Basics of Superconductivity . . . 3

1.2.1 Zero resistance . . . 3

1.2.2 Meissner effect . . . 3

1.2.3 Conventional superconductors . . . 4

1.2.4 Characteristic length scales of superconductors . . . 7

1.2.5 Type II superconductors . . . 8

1.2.6 Unconventional superconductors . . . 10

1.3 Topological non-trivial systems . . . 11

1.3.1 Historical perspective . . . 11

1.3.2 Theoretical and experimental background of topological materials . . . 12

1.3.3 Dirac and Weyl semimetals . . . 14

1.3.4 Concept of topological equivalence . . . 16

1.3.5 Berry phase . . . 17

1.3.6 Topological invariants . . . 19

1.4 Topological superconductors . . . 19

**2 Experimental Techniques** **24**

2.1 Scanning Tunneling Microscope (STM) . . . 24

2.1.1 Working principle . . . 24

2.1.2 Theoretical description of quantum tunneling current . . . 25

2.1.3 Scanning Tunneling Spectroscopy (STS) . . . 26

2.2 Overview of Scanning Tunneling Microscope . . . 29

2.2.1 STM system and its components . . . 29

2.2.2 STM head/unit . . . 30

2.2.3 Electrochemical etching of metallic tip . . . 30

2.3 Point-contact spectroscopy technique . . . 35

2.3.1 Point-Contact Andreev Reflection Spectroscopy (PCAR): . . . . . 35
2.3.2 Electronic transport in different regimes . . . . . 36
2.3.3 Transport phenomena at the interface . . . . . 37
2.3.4 Measurement of transport spin polarization . . . . . 40
2.3.5 PCAR Spectroscopy measurement system . . . . . 42
2.4 Comparison between STS and PCAR Spectroscopy . . . . . 43
2.5 Conclusions . . . . . 44

**3 STM studies on gallide compound $Mo_8Ga_{41}$ 47**
3.1 Introduction . . . . . 47
3.2 Experimental details . . . . . 48
3.2.1 Sample Details . . . . . 48
3.2.2 Measurement Details . . . . . 48
3.3 STM/STS measurements on $Mo_8Ga_{41}$ . . . . . 49
3.3.1 Magnetic field dependence of $dI/dV$ vs. $dV$ spectrum . . . . . 51
3.3.2 Temperature dependence of $dI/dV$ vs. $dV$ spectrum . . . . . 52
3.4 Theoretical findings . . . . . 54
3.5 Summary . . . . . 58
3.6 Acknowledgements . . . . . 58

**4 Nature of superconductivity in $PdTe_2$ 61**
4.1 Introduction . . . . . 61
4.2 Experimental details and results . . . . . 62
4.2.1 Investigation of superconducting phase in magnetic fields . . . . . 63
4.2.2 Conductance mapping above the critical temperature . . . . . 64
4.2.3 Conductance mapping in presence of magnetic field . . . . . 66
4.2.4 Theoretical results . . . . . 67
4.3 Summary . . . . . 69
4.4 Acknowledgements . . . . . 69

**5 Unconventional superconductivity in $Nb_xBi_2Se_3$ 72**
5.1 Introduction . . . . . 72
5.2 Experimental details and results . . . . . 73
5.2.1 Sample details . . . . . 73
5.2.2 STM/STS results . . . . . 73
5.2.3 Tunneling Spectroscopy results . . . . . 75
5.2.4 Temperature and magnetic field dependence . . . . . 77
5.3 Summary . . . . . 80
5.4 Acknowledgements . . . . . 80

**6 Tip-induced superconductivity in silicon** **83**
6.1 Introduction . . . 83
6.2 Experimental details and results . . . 84
6.2.1 Sample details . . . 84
6.2.2 Point-contact spectroscopy . . . 85
6.2.3 Evolution of spectral features with temperature & magnetic field . . . 87
6.2.4 Observation of transport spin-polarization . . . 89
6.2.5 Other possibilities of superconducting phase . . . 89
6.3 Facet and carrier dependence of superconductivity in silicon . . . 91
6.3.1 Point contact spectroscopy on As-doped Si(100) . . . 93
6.3.2 Point contact spectroscopy on B-doped Si(100) . . . 95
6.3.3 TISC on Silicon with other metallic tips . . . 99
6.4 Summary . . . 101

**A Indication of unconventional superconducting pairing in Pb nano-islands** **104**
A.1 Introduction . . . 104
A.2 Experimental details and results . . . 105
A.3 Conclusions . . . 110

**B High spin-polarization in CuFeSb** **113**
B.1 Introduction . . . 113
B.2 Experimental results . . . 114
B.3 Theoretical calculations . . . 116
B.4 Conclusions . . . 119
B.5 Acknowledgements . . . 119

# List of Figures


1.1 superconducting transition of mercury . . . 3
1.2 Exclusion of magnetic field by a superconductor . . . 4
1.3 Type II superconductor . . . 9
1.4 Schematic of band gap . . . 13
1.5 Weyl chirality . . . 15
1.6 type II Dirac/Weyl cone . . . 15
1.7 Topology . . . 16

2.1 Schematic of STM . . . 25
2.2 Silicon topography with both bias . . . 27
2.3 Tunneling spectrum measured on superconducting Pb . . . 28
2.4 Overview of STM unit . . . 29
2.5 Piezo-tube scanner . . . 30
2.6 Tip etching system . . . 31
2.7 SEM image of resulting tip . . . 32
2.8 Schematic of tip cleaning . . . 33
2.9 A picture of sample cleaving stage . . . 34
2.10 Schematic of PCS . . . 35
2.11 Schematic of PCAR . . . 38
2.12 Schematic of spin-polarized PCAR spectroscopy . . . 40
2.13 Schematic of PCAR . . . 41
2.14 Picture of PCAR system . . . 42

3.1 Crystal structure of $Mo_8Ga_{41}$ . . . 48
3.2 Topography of $Mo_8Ga_{41}$ . . . 50
3.3 Two superconducting gaps in a single spectrum . . . 50
3.4 Two clear superconducting gaps in a single spectrum . . . 51
3.5 H dependence of $dI/dV$ vs. $dV$ spectrum . . . 52
3.6 Temperature dependence of $dI/dV$ vs. $dV$ spectrum . . . 52

3.7 Band structure and density of states . . . 55
3.8 3D Fermi surface of $Mo_8Ga_{41}$ . . . 55

4.1 Topography of $PdTe_2$ . . . 62
4.2 Temperature dependence of the tunneling spectrum . . . 62
4.3 Magnetic field dependence of tunneling spectra . . . 63
4.4 Conductance spectra in presence of magnetic field . . . 64
4.5 Conductance imaging in the normal state of $PdTe_2$ . . . 65
4.6 Conductance mapping in presence of magnetic field . . . 67
4.7 Computed values for the GLAG parameter . . . 68

5.1 Crystal structure of $Nb_xBi_2Se_3$ . . . 73
5.2 Atomic resolution images of $Nb_xBi_2Se_3$ . . . 74
5.3 Dirac cone of $Nb_xBi_2Se_3$ . . . 75
5.4 Tunneling spectra along a line of $Nb_xBi_2Se_3$ . . . 76
5.5 Tunneling spectra with fits of $Nb_xBi_2Se_3$ . . . 77
5.6 Temperature and magnetic field dependence of tunneling spectrum of $Nb_xBi_2Se_3$ 78
5.7 Multiple kinds of tunneling spectrum measured on $Nb_xBi_2Se_3$ . . . 79

6.1 STM imaging and tunneling spectroscopy . . . 84
6.2 $H$-dependence of $R-T$ of Silicon/metal point-contact . . . 85
6.3 transport spectroscopy in metallic regime . . . 86
6.4 Spectroscopic comparison with Pb point-contacts . . . 87
6.5 H and T-dependence of spectroscopy . . . 88
6.6 Transport spin-polarization in Silicon point-contacts . . . 89
6.7 H-dependence of R-T . . . 92
6.8 Point-contact spectroscopic results on As-doped silicon . . . 94
6.9 Point-contact spectroscopic results on B-doped silicon . . . 96
6.10 H-dependence of thermal contribution to I-V characteristics . . . 97
6.11 H and T-dependence of point-contact spectra and transport spin-polarization . . . 98
6.12 Point-contact spectroscopy with Cobalt tip . . . 99
6.13 H and T-dependence of spectra of silicon/Cobalt point-contacts . . . 100
6.14 Point-contact spectroscopy with Pt-Ir tip . . . 100

A.1 Spectroscopy in all regimes of point-contact . . . 105
A.2 Asymmetry in thermal regime spectrum . . . 106
A.3 3D plot of $dV/dI$ spectra . . . 107
A.4 H-dependence of $R$-$T$ and corresponding $H$-$T$ plot . . . 107
A.5 Nb point-contact spectra . . . 109

B.1 Point-contact spectra using Nb and Pb tips . . . 115

B.2 $P_t$ vs Z plot . . . . . 116
B.3 Theory figure . . . . . 118

# List of Tables

B.1 Refined structural parameters for CuFeSb obtained at 300K, which is below the ferromagnetic transition temperature. The number in the square bracket indicates the number of symmetric bond lengths. . . . . 117

Chapter 1

# Overview of superconductivity and topological materials

## 1.1 Introduction

Since the last century, superconductivity has been the most fascinating area of fundamental research in condensed matter Physics. Superconductivity in materials leads to the flow of current without any resistance. After the discovery of superconductivity, it was thought and experimentally realized that some of the elemental metals can become superconductor when they cooled below a certain temperature. Superconductivity in materials is governed by a complex quantum process. In most of the elemental superconductors and their alloys superconductivity is well understood within the framework of mean field theory that was developed by Bardeen, Cooper, and Schrieffer (BCS) in 1952. [1] Within this theory, the electrons form Cooper pairs and superconductivity happens when all the Cooper pairs in a material condense into a single quantum ground state where the phase of all the Cooper pairs become identical and a gap is created between the condensate and the single quasi-particle states. One of the basic assumptions involved in this theory is that the gap function in the quasiparticle density of states is isotropic in the momentum space. This theory has been very successful and most of the superconductors with low critical temperatures have been described well within this theory. Such superconductors are generally known as conventional superconductors. [2] There are many other classes of superconductors where Cooper-pairing is not accomplished by the interaction of charge carriers with the crystal lattice like in the high $T_c$ superconductors. Because of the unconventional Cooper pairing the superconducting gap function found to be anisotropic. The quantum mechanism of Cooper-pairing in such materials is not explained within the BCS theory. [1]

Moreover, the extensive research in superconductivity has been triggered by following the discovery of topological materials such as topological insulators [3], Dirac and Weyl semimetals. The topological materials host relativistic Dirac fermions as a quasi-particle excitation on their surface/edges [4]. It is believed that the emergence of superconductivity in topologically

non-trivial materials leads to the existence of highly searched relativistic particle Majorana fermions. In fact, in the past attempts were made to realize such topological superconducting phases in topological insulators and semimetals. For example, by doping or applying pressure on topological materials, fabricating heterostructures of topological material and superconductors to induce proximity effect [5] and by making point-contacts on a topological crystalline insulator, Dirac or Weyl semimetals. However, in such systems, while a superconducting phase could be achieved and there are some shreds of evidence also which claim the existence of Majorana fermions [6] but still a clear manifestation of topological superconductivity remained an unobtainable goal. More scientific efforts are required in this direction of research as the exotic excitations that emerge in topological superconductors are most important and interesting for future applications such as in fault-tolerant quantum computing. [7]

First I will begin with the introduction of superconductivity and discuss briefly by considering the main assumptions of BCS theory.

## 1.2 Basics of Superconductivity

Zero resistance and complete expulsion of the magnetic flux from the interior of the materials are the trademarks of the superconductivity. Kammerlingh Onnes discovered a sudden drop to zero in the resistivity of Mercury (Hg) at 4.2 K. [8] This was the first experiment to realize a superconducting phase and was awarded by a Nobel prize. The temperature at which the materials go to zero resistance state is called the critical temperature ($T_C$). Subsequently, this phenomenon was observed in a number of elemental metals and alloys. A microscopic theory explaining the complex quantum process which leads to the superconducting state is proposed by Bardeen, Cooper, and Schrieffer in 1957 known as BCS theory of superconductivity. [1]

### 1.2.1 Zero resistance

In 1911, Heike Kamerlingh Onnes discovered an absolute zero resistance state of Mercury (Hg). [8] This is one of the most important signatures of a superconductor which is shown in figure 1.1.

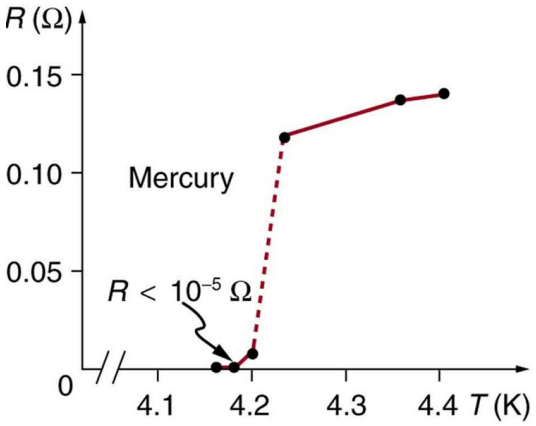


Figure 1.1: First material (Mercury) which shows superconducting transition at 4.2 K in R-T curve. (Image credit: Wikipedia)

### 1.2.2 Meissner effect

Another hallmark of superconductors is the perfect diamagnetism below their critical temperatures. When a material is placed in a small magnetic field below its critical temperature it expels all the magnetic flux from its interior. This phenomenon is called the Meissner effect first observed by W. Meissner and R. Ochsenfeld [9].

When a material goes through the superconducting transition in the presence of a weak magnetic field, it expels all the magnetic flux from the inside of the superconductor by introducing surface current. This effect is a unique property of a superconductor, which cannot be

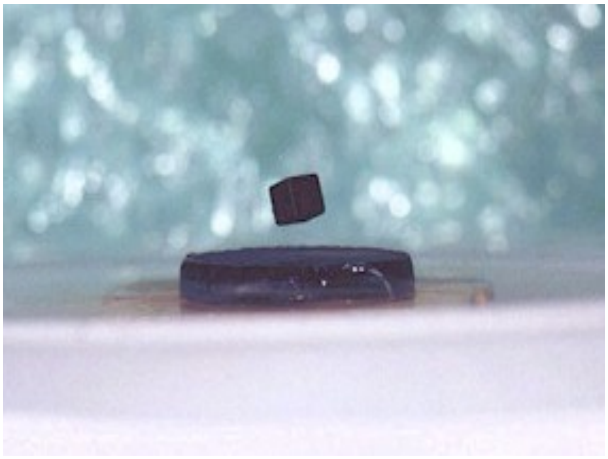

Figure 1.2: A picture showing the exclusion of magnetic field (Meissner effect) in the superconducting state under weak magnetic field. (Image credit: Wikipedia)

described by considering only a perfect conductor with zero resistivity. The electrical conductivity of a superconductor is infinite, which leads to a dissipationless current to flow forever.

### 1.2.3 Conventional superconductors

First successful microscopic mean field theory of superconductivity was proposed by Bardeen, Cooper, and Schrieffer (BCS) in 1957. Within this theory, in superconductors, electrons of opposite momentum form Cooper pairs and condense into a single ground state. In order to make Cooper pair, there should be something which can make two electrons attract each other. According to BCS theory, electron-lattice-electron interaction leads to an attractive force between two electrons. The indirect interaction builds up when one electron deforms the lattice by interacting it, the other electron takes this advantage and adjust itself to minimize the energy of the system which causes a correlation between these two electrons and leads to a weak attractive force between the two. Therefore, el-ph interaction is the main cause of superconductivity in conventional superconductors.

After the discovery of various superconductors like elemental metals and alloys it has been seen that the superconducting critical temperature depends on the different isotopes of the same material such as Hg (Mercury) has many isotopes and the critical temperature for all the isotopes is different. [10] The dependence of critical temperature on the isotopes of material confirms that the electron-phonon coupling is responsible to the superconducting mechanism. The second-order correction in the total Hamiltonian including a weak electron-phonon interaction provides a negative correction to the energy. [11] The total Hamiltonian can be written as

$$H = H_{el} + H_{ph} + H_{el-ph}$$

The Hamiltonian for electron-phonon interaction is

$$H_{el-ph} = \Sigma_{k,q}\, M_q\, a^{\dagger}{}_{k+q}\, a_k\, (b_q + b^{\dagger}{}_{-q})$$

where, $a_k^\dagger$, $a_k$ are the creation and annihilation operators and $a_{k+q}^\dagger$ is the creation operator of electrons after emitting a phonon of momentum q. $b_q$ and $b_{-q}^\dagger$ are the phonon absorption and emission operators. $M_q$ is the electron-phonon coupling coefficient. After the correction the effective Hamiltonian becomes

$$H_{eff} = H_o + \Sigma_{k,q} |M_q|^2 \, a^\dagger_{k+q} \, a^\dagger_{k'-q} a_{k'} \, a_k \, [\frac{\hbar\omega_q}{(\varepsilon_{k'}-\varepsilon_{k'-q})^2-(\hbar\omega_q)^2}]$$

$\omega_q$ is the phonon frequency. Now, the second term of the effective Hamiltonian will be negative if $(\varepsilon_{k'} - \varepsilon_{k'-q}) < (\hbar\omega_q)$ and the electrons experience a net attractive force. In general, $\varepsilon_{k'}$ and $\varepsilon_{k'-q}$ vastly exceed $\hbar\omega_q$. This k-space attraction allow electrons to attach together with the energy less than their non-interacting counterparts. This attraction is the basis of superconductivity.

$$V(k',q) = \frac{|M_q|^2\hbar\omega_q}{(\varepsilon_{k'} - \varepsilon_{k'-q})^2 - (\hbar\omega_q)^2} \tag{1.1}$$

where, $q = k - k'$, and phonon frequency $\omega_q$ is proportional to q. Therefore, for $\hbar\omega_q$ to be maximum q should be large enough. The maximum value q can have is 2k when $k' = -k$. This indicates that the coupling of momentum k with -k will be much favorable to get the strong attractive interaction between electrons and to condense in to the minimum energy state.

In BCS theory, the ground state wave function of cooper-pairs is given by

$$|\psi_{BCS}> = \Pi_{\vec{k}}(u_k + v_k \, c^\dagger_{k\uparrow} \, c^\dagger_{-k\downarrow})|0> \tag{1.2}$$

where $|0\rangle$ is the vacuum state and $c^\dagger_{k\uparrow}$, $c^\dagger_{-k\downarrow}$ are the single electron operators which create an electron with momentum $k$ and $-k$, while $v_k^2$ is the probability of pair occupancy and $u_k^2$ = 1- $v_k^2$ is the probability of pair vacancy.

Since the electrons form Cooper-pairs, an energy gap is formed between the ground state of the superconductor and the energy of the quasi-particle excitation. This energy gap is known as the superconducting energy gap of a superconductor. At temperature T = 0, the function of the superconducting energy gap in terms of momentum k is given as,

$$\Delta_{\vec{k}} = -\frac{1}{N}\sum_{k'} V_{\vec{k}\vec{k'}} < c^\dagger_{k\uparrow} \, c^\dagger_{-k\downarrow} > \tag{1.3}$$

Where $V_{kk'}$ is the electron-electron attractive interaction energy.

The elementary excitations in a superconductor are not electrons or holes as in a normal metal but more complicated objects known as Bogoliubons. For these excitations, Bogoliubov defined a creation operator in terms of electron creation and annihilation operators [12] as

$$\gamma_{\vec{k}\uparrow} = u_{\vec{k}} c_{k\uparrow} - v_{\vec{k}} c^{\dagger}_{-k\downarrow} \tag{1.4}$$

$$\gamma^{\dagger}_{-\vec{k}\downarrow} = u^{*}_{\vec{k}} c^{\dagger}_{-k\downarrow} + v^{*}_{\vec{k}} c_{k\uparrow} \tag{1.5}$$

$\gamma_{\vec{k}\uparrow}$ destroy an electron with $\vec{k}\uparrow$ and creates one with $-\vec{k}\downarrow$, similarly $\gamma^{\dagger}_{-\vec{k}\downarrow}$ creates an electron with $-\vec{k}\downarrow$ and destroys one with $\vec{k}\uparrow$. In the normal state, creating a bogoliubon excitation corresponds to creating one electron and one hole. In the superconducting state, a bogoliubon becomes superposition of both electron and hole state. The BCS ground state therefore corresponds to the vacuum of Bogoliubons $\gamma_{k\sigma}|\psi_{BCS}\rangle = 0$. These excitations follow Fermi-Dirac distribution

$$< \gamma^{\dagger}_{k'\uparrow}\gamma_{k'\uparrow} > = < \gamma^{\dagger}_{-k'\downarrow}\gamma_{-k'\downarrow} > = \frac{1}{e^{\beta E_{k'}}+1}$$

$u_k$ and $v_k$ are

$$|u_k|^2 = \frac{1}{2}\left[1 + \frac{\varepsilon_k}{\sqrt{{\varepsilon_k}^2 + |\Delta_k|^2}}\right]$$

and

$$|v_k|^2 = \frac{1}{2}\left[1 - \frac{\varepsilon_k}{\sqrt{{\varepsilon_k}^2 + |\Delta_k|^2}}\right]$$

by putting $u_k$ and $v_k$ and using Bogoliubons transformation and Fermi-Dirac statistics the expression of the superconducting energy gap can be obtained

$$\Delta_0 = 2\hbar\,\omega_D\, e^{-\frac{1}{V_0\rho_F}} \tag{1.6}$$

and expression for critical temperature of superconductors can be obtained for which $\Delta \neq 0$

$$T_c = 1.14 \frac{\varepsilon_D}{k_B} e^{-\frac{1}{V_0 \rho_F}} \tag{1.7}$$

Since, we know the $\Delta_0$ and $T_c$, $\Delta_0/k_B T_c$ ratio can be calculated as

$$\frac{\Delta_0}{k_B T_c} = 1.76$$

this ratio is true for most of the conventional superconductors called the BCS limit of conventional superconductors. For weak coupling superconductors, this ratio falls between 1.5 to 2.25. Most of the elemental materials or alloys in which the order parameter is well defined within the BCS theory are known as conventional superconductors. Generally, low-temperature superconductors are conventional in nature.

### 1.2.4 Characteristic length scales of superconductors

In 1935, after the discovery of superconductivity, London brothers F. and H. London proposed a simpler theory to explain the Meissner effect. [12] They introduced two basic electrodynamic equations as

$$E = \frac{4\pi\lambda_L^2}{c^2} \frac{\partial J_s}{\partial t} \tag{1.8}$$

$$H = -\frac{4\pi\lambda_L^2}{c^2} (\nabla \times J_s) \tag{1.9}$$

where, $n_s$ is considered as the number density of superconducting electrons and $\lambda_L$ is the penetration depth. When the second London's equation combined with the Maxwell equation $\nabla \times H = 4\pi J/c$, the resultant equation $\nabla^2 H = H/\lambda^2$ implies that the magnetic field decays exponentially with the penetration depth inside a superconductor. This is how, it explains the Meissner effect. The empirical temperature dependence of $\lambda(T)$ is described by

$$\lambda(T) = \lambda(0)[1 - (T/T_c)^4]^{-1/2}$$

The penetration depth is the characteristic length of a superconductor

$$\lambda_L(0) = \left(\frac{mc^2}{4\pi n_s e^2}\right)^{\frac{1}{2}} \tag{1.10}$$

$\lambda_L(0)$ is an ideal theoretical limit as $T \to 0$. Experimental observations of penetration depth reveals that the actual measured penetration depth is always larger than $\lambda_L(0)$. The quantitative explanation of this larger penetration depth is given by Pippard by the introduction of Pippard's coherence length $\xi_o$. By considering the uncertainty principle argument that "Only electrons within $\approx kT_c$ of the Fermi-energy can play an important role in superconductivity" and these electrons have a momentum range $\Delta p \approx kT_c/v_f$. Thus

$$\Delta x \geqslant \hbar/\Delta p \approx \hbar v_f/kT_c$$

Now, the Pippard's coherence length is given by

$$\xi_o = a\frac{\hbar v_f}{kT_c} \tag{1.11}$$

where $v_f$ is the Fermi velocity and a is a numerical constant. $xi_o$ is analogous to the mean free path $l$ in the non-local electrodynamics of metals. In 1950, Ginzburg and Landau advanced a microscopic theory of superconductivity in terms of an order parameter. The Ginzburg and Landau (GL) theory concentrate completely on the superconducting electrons rather than the normal excitations. [12] The GL theory also introduces a characteristic length scale known as GL coherence length

$$\xi(T) = \frac{\hbar}{|2m^*\alpha(T)|^{1/2}} \tag{1.12}$$

where $m^* = 2m$ and $\alpha(T)$ is the expansion coefficient and vanishes as $(T - T_c)$. Far below $T_c$, GL coherence length $\xi(T) \approx \xi_o$; the Pippard's coherence length. However, these two quantities are different. The GL parameter can be defined by the ratio of the two characteristic lengths

$$\kappa = \frac{\lambda}{\xi} \tag{1.13}$$

Since, $\lambda$ and $\xi$ both diverges as $(T_c - T)^{-1/2}$ near $T_c$, this dimensionless ratio $\kappa$ is approximately independent of temperature. Typically $\kappa << 1$ implies that $\xi > \lambda$.

### 1.2.5 Type II superconductors

In 1957, Abrikosov investigated the case when $\kappa$ is larger instead of small i.e. what would happen if $\xi < \lambda$ instead of $\xi > \lambda$. [13] He found a different superconducting phase known as

type II superconductor where magnetic flux can penetrate through the superconductor in the form of a regular array of flux tubes. Each flux tubes carry the quantum of flux $\Phi_o = hc/2e$. Abrikosov showed the exact boundary of two phases at $\kappa = 1/\sqrt{2}$. He described the type I and type II superconductors as

$$\kappa = \frac{\lambda}{\xi} < \frac{1}{\sqrt{2}} \quad \rightarrow \quad \text{type I superconductors}$$
$$\kappa = \frac{\lambda}{\xi} > \frac{1}{\sqrt{2}} \quad \rightarrow \quad \text{type II superconductors}$$

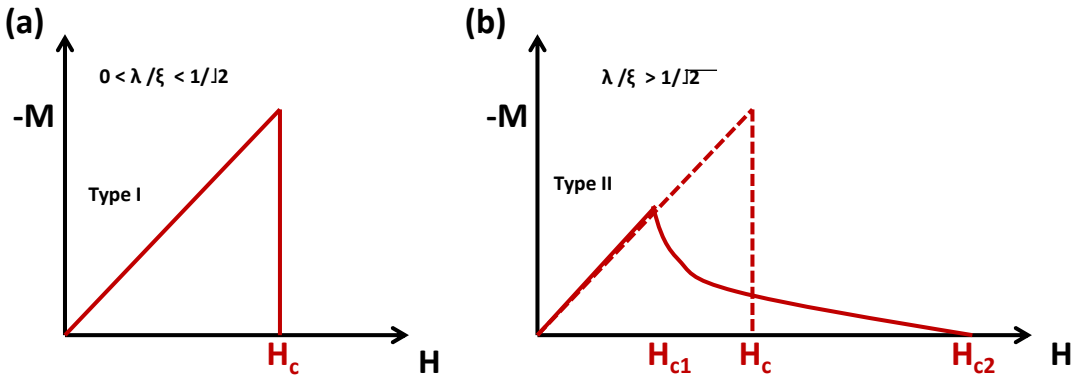


Figure 1.3: $M$ vs. $H$ plot for a (a) type I superconductor and (b) type II superconductor.

### 1.2.6 Unconventional superconductors

The superconductors which do not have a well-defined order parameter within the BCS theory are generally known as unconventional superconductors. Basically, the high-temperature superconductors are unconventional superconductors where the origin of superconducting state is not clear and still elusive with some exceptions like $MgB_2$. [14] These unconventional superconducting compounds challenge our theoretical understanding of the origin and nature of superconductivity. Experimental observations strongly indicate that there are a lot of fundamental differences between the physical properties of the conventional superconductors and high-temperature unconventional superconductors. The most significant difference is in the symmetry of their order parameters. In conventional superconductors, the order parameter is isotropic in the momentum space which means that the superconducting energy gap is symmetric (s-wave) which implies isotropic interaction between electrons in all spatial directions. However, in unconventional superconductors, the scenario is completely different and appear to be much more complex. The superconducting gap here is anisotropic. The unknown exotic phenomenon responsible for superconductivity in these materials leads to the anisotropy in the order parameter.

Apart from the high-temperature superconductors, there are many other classes of superconductors where unconventional superconductivity occurs from the number of microscopical phenomena. One of the main example is of topological superconductors. I will give a brief idea about the topological superconductivity in the next section after the introduction of topological materials (see section 1.4).

## 1.3 Topological non-trivial systems

This section briefly summarize the recent research developments in the direction of topological materials. Topologically non-trivial systems such as the topological insulators have emerged as the new quantum states of matter. [15] Their unique properties, such as the manifestation of time reversal symmetry and protected edge states have attracted the significant attention of the contemporary condensed matter physics community for fundamental studies as well as for potential applications in spintronics and fault-tolerant quantum computing. Therefore, studying their quantum novel properties under extremely special conditions is of foremost importance.

### 1.3.1 Historical perspective

In condensed matter physics, within the description of Landau's theory, phases of matter are often characterized by a very well-defined order parameter and by the symmetries they spontaneously break. For example, ferromagnets break rotational symmetry along with time reversal symmetry. The discovery of quantum Hall effect in a 2-D electron gas showed that there are phases of matter for which an order parameter cannot be defined and no spontaneous breaking of symmetry can be identified. Such phases are not understood within the frameworks of conventional theories. Unlike in classical Hall Effect, Hall conductance is quantized in quantum Hall Effect and the quantized Hall conductivity is surprisingly robust against external perturbations/disorders. [16, 17] Within the framework of the Nobel Prize-winning theory proposed by Thouless, Kohmoto, Nightingale, and den Njis (TKNN), the quantum Hall phase was understood to be a new topological phase of matter where remarkable robustness of the quantized Hall conductance is due to a topological invariant known as the Chern number. [18] More recently even more exotic states of matter were realized where topological invariants play a crucial role in determining the physical properties. One such example is the quantum spin Hall states. A special case of these states is termed as topological insulators, which are characterized by an energy gap in the bulk, like an ordinary band insulator, but conducting states on the surface. Spin-orbit coupling (SOC) causes opposite spin electrons at the edges to move in opposite directions even in the absence of an external magnetic field. These 'chiral' edge states are robust to impurities or magnetic defects as there are no states available for backscattering. Spin and momentum of the surface charge carriers are locked. These states were theoretically predicted to exist in (Hg, Cd)Te quantum well structures by Bernevig, Hughes, and Zhang and were experimentally observed in 2007. [3] Alloy $Bi_xSb_{1-x}$ was the first 3D topological insulator discovered by ARPES (Angle-Resolved Photoemission Spectroscopy) experiments. [19]

### 1.3.2 Theoretical and experimental background of topological materials

This section will provide an overview of materials which host Dirac fermions in condensed matter systems. Dirac fermions are the particles that obey the Dirac Hamiltonian instead of Schrodinger Hamiltonian. The excitations in the normal metals and doped semiconductors can be described well by the Schrodinger equation

$$i\hbar\frac{\partial}{\partial t}|\psi(t)>=H_s|\psi(t)> \tag{1.14}$$

The Schrodinger Hamiltonian is given as $H_s = p^2/2m^*$, where $\hbar$ is the reduced Planck's constant, $m^*$ is the effective mass and $p$ is the momentum. Schrodinger fermions are accompanied by a parabolic dispersion relation $E \propto p^2$. However, recent discoveries showed that there are some materials that host relativistic excitations, the most famous one is called Dirac fermions. These relativistic excitations cannot be described by conventional Schrodinger Hamiltonian but can be described by Dirac Hamiltonian [20]

$$H = c\sigma.p + mc^2\sigma_z \tag{1.15}$$

$\sigma = (\sigma_x, \sigma_y)$ & $\sigma_z$ are the Pauli matrices and c is the speed of light, c is replaced by $v_F$, the Fermi velocity in condensed matter systems. Dirac fermions show a linear energy dispersion. If the mass vanishes in equation 1.15 then there will be no possibility of opening a gap at Dirac point because this is the only perturbation term in the Dirac Hamiltonian. [21, 22] This will be useful in case of Weyl semimetals (WSM) which I will discuss in the next section. The Dirac Hamiltonian leads to an interconnection of conduction band and valence band even in case of non zero Dirac mass.

More generally the Dirac equation [21] can be written as

$$i\hbar\frac{\partial}{\partial t}|\psi(t)>=(c\alpha.p+\beta mc^2)|\psi(t)> \tag{1.16}$$

In the relativistic regime, when $cp >> mc^2$, the chirality $\sigma.p/p$ defines whether the spin and momentum of a (quasi) particle are aligned parallel or antiparallel. Thus the chirality can have the values +1 or -1 for parallel or antiparallel alignment. For massless particles the chirality is similar to the helicity. [23] One more important dynamics of the particles arises due to the chirality of the particles. If the momentum of the particles changed from $p$ to -$p$ it also needs to flip the spin $\sigma$ to $-\sigma$. This process of backscattering is suppressed without spin-flip.

The most famous Dirac material is graphene; a monolayer of graphite. [24] The band structure of a monolayer of carbon host Dirac like touching point (Dirac cone) and show linear dispersion above and below these points. In particular, the important 2D Dirac system is the 3D topological insulator. [25] In topological insulators, the bulk is insulating like an ordinary band insulator while the surface is conducting. [26] Commonly, these conducting states arise from the linear band crossing leads to the Dirac like dispersion. The origin of these surface states is of topological character. [27] The insulating bulk of TI hosts inverted bands; the valence band goes above the conduction band and conduction band drops below the valence band this is how they reverse the role. Spin-orbit coupling causes an insulating material to acquire protected surface states in topological insulators. The first generation of topological insulator found in $Bi_{1-x}Sb_x$. More famous and extensively investigated generation of the topological insulator is $Bi$ compounds such as $Bi_2Se_3$ and $Bi_2Te_3$. [26]

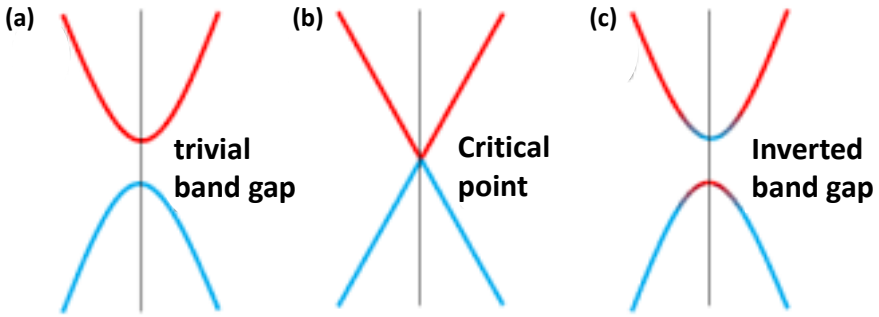


Figure 1.4: (a) Showing the band gap in a normal band insulator (b) Critical point where valence band and conduction band touches at a single point (c) Inverted bands: a case of topological insulator. [28]

In figure 1.4, we show how trivial band insulator can become the topological insulator (TI) by tuning the external parameter. The external parameter here is the Spin-Orbit Coupling. Spin-Orbit Coupling plays an important role in topological materials. The inverted bands are responsible for the conducting surface states in TIs. At the critical point, valence band and conduction band touch at a single point called the Dirac-point. This phase is known as Dirac semi-metal (DSM).

### 1.3.3 Dirac and Weyl semimetals

Before discussing the Dirac semimetals (DSM), let us first discuss Weyl semimetals (WSM). Since Dirac semimetals are the special case of Weyl semimetals from the point of view of symmetry. In 1929, Weyl simplified the Dirac Hamiltonian and proposed Weyl Hamiltonian by considering the zero mass of the particles. [22]

$$H_W = \pm c(\sigma_x p_x + \sigma_y p_y + \sigma_z p_z) \tag{1.17}$$

Equation 1.17 shows the topologically protected chiral charge. [29] It can also be seen as a pseudo-magnetic monopole in the momentum space. [30, 31] Mathematical description of the monopole needs the introduction of Berry curvature which can be understood as the induced flux by the monopole. Integration over a small surface including one Weyl node adds $\pm 2\pi$ to the flux. [32] The sign indicates the chirality of the Weyl node. Integration over the whole Brillouin zone should give zero because Weyl nodes appear in pairs with opposite chirality. Since, Dirac point is protected by time reversal and inversion symmetry, in case of Weyl semi-metals either time reversal or inversion symmetry needs to be broken. Time reversal symmetry requires a particle to move in the opposite momentum direction with the opposite spin i.e. $E(k,\uparrow) = E(-k,\downarrow)$ [33] and inversion symmetry imposes a condition that a particle should move in opposite momentum direction with same spin i.e. $E(k,\uparrow) = E(-k,\uparrow)$. According to the broken symmetry, the degeneracy of the Dirac point will be lifted and will leave two Weyl points behind with double degeneracy. When One chiral Weyl node connects with the other with opposite chirality it gives rise to the more exotic states called Fermi arc. [29] Chiral anomaly is also an exotic phenomenon which appears only in case of Weyl semimetals when Weyl points are separated in momentum space. [31] The experimental observation of chiral anomaly needs application of magnetic field which itself breaks the time reversal symmetry, therefore, this effect can also be seen in Dirac semimetals. In the presence of magnetic field Dirac point splits into two Weyl points leads to the chiral anomaly in the experimental measurements. The famous Weyl semimetals are TaAs, TaP, NbAs and NbP. All of these belongs to the same family. [34–37]

DSMs can be understood in two ways; 1) 3D Dirac semimetals can be similar to the 2D graphene with the linear dispersion in all three momentum directions. 2) Dirac semimetals can be the special case of Weyl semimetals. In DSM, two Weyl nodes with opposite chirality overlap without annihilating each other, since it is known that two Weyl nodes of opposite chirality will annihilate each other if they come closer. However, interestingly, in case of Dirac semimetals, some symmetries block this annihilation and protect them. [20] In addition to the time reversal and inversion symmetry crystalline rotational symmetry also protect the Dirac point in DSMs and make this phase to occur with stability. Therefore, two Weyl nodes with

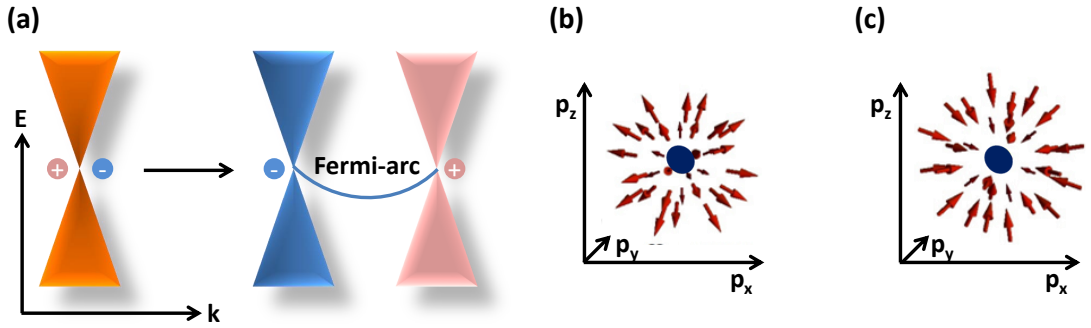


Figure 1.5: (a) Single Dirac cone which splits in to two Weyl nodes with opposite chirality by breaking either inversion or time-reversal symmetry. (b, c) Represent two Weyl nodes with opposite chirality. (Image credit: (b) and (c) are from Wikipedia.

opposite chirality can exist at the same momentum and lead to the Dirac node and symmetries play a crucial role in the existence of DSMs. Thus, the Dirac point holds four-fold degeneracy. [20]

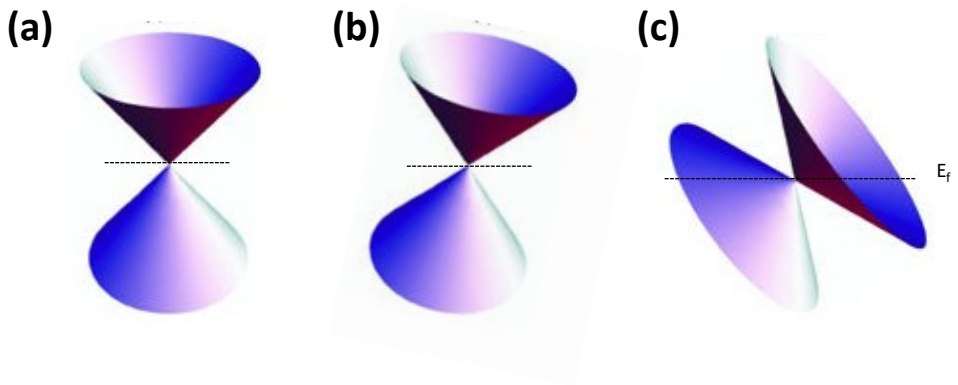


Figure 1.6: (a) A Dirac cone symmetric about the touching point, known as type I Dirac cone. (b) A tilted Dirac-cone but still touching point is a single point. (c) A tilted Dirac-cone up to the limit where conduction and valence band are crossing the Fermi-level. Image is taken from ref [38] and edited.

All the cases discussed above were of an ideal type of Dirac/Weyl cones where cones are symmetric above and below the touching points. However, in real crystals, the scenario is different not that much ideal. In real materials, the effect of finite temperature and scattering comes into the picture. Mass-induced energy gaps also play an effective role in determining the band structure. These factors can give rise to the asymmetries resulting in tilted Dirac/Weyl cone. [39] In figure 1.6, two types of tilted Dirac cones are shown, the first one is not so special because still conduction band is above the Dirac point and valence band is below the Dirac point. The Fermi level is crossing only at a point as it was in the ideal case. Therefore, the basic properties remain similar as of untilted case. In the second figure 1.6 (c), Dirac/Weyl cone is tilted at higher degree leads to a situation where the Fermi energy crosses the bulk conduction and valence bands, consequently, the density of states at the Fermi level is non-zero

even if the Fermi level is situated at the touching point (DP/WP). [40] This is the scenario in type II semimetals which consequently exhibits an open Fermi surface leading to the more exotic electronic properties. [41]

### 1.3.4 Concept of topological equivalence

First, we will understand the concept of topology in quantum mechanical wavefunctions. Topology is a mathematical concept to classify shapes or geometries. If any object can be continuously transformed into other by bending or stretching then all the geometries one can make out of the given geometry will be topologically equivalent. For example, a doughnut and a coffee cup belong to the same topological class as both the shapes can be characterized by the single hole in the shapes. Similarly by squeezing the sphere it can be transformed into the bowl without creating or closing any hole, therefore, the sphere and a bowl belong to the same topological class. It can be better understood by the mathematical interpretation of Gauss-Bonnet theorem where Gaussian curvature of the surface of an object can be evaluated by counting the number of holes in a given object.

$$\int_O k dA = 4\pi(1-g)$$

Here, k is the Gaussian curvature of the object O. This statement tells that the integration of Gaussian curvature all over the surface is equal to $4\pi(1-g)$, here g represents the number of holes in the given object. Small deformations on the surface can modify the curvature locally but the integral all over the surface will still be equal to $4\pi(1-g)$. Therefore, g is a topological invariant which is not going to change by the small deformations on the given surface.


Figure 1.7: Topological equivalence of geometrical objects where a sphere and a bowl are equivalent and a doughnut and a coffee mug are equivalent topologically. (Image credit: Wikipedia)

In condensed matter physics, it has recently been discovered that certain quantum phases of matter display unique physical properties that can be understood only by the quantities analogous to the topological invariant $g$. Quantum phases with an energy gap (e.g. Band insulator, semiconductor) are topologically equivalent if they can be smoothly deformed into one another

without closing the gap. Two quantum mechanical wavefunctions can be in the same topological class if they are connected adiabatically into each other. A normal band insulator is characterized by the finite gap at the Fermi-level. The transition from normal band insulator into the topological insulator needs to close the gap somewhere in between at the critical point where valence band touches the conduction band at a single point. Therefore, these phases are in different topological class. Such phases can be described well within the framework of topological band theory. Thouless, Kohmoto, Nightingale, and den Njis (TKNN) defined the topological phases by introducing topological invariants. [18]

Topological invariants of phases of matter can be calculated by the Berry phase. Therefore, before introducing the topological invariants we give a brief review of Berry phase.

### 1.3.5 Berry phase

In classical and Quantum mechanics, the Berry phase arises in a cyclic adiabatic process. When a system is subjected to cyclic adiabatic processes, it acquires some geometrical properties of the parameter space of the Hamiltonian that relates directly to the Berry phase. These concepts were first introduced by S. Pancharatanam [42] in 1956 and by H. C. Longuet Higgins [43] in 1958 and completely generalized by Michael [44] Berry in 1984. This phase is also known as Pancharatanam phase or Berry phase. The Berry phase can be observed experimentally in the Aharonov-Bohm effect. Where, the wave function of a charged particle passing around a long solenoid experiences a phase shift as a result of the enclosed magnetic field, this phase shift is analogous to the Berry phase. [45] The adiabatic parameter in the case of the Aharonov-Bohm effect is the magnetic field enclosed by two interference paths.

Let us take a general Hamiltonian $H(R)$ that depends on a certain set of parameters say $R = (R_1, R_2, R_3, .....)$ and $|n(R)>$ is the initial eigenstate. The eigenstates are defined in the corresponding parameter space. The wavefunctions may have a non-trivial topological character. The Berry phase characterizes such a non-trivial topology in the parameter space. The eigenstates are given by the solution of time-independent Schrodinger equation

$$H(R)|n(R)>= E_n(R)|n(R)> \tag{1.18}$$

Now, we are interested in the adiabatic time evolution of the state $|n(R)>$ along some closed path C. The system is initially prepared in the state $|n(R(t=0))>$. In Quantum mechanics, the adiabatic theorem can be applied to a system whose Hamiltonian slowly varies with time. According to the Adiabatic theorem, the system will always remain in its instantaneous eigenstate at any time t. It implies that the time evolved state $|n(R(t))>$ will be the instantaneous eigenstate of $H(R(t))$ for slowly varying $R$. The time evolved state at time $t$ can be written as $|\psi(t)>= e^{-i\theta(t)}|n(R(t))>$ and the time-dependent Schrodinger equation can be written as

$$H(R(t))|\psi(t)>= i\hbar\frac{d}{dt}|\psi(t)> \tag{1.19}$$

after putting the $|\psi(t)>$ it becomes

$$E_n(R(t))|n(R(t))>= \hbar(\frac{d}{dt}\theta(t))|n(R(t))> +i\hbar\frac{d}{dt}|n(R(t))> \tag{1.20}$$

scalar product with <n(R(t))| gives

$$E_n(R(t)) - i\hbar < n(R(t))|\frac{d}{dt}|n(R(t))>= \hbar(\frac{d}{dt}\theta(t)) \tag{1.21}$$

from here $\theta(t)$ can be written as

$$\theta(t) = \frac{1}{\hbar}\int_0^t E_n(R(t'))dt' - i\int_0^t < n(R(t'))|\frac{d}{dt'}|n(R(t'))> dt' \tag{1.22}$$

In equation 1.17 the first term is the dynamical phase and the second term is corresponding to the geometrical phase which is also known as the Berry phase that arises due to the time evolution of the Hamiltonian. It indicates that the time evolved state has picked some phase that depends on the trajectory in the parameter space.

Berry phase

$$\gamma_n = i\int_0^t < n(R(t'))|\frac{d}{dt'}|n(R(t'))> dt \tag{1.23}$$

and Berry potential can be described as

$$A_n(R) = i < n(R(t'))|\frac{d}{dt'}|n(R(t'))> \tag{1.24}$$

In the next section we will use equation 1.24 (Berry potential) to calculate the topological invariants.

### 1.3.6 Topological invariants

In condensed matter, if we take a Hamiltonian which can be described by the Bloch state $u(k)$, k is the crystal momentum then Berry potential can be described as

$$A_n(k) = i < u(k)|\nabla_k|u(k) > \tag{1.25}$$

The curl of Berry potential will give the Berry flux equivalent to the magnetic field obtained from Maxwell's equation ($\vec{B} = \vec{\nabla} \times \vec{A}$)

$$F(k) = \nabla_k \times A_n(k) \tag{1.26}$$

Now, Chern number n will be

$$n = \frac{1}{2\pi} \oint_{BZ} F(k).dS(k) \tag{1.27}$$

That is how the Chern number (n) identify the topologically trivial and non-trivial phase. If the value of n is zero it will correspond to a topological trivial phase while the non-zero value will be corresponding to the non-trivial phase of matter.

## 1.4 Topological superconductors

Topological classifications are not limited to the insulators and semimetals but also conducted for the superconductors based on the symmetry properties. In 2000, topologically nontrivial superconductors were discussed in a 2D model by Green and in a 1D model by Kitaev. [48, 49] For the superconducting state, both the models consider spinless, time-reversal-breaking and p-wave pairing which leads to the existence of exciting particles known as Majorana particles in the vortex core in case of 2D and at the edges in case of 1D. Majorana particle is its own antiparticle. Ettore Majorana modified Dirac equation in 1937 using real numbers and described Majorana particle that was its own antiparticle. [7, 15, 46, 47] Initially, the neutrino has been considered as Majorana particle but after the discovery of a non-vanishing mass of the neutrino, there is no fundamental particle to be considered as Majorana particle. However, such particles are predicted to exist in some of the condensed matter systems like in topological superconductors. Sato proposed a model in 2D to realize Majorana zero modes even in case of

s-wave superconducting pairing in 2003. [50] The ideas of realizing topological superconductors emerged only after the successful discovery of the topological insulators, which provides an appropriate platform for spinless superconductivity.

Experimental realization of such a superconducting phase in topological insulators demands intercalation of elemental metals in these materials or application of extremely high pressure. [51–54] There have been a lot of efforts to induce superconductivity in topological insulators. The heterostructures of superconductors and the interfaces of topological insulators and superconductors have been rigorously studied and there are some shreds of evidence exist of the presence Majorana states in such structures. [5, 6]

The primary goal of this thesis is to use scanning tunneling microscopy and spectroscopy (STM/STS) to study the superconducting phases in topologically non-trivial materials. Our results, together with the other emerging discoveries in the respective field, may help to untangle the fundamental physics.

# Bibliography


[1] J. Bardeen, L. N. Cooper, J. R. Schrieffer, Phys. Rev. **106**, 162 (1957).

[2] M. Tinkham, Introduction to Superconductivity (McGraw-Hill, Singapore, 1996).

[3] M. Konig, S. Wiedmann, C. Brüne, A. Roth, H. Buhmann, L. W. Molenkamp, X. -L. Qi, S. -C. Zhang, Science **318**, 766 (2007).

[4] X. -L. Qi and S. -C. Zhang, Rev. Mod. Phys. 83, 1057 (2011).

[5] M. X. Wang et. al., Science **336**, 52 (2012).

[6] V. Mourik, K. Zuo, S. M. Frolov, S. R. Plissard, E. P. A. M. Bakkers, L. P. Kouwenhoven, Science **336**, 1003 (2012).

[7] M. Sato and Y. Ando, Rep. Prog. Phys. **80**, 076501 (2017).

[8] H. Kamerlingh Onnes, Leiden Comm. 120b, 122b, 124c (1911).

[9] W. Meissner, R. Ochsenfeld, Naturwissenschaften **21**, 787 (1933).

[10] C. A. Reynolds, B. Serin, and L. B. Nesbitt, Phys. Rev. **84**, 691 (1951).

[11] P. Phillips, Advanced Solid State Physics, second edition, Cambridge University Press, Pp. 402. (2012).

[12] G. E Blonder, M. Tinkham,and T.M. Klapwijk, Phy. Rev. B (1982).

[13] A. A. Abrikosov, Journal of Physics and Chemistry of Solids, **2** 199–208 (1957).

[14] J. A. Silva-Guillen, Y. Noat, T. Cren, W. Sacks, E. Canadell, and P. Ordejon, Phys. Rev. B **92**, 064514 (2015).

[15] C. L. Kane, and E. J. Mele, Phys. Rev. Lett. **95**, 146802 (2005).

[16] C.L. Kane and E.J. Mele Phys. Rev. Lett. **95**, 226801 (2005).

[17] B. A. Bernevig, T. Hughes and S.C. Zhang, Science **314**, 1757 (2006).

[18] D. J. Thouless, M. Kohmoto, M. P. Nightingale, and M. den Nijs Phys. Rev. Lett. **49**, 405 (1982).

[19] D. Hsieh, D. Qian, L. Wray, Y. Xia, Y. Hor, R.J. Cava and M.Z. Hasan, Nature **452**, 970 (2008).

[20] P. A. M. Dirac, Proc. of the Royal Soc. of London A, **117**, 610–624 (1928).

[21] T. O. Wehling, A. M. Black-Schaer, and A. V. Balatsky, Advances in Physics **63**, 1–76 (2014).

[22] H. Weyl, Zeitschrift fur Physik **56**, 330–352 (1929).

[23] C. G. Bohmer and L. Corpe, Jour. of Phys. A **45**, 205206 (2012).

[24] A. H. C. Neto, F. Guinea, N. M. R. Peres, K. S. Novoselov, and A. K. Geim, Rev. of Mod. Phys. **81**, 109 (2009).

[25] M. B. Schilling, A. Lohle, D. Neubauer, C. Shekhar, C. Felser, M. Dressel, and A. V. Pronin, Phys. Rev. B **95**, 155201 (2017).

[26] M. Z. Hasan and C. L. Kane, Rev. of Mod. Phys. **82**, 3045–3067 (2010).

[27] M. Z. Hasan and J. E. Moore, Ann. Rev. of Cond. Matt. Phys. **2**, 55–78 (2011).

[28] A. Bansil, H. Lin, and T. Das, Colloquium: Topological Band Theory, arxiv:1603.1603.03576.

[29] S. Jia, S. Y. Xu, and M. Z. Hasan, Nature Materials **15**, 1140–1144 (2016).

[30] X. Wan, A. M. Turner, A. Vishwanath, and S. Y. Savrasov, Phys. Rev. B **83**, 205101 (2011).

[31] M. Z. Hasan, S.-Y. Xu, I. Belopolski, and S.-M. Huang, Ann. Rev. of Cond. Matt. Phys. **8**, 289–309 (2017).

[32] A. M. Turner and A. Vishwanath, Contemporary Concepts of Cond. Matt. Sci. **6**, 293-324 (2013).

[33] J. S. Lamb and J. A. Roberts, Physica D: Nonlinear Phenomena **112**, 1–39 (1998).

[34] S. Y. Xu, et. al., Science **349**, 613–617 (2015).

[35] X. Huang, et. al., Phys. Rev. X **5**, 031023 (2015).

[36] N. Xu., et. al., Nature Communications **7**, 11006 (2016).

[37] C. L. Zhang, et. al., Nature Communications **7**, 10735 (2016).

[38] M. Yan et. al., Nature Comm. **8**, 257 (2017).

[39] M. N. Ali, J. Xiong, S. Flynn, J. Tao, Q. D. Gibson, L. M. Schoop, T. Liang, N. Haldolaarachchige, M. Hirschberger, N. P. Ong, and R. J. Cava, Nature **514**, 205–208 (2014).

[40] A. A. Soluyanov, D. Gresch, Z. Wang, Q. Wu, M. Troyer, X. Dai, and B. A. Bernevig, Nature **527**, 495–498 (2015).

[41] S. -Y. Xu, et. al., Science **347**, 294–299 (2015).

[42] S. Pacharatanam, Proc. Indian Acd. Sci. A. **44**, 247-262 (1956).

[43] H. C. L. Higgins, Proc. R. Soc. A. **244**, 1-16 (1958).

[44] M. V. Berry, Proc. Royal Soc. A. **392**, 45-57 (1984).

[45] Y. Aharonov and D. Bohm, Phys. Rev. **115**, 485 (1959).

[46] C. W. J. Beenakker, Annu. Rev. Condens. Matter Phys. **4**, 113–136 (2013).

[47] M. Sato, and S. Fujimoto, J. Phys. Soc. Jpn. **85**, 072001 (2016).

[48] N. Read and D. Green, Phys. Rev. B **61**, 10267–10297 (2000).

[49] A. Y. Kitaev, Physics-Uspekhi **44**, 131 (2001).

[50] M. Sato, Phys. Lett. B **575**, 126–130 (2003).

[51] Y. S. Hor, A. J. Williams, J. G. Checkelsky, P. Roushan, J. Seo, Q. Xu, H. W. Zandbergen, A. Yazdani, N. P. Ong, and R. J. Cava, Phys. Rev. Lett. **104**, 057001 (2010).

[52] M. Kriener, K. Segawa, Z. Ren, S. Sasaki, and Y. Ando, Phys. Rev. Lett. **106**, 127004 (2011).

[53] Shruti, V. K. Maurya, P. Neha, P. Srivastava, and S. Patnaik, Phys. Rev. B **92**, 020506(R) (2015).

[54] C. Q. Han, et. al., App. Phys. Lett. **107**, 171602 (2015).

Chapter 2

# Experimental Techniques

This chapters introduces the experimental techniques that has been used in this thesis namely the Scanning Tunneling Microscope (STM) and Point-Contact Andreev Reflection Spectroscopy (PCAR). STM is a most powerful technique to study the physics of low energy excitations in the condensed matter systems. Firstly, I will briefly go through the detailed description and basic concepts of Scanning Tunneling Microscope (STM) and then briefly explain the Point-Contact Andreev Reflection Spectroscopy (PCAR).

## 2.1 Scanning Tunneling Microscope (STM)

The Scanning Tunneling Microscope was invented for the first time by G. Binning and H. Rohrer in 1981. [1] Few years later, they were awarded by the Nobel prize in Physics. This invention changed the standard of research completely in experimental condensed matter physics. STM provides the ability to see the topographic features of materials at angstrom level and the ability to resolve the electronic information at $\mu eV$ level. Basically, the STM works on the basic principle of quantum tunneling. In the next section the brief introduction to the working principle and the components of STM will be explained. The discussion of tunneling theory is also included.

### 2.1.1 Working principle

The STM works on the quantum tunneling process correlated with the wave nature of electrons in quantum mechanics. A schematic presented in figure 2.1 shows a sample and a conducting tip connected through the current amplifier. The conducting tips usually made of metallic wires (see section 2.2.3) is positioned close to the sample using the feedback loop. The distance between the two (tip and the sample) is maintained so that the tunneling current can be measured from the tip after applying the appropriate voltage bias to the sample or one can do the reverse process. The vacuum or oxide act as a potential barrier between these two. The tunneling gap typically is of the order of several angstroms between tip and sample. This process enables us

to scan over the surface of the sample as shown in figure 2.1. Imaging of the surface can be done in two ways 1) in constant current mode 2) in constant height mode.

To get high resolution image (atomic scale) of sample surface we need to have a clean surface, clean environment around. Therefore, to keep sample surface clean vacuum is the best option. At higher temperatures thermal vibrations (e.g., lattice vibrations) appear in the sample. Therefore, to avoid these lattice vibrations for the accuracy of measurement low temperature is required. The value of tunneling current is the order of pico amperes. To measure it accurately we have to decrease the mechanical vibrations of the system as much as possible.

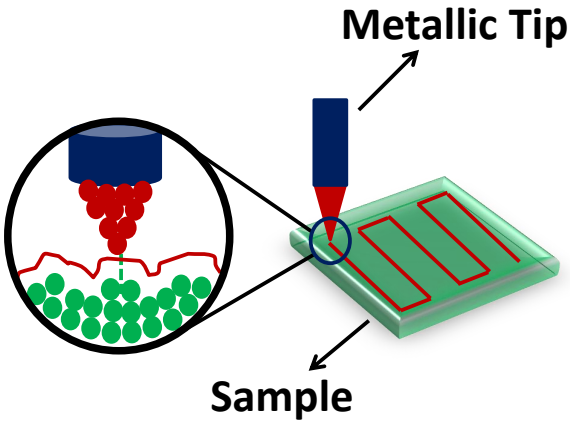


Figure 2.1: The schematic of Sccaning Tunneling Spectroscopy.

### 2.1.2 Theoretical description of quantum tunneling current

In classical mechanics, particles can pass through a barrier only when the energy of the particles exceeds the barrier height (E > V). However, in Quantum mechanics due to the wave-like nature of particles, there is always some probabilities for crossing the barrier even for E < V and this process is known as quantum tunneling. The tunneling current between two metals first measured by Giaever [2, 3] and then most interesting results were obtained by Nicol, Shapiro, and Smith [4, 5] in metal/superconductor and superconductor/superconductor junctions. They find direct evidence for a gap in the quasi-particle spectrum of the superconductor. The tunneling current depends upon the barrier width and decays exponentially by the relation, $I \propto e^{-2kd}$, where $d$ is the barrier width.

In 1961, J. Bardeen proposed a general formalism to describe electron tunneling between two electrodes and for complex geometries which also accounts for the existence of multiple conduction channels. Within the Bardeen's model, the equation of tunneling current is derived by the approach of Fermi's golden rule using time-dependent perturbation theory. The tunneling current between a normal metal and a superconductor junction can be given as

$$I = -\frac{4\pi e}{\hbar}\int_{-ev}^{0} |M|^2 N_n(\varepsilon) N_s(\varepsilon + eV)[f(\varepsilon) - f(\varepsilon + eV)]d\varepsilon \tag{2.1}$$

Where, $\hbar$ is the reduced Planck's constant, M is the tunneling matrix, $N_n(\varepsilon)$ are the density of states of a normal metal, $N_s(\varepsilon + eV)$ are the density of states of a superconductor and $f(\varepsilon)$ is the Fermi-function

$$f(\varepsilon) = \frac{1}{1+e^{\varepsilon/k_B T}}$$

If one electrode is a metal and another is a superconductor then density of states of a metal can be taken as flat (constant) near the Fermi-energy (within the order of magnitude of meV). Tunneling matrix M can be approximated as the exponential function $\propto e^{-2kd}$ as M is the expectation value of the single particle transition probability across the barrier. At sufficiently low temperatures, the Fermi-function shows a sharp cut off at Fermi-energy. [6] Thus, the tunneling current is proportional to the integral of the density of states of the superconducting electrode.

$$I = \frac{-4\pi e}{\hbar} e^{-2kd} N_n(\varepsilon) \int_{-ev}^{0} N_s(\varepsilon + eV)d\varepsilon \tag{2.2}$$

The equation 2.2 reflects an approximation at approximately zero temperatures and for small potential difference.

### 2.1.3 Scanning Tunneling Spectroscopy (STS)

#### Topographic mode

In STM feedback loop enables imaging of surface in two different modes which can reveal the topographic features.

**1) Constant current mode:** In this mode, current is kept at particular value and the height of the tip changes according to the height/DOS profile of the surface. The variation in height is measured as a function of position which reflects the topographic/electronic features.

**2) Constant height mode:** In this mode, tip height from the surface is kept at constant value and the current varies according to the height/DOS profile. The variation in current as a function of position reveals the topographic/electronic features.

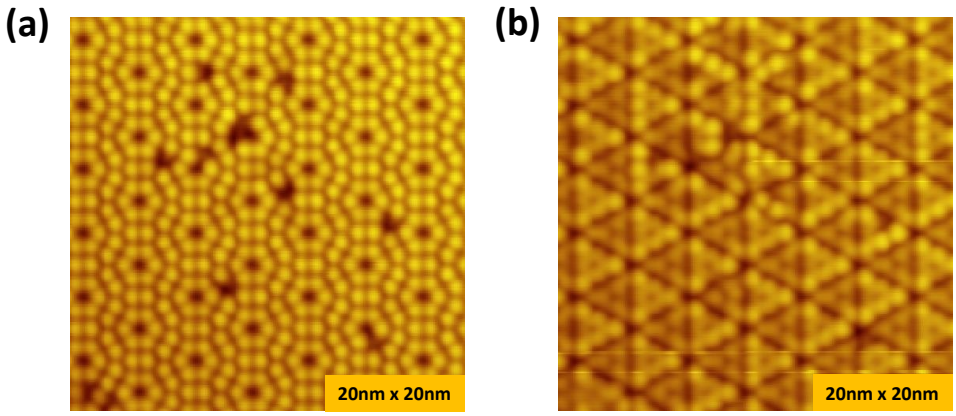


Figure 2.2: Topographic image of silicon $7 \times 7$ reconstruction by applying (a) positive bias and (b) negative bias voltage to the sample.

Constant current mode is used to image the topography of the samples and constant height mode is used to map the conductance in the measurements. In figure 2.2 we have shown the topographic image of $7 \times 7$ reconstruction of silicon surface. Both the images (a & b) have been measured on same area in constant current mode. However, the difference in both the images is the polarity of the applied bias voltage, in (a) sample has been kept at positive bias while in case of (b) the sample has been kept at negative bias. The density of states at the Fermi level will be different as the applied voltage is different. Therefore, it is clear from here that the STM measures the local electronic structure of the conducting samples.

**Tunneling Spectroscopy:**

There are several methods to study the superconducting phases and to measure the superconducting energy gap like Penetration depth measurement, Specific heat measurement, Point-Contact Spectroscopy (PCS) and Scanning Tunneling Spectroscopy (STS) etc. STS and PCS are the direct and more accurate methods to measure the superconducting energy gap. It can be obtained by measuring the tunneling conductance.

The tunneling conductance can be obtained by differentiating the tunneling current with respect to applied voltage

$$\frac{dI}{dV} = \frac{-4\pi e}{\hbar} e^{-2kd} N_n(\varepsilon) \frac{d}{dV} \left( \int_{-ev}^{0} N_s(\varepsilon + eV) d\varepsilon \right) \tag{2.3}$$

The superconducting density of states can be described as

$$N_s(E) = \left(\frac{E}{\sqrt{E^2-\Delta^2}}\right)$$

$\Delta$ is the superconducting energy gap of the superconducting electrode. By fitting the experimental data using tunneling equation (equation 2.3) superconducting gap can be evaluated.To take care of the broadening of the BCS [7] density of states of a superconductor possibly due to finite life time of quasiparticles Dyne included an effective broadening parameter to the density of states [8]

$$N_s(E) = Re\left(\frac{(E-i\Gamma)}{\sqrt{(E-i\Gamma)^2-\Delta^2}}\right)$$

We have used Dyne's equation [8] of tunneling conductance to fit the experimental data in our analysis.

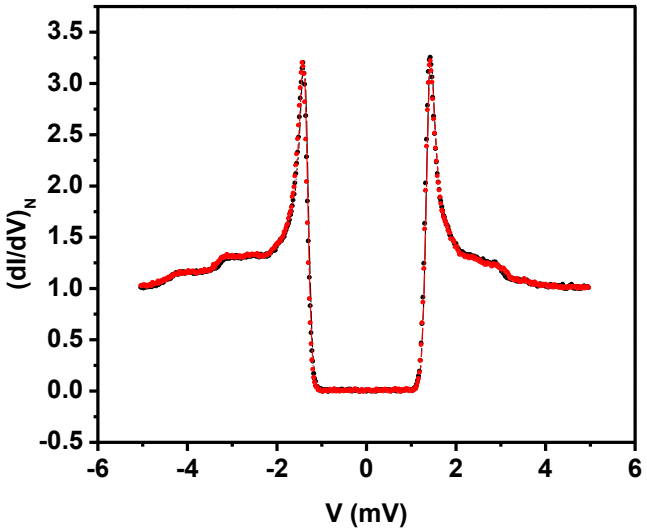


Figure 2.3: Tunneling spectrum measured on superconducting Pb using PtIr tip.

In figure 2.3, we have shown a representative spectrum obtained on superconducting Lead (Pb) sample using PtIr tip at 300 mK temperatures. A fully formed superconducting gap can be seen clearly which confirms the ability of the instrument used in this work. The typical value of parameters are $I = 1nA$ and $V = 500mV$.

## 2.2 Overview of Scanning Tunneling Microscope

### 2.2.1 STM system and its components

Our STM system works down to 300 mK and is integrated with an 11 Tesla superconducting magnet. The system is integrated with a number of UHV growth, characterization and preparation tools e.g., RHEED, LEED, K-Shell evaporators and an in-situ cleaver. All the specifications I will discuss in detail below. I have also used a home-built point contact spectroscopy probe to investigate the superconducting phases of a number of systems. The lowest temperature achieved in this case is 1.4 K and this system is equipped with a vector magnet (6 T in Z-direction, 1-1 T in X and Y directions).

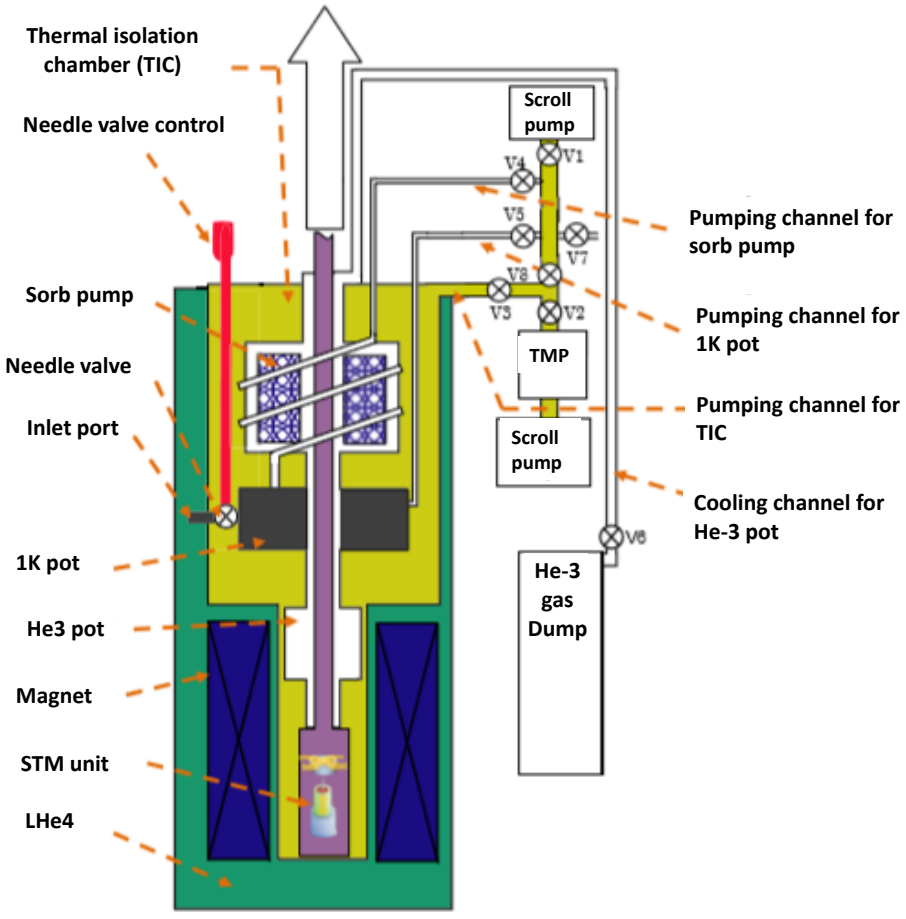


Figure 2.4: The overview of Observation chamber components

An overview of STM system used in this study is shown in figure 2.4. This figure is adopted from the manual of our STM. All the main components are shown by the dashed lines and explained within the figure.

### 2.2.2 STM head/unit

In this instrument, the scanning process is performed by the single tube-type piezo driver which can be driven by 6 electrodes (as shown in Fig.2.5), that is, 5 outer electrodes; +X, -X, +Y, -Y, Feedback Z (scan Z), and one inner electrode: offset Z. The Z Scan range is extended by the negative voltage, on the other hand, the offset Z is extended with the positive voltage. This figure is adopted from the manual of our STM.

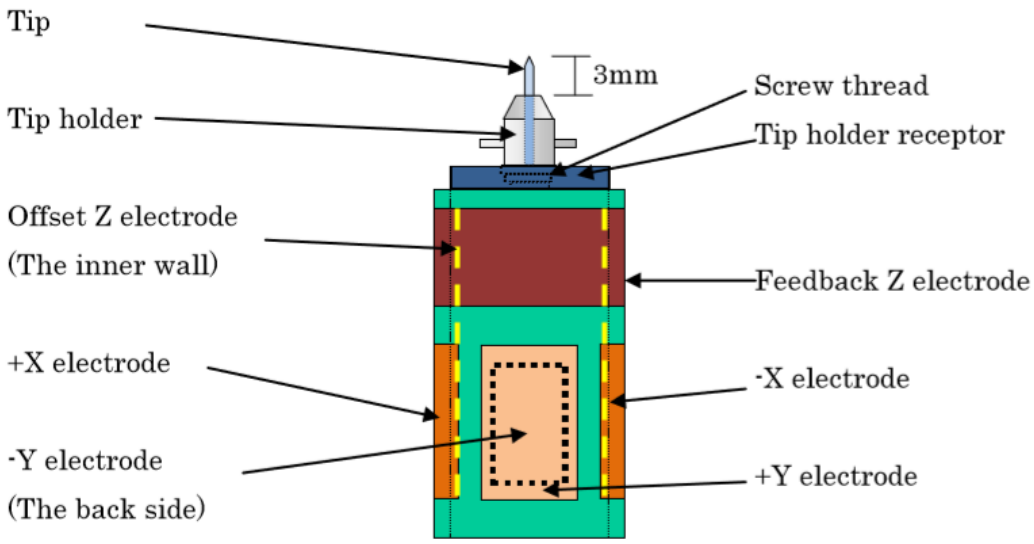


Figure 2.5: The features of scanning tube-type piezo driver.

The tube-type piezo is located in an approach stage which is supported by an inertial piezo slider (I.P.S.) devices within the approach stage holder. I.P.S device is driven by the combination of friction and inertial movement controlling motion. Each step which driven by I.P.S. device is approximately 1 $\mu$m at RT with 120 V. The working distance of the approaching stage is approximately 5mm in Z direction. The working distance (X and Y direction) of the sample stage are (0.5 mm). The maximum scan area by the scanning tube-type piezo is approximately 2.3 $\mu$m in length at RT.

### 2.2.3 Electrochemical etching of metallic tip

STM is used for surface analysis. We are able to obtain the physical properties of samples like electronic state and atomic structure from the tunneling current arise by having very sharp tip close to the sample surface. Sharpness of the STM tip is very important for good image since the tip has to detect the tunneling current from one individual atom which constructs the surface of the sample, therefore, resolution of the STM image is greatly affected by the sharpness of the

tip. We made very sharp STM tips by electrochemical etching. A tungsten wire and Platinum ring submerged into Potassium Hydroxide solution (KOH) and a voltage is applied between the tungsten wire and Platinum ring. The submerged section near by meniscus is most ablated since the tungsten wire is very close to meniscus. The constriction point made by this erosive process gradually becomes thin. Finally, the area under the constriction point fall off and the edge of tungsten wire become very sharp. one of the tip apex made by this method is shown in figure 2.7.

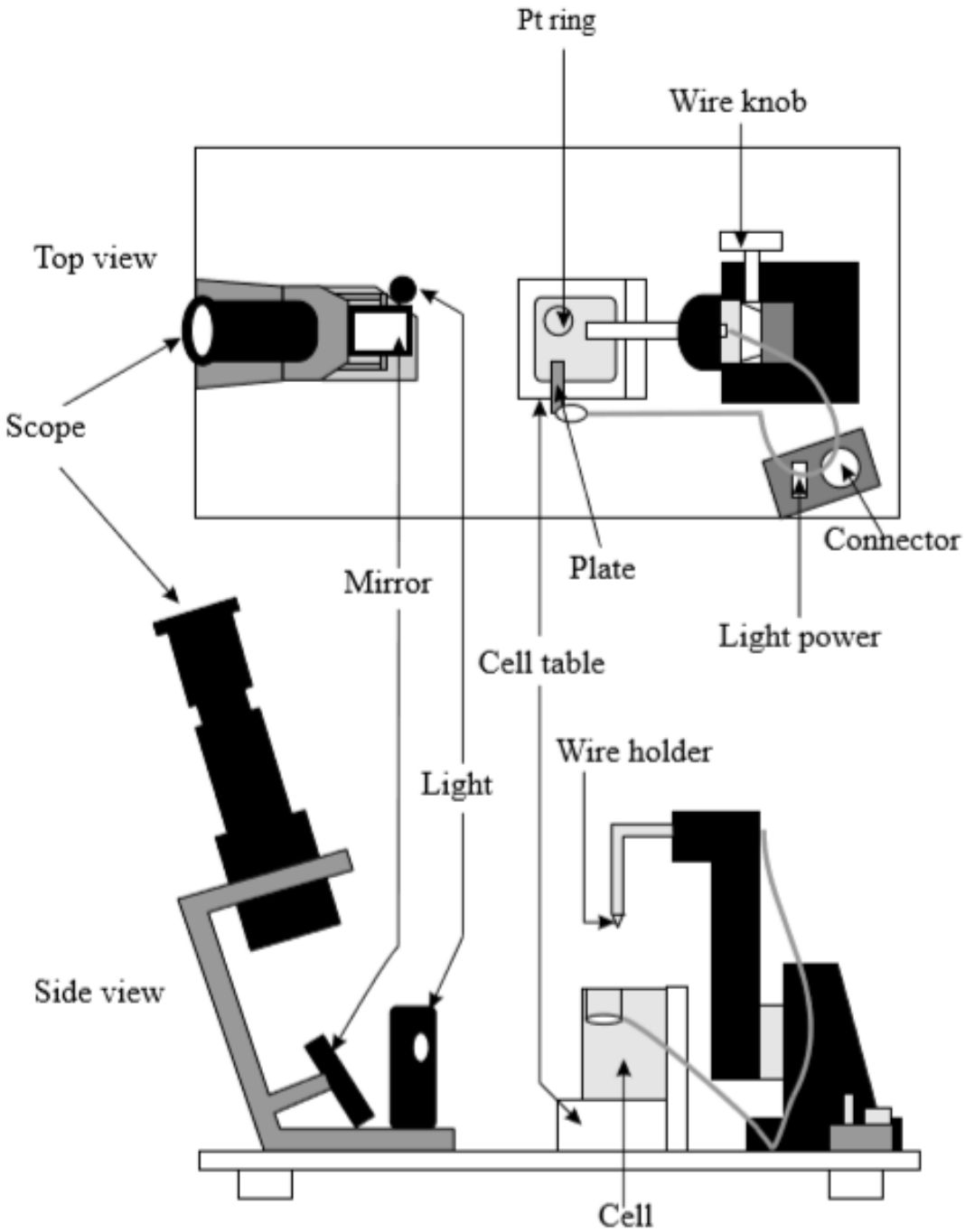


Figure 2.6: Tip etching system.

The shape of the tip depends on various conditions, temperature, amount of the solution, vibration of the liquid surface, etc. However, for reproducible high quality tip, using the condition: 1.2N-KOH (aq) and a voltage of 7 V, stop current of 2 mA is most favorable. A high concentration of potassium hydroxide and high voltage results in a thick and short tip with a large radius of curvature. Conversely, a low potassium hydroxide concentration and low voltage results in a sharp and long tip which tends to break during the rinsing procedure.

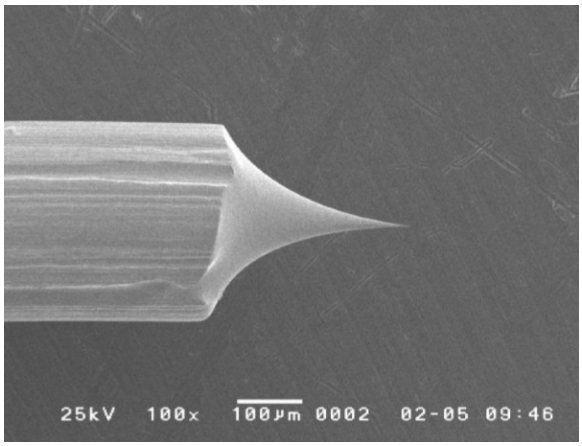


Figure 2.7: Scanning Electron Microscopic (SEM) image of resulting tip apex.

### Cleaning of tip

The tip may become oxidized or contaminated in air for an extended period of time. To avoid this, after inserting the tip in the preparation chamber, the tip apex is cleaned in ultra-high vacuum environment just before the experimental measurements by heating the tip apex by electron bombardment. A schematic of tip cleaning assembly is shown in figure 2.8. A high voltage is applied to heat the filament and an accelerating voltage is applied between the tip and filament so that tip apex can be heated by electron bombardment.

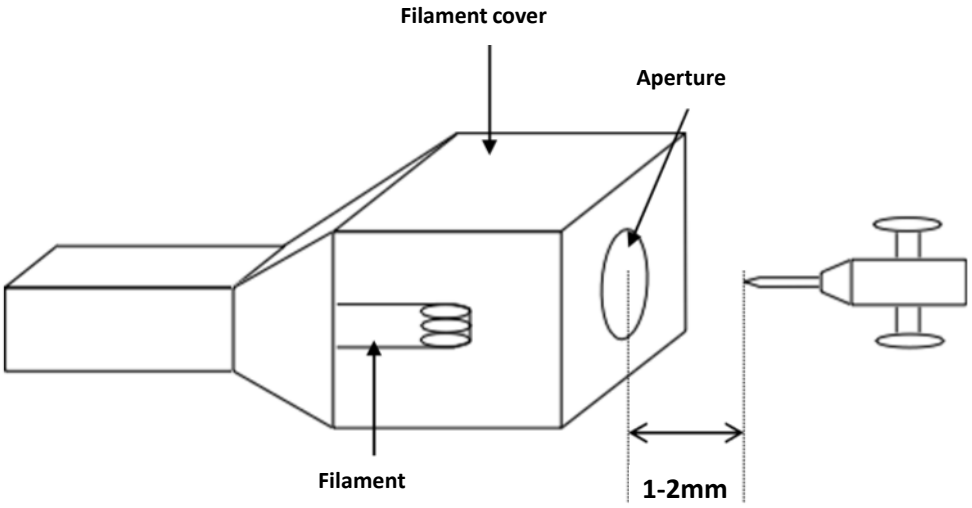


Figure 2.8: Schematic of tip cleaning assembly.

### Cleaving of single crystals

To avoid the oxidation and surface contamination the single crystals were cleaved in ultra-high vacuum environment before starting the experiments. First, we fix a wire/bar on the cleaving surface using silver epoxy and then insert the sample holder with sample in the preparation chamber. Using liquid nitrogen, we cool the samples down to 77 K and cleave the surface by hitting that wire using a manipulator. A picture of such an arrangement is shown in figure 2.9. Right after the cleaving we insert the sample directly to the STM head and start the cooling process down to milli-Kelvin temperatures.

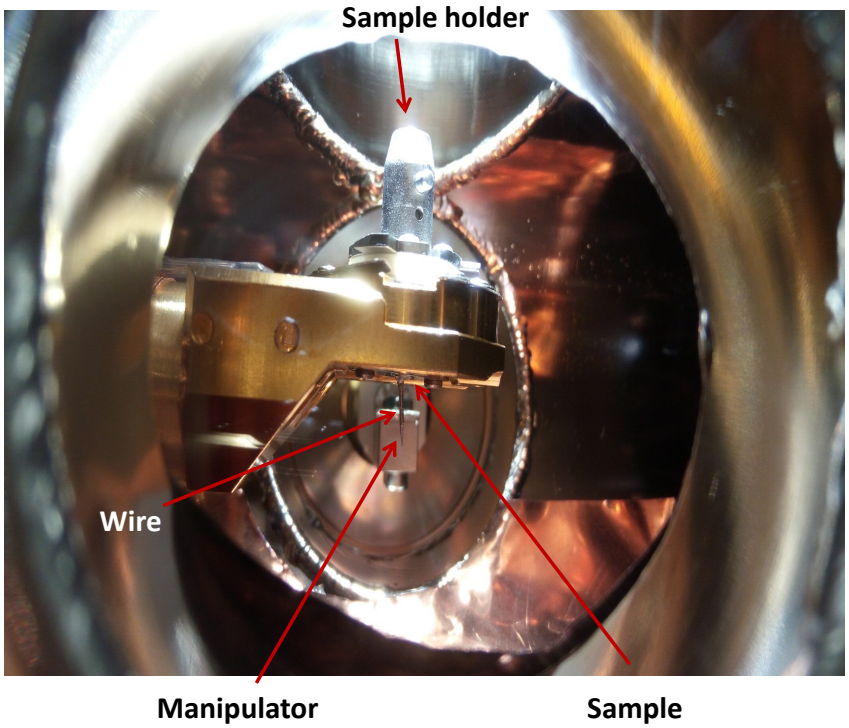


Figure 2.9: A picture of sample cleaving arrangement.

## 2.3 Point-contact spectroscopy technique

I have also used Point-Contact Andreev Reflection (PCAR) Spectroscopy [9,10] in some of the transport measurements. Here, I will discuss briefly the main aspects of this technique.

### 2.3.1 Point-Contact Andreev Reflection Spectroscopy (PCAR):

This technique is conventionally similar to the tunneling spectroscopy except that in PCAR spectroscopy tip touches the sample physically and there is no tunneling gap between the tip and the sample. The technique simply shows scattering mechanism at the normal metal and superconductor (NS) junction. A schematic describing the point-contact between tip and the sample is shown in figure 2.10. Point-contact spectroscopy is a powerful technique to extract the energy and momentum resolved information of the materials. It can be used to measure the superconducting energy gap and the symmetry properties of the gap (isotropic or anisotropic gap), [11, 12] spin-polarization of ferromagnets and information about the phonon spectra of the materials. If the diameter of the contact is of the order of characteristic length scales (like the elastic and inelastic mean-free path of the electrons) of the materials then this contact is called point-contact. Figure 2.10 defines that there are two contacts attached to the tip and another two are attached to the sample. Across the point-contact we measure the voltage drop using a lock-in amplifier at a particular frequency by sending a small amount of modulated current ($I_{dc} + I_{ac}\sin\omega t$) using Keithley current source and lock-in amplifier.

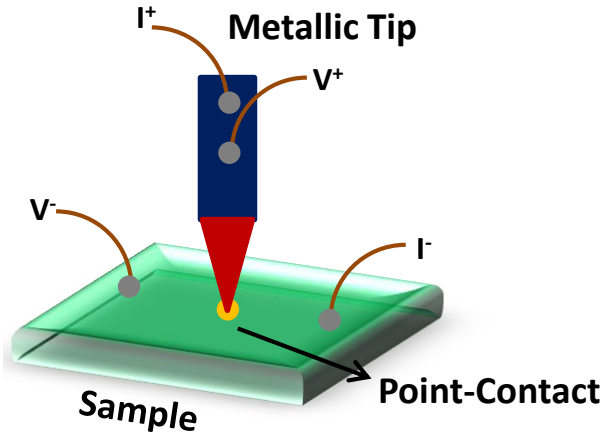


Figure 2.10: The Schematic of Point-Contact Spectroscopy.

The resistance of such a point-contact is given by Wexler's formula [13] $R_{pc} = \frac{(2h/e^2)}{(ak_F)^2} + \Gamma(l/a)\frac{\rho(T)}{2a}$. Where h is the Planck's constant, a is the diameter of point-contact, $\rho$ is the bulk resistivity of the material. The spectroscopy is performed in different regimes of point-contact called ballistic, thermal and intermediate regimes. Different regimes of point-contact depend

upon the diameter of contact of tip and sample relative to the mean free path of the excitations. The superconducting gap can be measured from dV/dI vs V spectrum (taken in ballistic regime of the point-contact) after fitting it with BTK theoretical equation. Blonder-Tinkham- Klapwijk (BTK) [14] have given the theoretical understanding of PCAR Spectroscopy.

### 2.3.2 Electronic transport in different regimes

Transport spectroscopy can be performed in different regimes of point-contacts by comparing the mean free path ($l$) of the electrons and the contact diameter ($a$).

#### Thermal regime

In thermal regime, the contact diameter is much greater as compare to the elastic and inelastic mean free path ($a >> l$) then the electrons undergo scattering (both elastic and inelastic) within the contact region. In such contacts, the spectroscopy is dominated by bulk transport properties. Maxwell has given the formula for resistance known as **Maxwell's resistance** of such contacts by solving the Poisson equation with relevant boundary conditions. Maxwell's formula for resistance is following

$$R_M = \frac{\rho(T)}{2a}$$

where, $\rho$ is the resistivity of the material.

In this regime, during the transport, electrons dissipate energy within the contact region leading to the joule heating consequently increase the local temperature of the contact with respect to the bath temperature ($T_{bath}$). The effective temperature ($T_{eff}$) increases with applied voltage (V) due to which the energy resolved information can not be obtained in thermal regime. [15]

#### Ballistic regime

When the contact diameter is much smaller than the elastic mean free path of the electrons ($l$ » $a$) then the contact behaves like ballistic contact and electrons do no undergo any scattering within the contact region. In such contact, energy does not dissipate and electrons gain energy and move ballistically within the contact region when a voltage is applied. In 1965, Sharvin [16] derived an expression by solving the problem of dilute gas through a small hole following the Knudsen's scheme. This expression defines the contact resistance in the ballistic regime and known as the **Sharvin's Resistance**. The formula for Sharvin's resistance is given

as follows

$$R_S = \frac{2h}{e^2(ak_F)^2}$$

where, $k_F$ is the Fermi wave vector and $e$ represent the charge of the electron.

In this regime of contact, electrons gain enough energy and excite the elementary excitations like phonon and magnons which gives rise to non-linearity in the I-V characteristics. That is how energy resolved spectroscopy is performed in the ballistic regime.

**Intermediate regime**

In intermediate regime, the contact diameter is approximately equal to the mean free path of the electrons ($a \approx l$). The contact resistance in this regime can be defined by including both the Maxwell's resistance part and the Sharvin's resistance part. The following is the **Wexler's formula**, which was obtained in 1966 by G. Wexler. [13]

$$R = R_S + \Gamma(l/a)R_M$$

where, $\Gamma(l/a)$ is a slowly varying function of the order of unity [17].

### 2.3.3 Transport phenomena at the interface

The transport phenomena of electrons at the interface of a normal metal and a superconductor can be understood by following the figure 2.11. At the left side density of states of a normal metal are shown, on the other side, the density of states of a superconductor are shown. When a voltage is applied across the interface, electrons gain energy and try to go to the other side. If the energy given to the electron is $E_1$ higher than the superconducting energy gap $\Delta$ then the electron will find state to the other side and transmitted through the interface. However, if the electronic energy is $E_2$ less than the superconducting energy gap $\Delta$, the electron will not find the states on the other side and will undergo reflection. Electron can reflect back in two ways 1) it can reflect back as it is i.e. as a electron with same spin known as normal reflection or 2) it can reflect back as a hole with opposite spin and subsequently there will be formation of cooper pair in the superconducting side at the Fermi-level leading to the conservation of momentum and spin, this reflection is known as Andreev reflection.

This phenomenon of Andreev reflection [18] and can be analyzed by normalized differential conductance $\frac{G(V)}{G_n}$ vs. V where G(V) = $\frac{dI}{dV}$ and V is the applied dc voltage. This $\frac{dI}{dV}$ and $V$ spec-

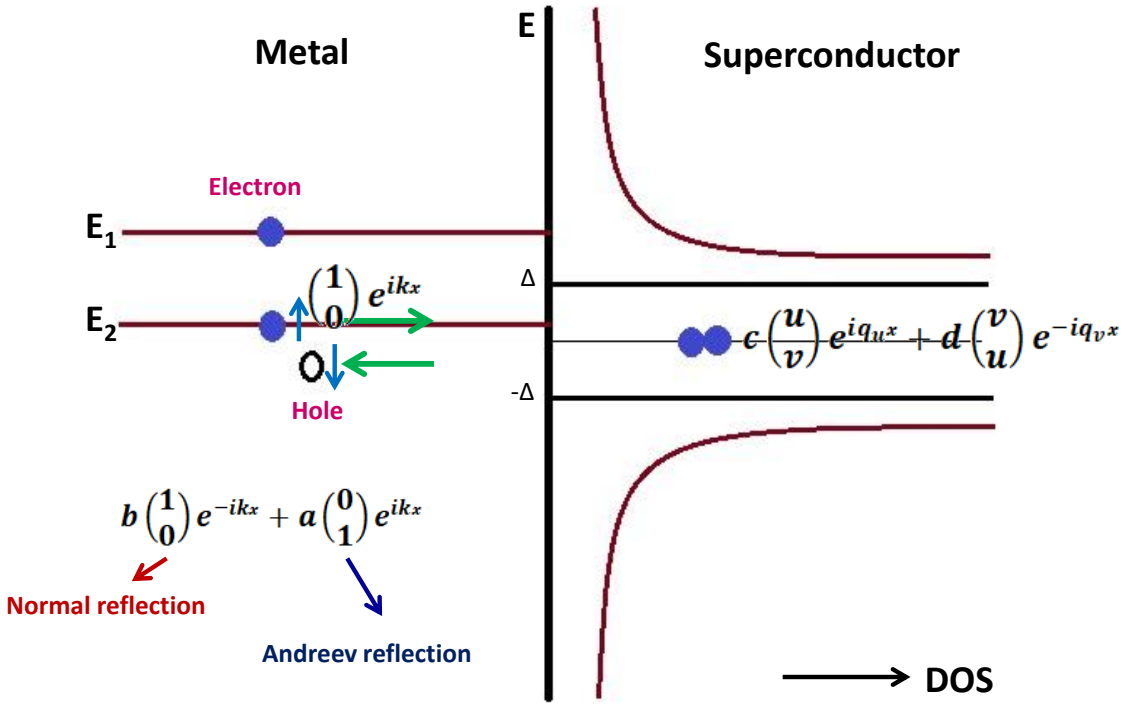


Figure 2.11: The Schematic of Point-Contact Andreev Reflection Spectroscopy showing the interface of a metal and a superconductor. $\begin{pmatrix}1\\0\end{pmatrix} e^{ikx}$ is the wavefunction of an electron approaching interface and $\begin{pmatrix}0\\1\end{pmatrix} e^{-ikx}$ is the wavefunction of a hole reflected back through the interface. $c\begin{pmatrix}u\\v\end{pmatrix} e^{iq_u x} + d\begin{pmatrix}v\\u\end{pmatrix} e^{-iq_v x}$ is the wavefunction of a cooper-pair propagating into the superconductor.

trum can be analyzed within the framework of Blonder-Tinkham-Klapwijk (BTK) theory. [14] Within the BTK theory, the interface of normal metal and superconductor is given by the delta function $H' = V_0\,\delta(x)$, where $x$ is perpendicular to the interface and $x = 0$ represent the interface.

The strength of the barrier potential is characterized by a dimension less parameter $Z = \frac{V_0}{\hbar v_F}$ (where $V_0$ is the potential , $\hbar$ is the planck's constant and $v_F$ is the Fermi velocity). This parameter z depends on two factors: (i) non-vanishing potential barrier at the interface of normal-metal and superconductor and (ii) the mismatch of Fermi velocities, $v_F$ is different for different materials. Therefore, the barrier potential strength can never be zero. Hence, electrons will always have some finite probability of normal reflection. If **A(E)** and **B(E)** are the probabilities of Andreev reflection and normal reflection, then, the current through the interface of normal

metal and superconductor can be described as

$$I_{N/S} \propto N(0)\, v_F \int_{-\infty}^{\infty} [f_0(E-eV) - f_0(E)][1 + A(E) - B(E)]dE \tag{2.4}$$

where, N (0) is the density of states at the Fermi level and $v_F$ is the Fermi velocity. The coefficient of **A(E)** and **B(E)** can be calculated by applying the appropriate boundary conditions for delta function and Bogoliubov-deGennes equation.

The values of **A(E)** = a*a and **B(E)** = b*b are shown in the following table.

| Coefficient | $E < \Delta$ | $E > \Delta$ |
|---|---|---|
| A(E) | $\frac{(\frac{\Delta}{E})^2}{1-\varepsilon(1+2Z^2)^2}$ | $\frac{(uv)^2}{\gamma^2}$ |
| B(E) | $1 - A(E)$ | $\frac{[u^2-v^2]^2 Z^2[1+Z^2]}{\gamma^2}$ |

**Table 2.1:** Probabilities of Andreev reflection and normal reflection with different energies.

In the above table, $\gamma^2$ = $[(u^2$ - $v^2$ $)Z^2$ + $u^2]^2$ and $\varepsilon$ = $\frac{E^2-\Delta^2}{E^2}$. Using equation 2.4, the experimental data can be fitted and the information about the superconducting energy gap can be obtained.

### 2.3.4 Measurement of transport spin polarization

Degree of spin-polarization can be measured by point-contact spectroscopy by replacing a normal metal to a ferromagnet. The Fermi-level of ferromagnet is spin-polarized i.e. total number of spin up and spin down channels are not equal. If ferromagnet is 100% polarized then there will be only one type of spin channel available. This difference can be probed by spin-polarized point-contact spectroscopy. A schematic in figure 2.12 showing the interface of 100% polarized ferromagnet and a superconductor. As it is clear from the picture shown in figure 2.12, the spin down states are not available for an electron to reflect back as a hole with opposite spin, thus, the Andreev reflection will be suppressed. The degree suppression can be evaluated by including some other parameters in the current equation.

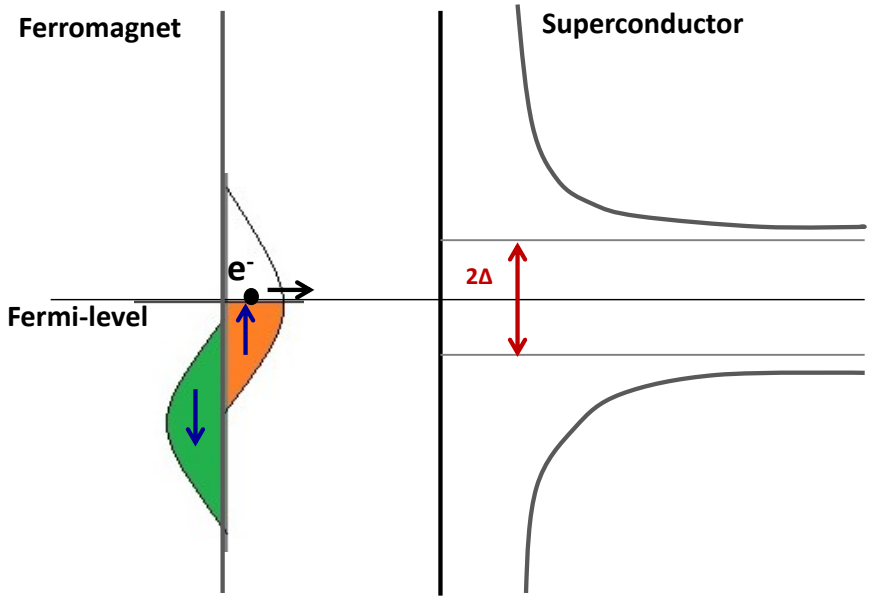


Figure 2.12: The schematic of Spin-Polarized Point-Contact Andreev Reflection Spectroscopy showing the interface of a ferromagnet and a superconductor.

As per BTK theory [14, 19] the current between a ferromagnet and a superconductor is given by

$$I_{mod} = (1 - P_t)I_u + P_t I_p$$

$I_u$ represents the unpolarized current, $I_p$ represents the polarized current and $P_t$ represents the degree of transport spin-polarization. After calculating the $I_u$ and $I_p$ we have simply written the total modified current including the transport spin polarization $P_t$. This equation is used to

fit the experimental $dI/dV$ curves to determine the transport spin polarization $P_t$. [20] Now the fitting parameters are $\Delta$, $Z$, $P_t$ and $\gamma$. The magnitude of spin-polarization ($P_t$) thus determined, it may decrease monotonically by increase in barrier strength ($Z$). Such a dependence is seen in spin polarization measurements using Andreev reflection spectroscopy and attributed to the process of spin-flip scattering which increases with the barrier strength. [21, 22] However, for certain materials, where spin dependent scattering are not present, any dependence of $P_t$ on $Z$ may not be observed.

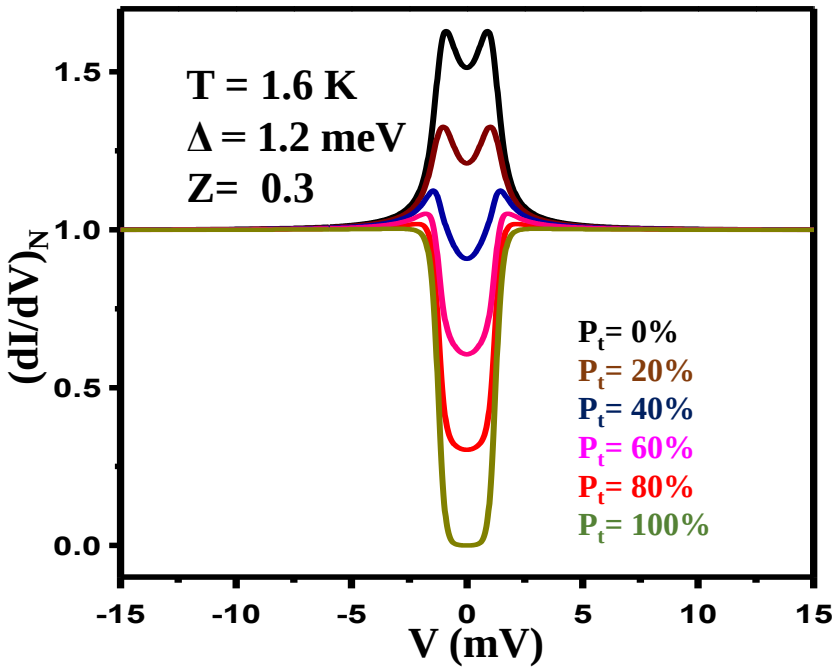


Figure 2.13: Simulated spectra for different degree of spin polarization of the transport current flowing through the point contacts using the modified BTK theory (as discussed in the text).

In figure 2.13, simulated spectra for different degree of transport spin-polarization is shown. Here we have used modified BTK theory to fit the spectra. [14]

### 2.3.5 PCAR Spectroscopy measurement system

A home built probe is used in PCAR experiments where measurement temperature down to 300mK can be obtained using a cryostat equipped with $He_4$ bath and $He_3$ pot. This system also dressed with vector magnet, 6 Tesla in z-direction and 1-1 Tesla in x, y direction. Here tip approaches the sample by piezo-walker.

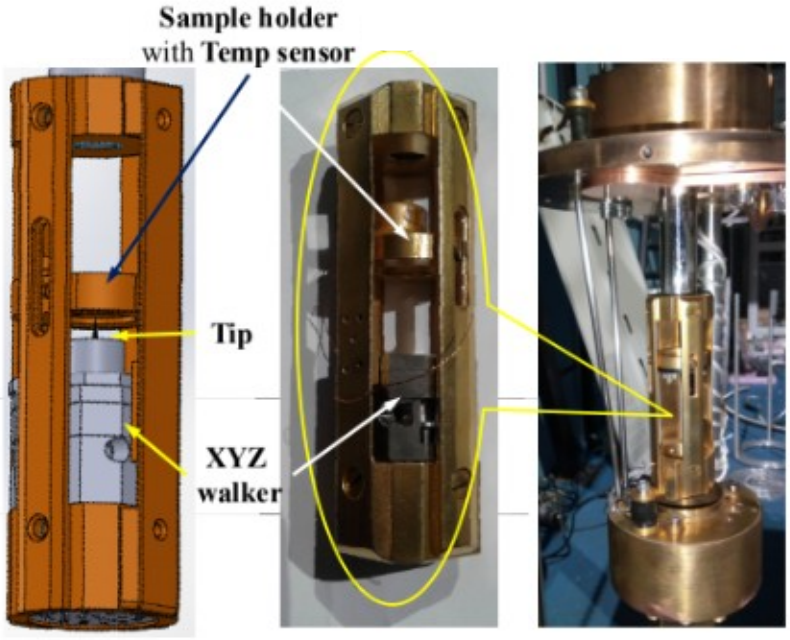


Figure 2.14: A picture of PCAR system showing an arrangement of piezo-walker and sample holder.

A picture of point-contact spectroscopy head is shown in figure 2.14. The left side picture is the solid works image and other two are the photographs of the existing head. Tip and sample are mounted between the sample plate and piezo walker. The tip can move in all three directions, thus, the contact region can also be changed without taking it out. A temperature sensor is mounted very close to the sample, the sample plate is made of cooper which has a higher thermal conductivity.

## 2.4 Comparison between STS and PCAR Spectroscopy

Scanning Tunneling Spectroscopy and Point Contact Andreev Reflection Spectroscopy are powerful and unique techniques by their own to probe the physics of electronic excitations in the condensed matter systems. There are few comparisons between these two techniques:

| **STM/STS Spectroscopy** | **PCAR Spectroscopy** |
|---|---|
| Surface sensitive technique | Also extract bulk properties such as transport spin-polarization |
| Spatial resolution is good | Energy and momentum resolved technique |
| Tunneling gap of finite width between tip and sample (see Fig.2.1) | Tip touches the sample physically (see Fig.2.10) |
| Transport takes place through tunneling barrier | Transport takes place through nano constriction formed at interface and can be controlled by the contact diameter |
| $I \propto \int_{-\infty}^{\infty} N_s(\varepsilon + eV)[f(\varepsilon) - f(\varepsilon + eV)]d\varepsilon$ | $I \propto \int_{-\infty}^{\infty} [f_0(E - eV) - f_0(E)][1 + A(E) - B(E)]dE$ |
| Works only in tunneling regime | Works in three regimes of transport: 1) Ballistic regime, 2) Thermal regime and 3) Intermediate regime |
| STM can produce atomically resolved images of samples also | PCAR only gives spectroscopic information |

**Table 2.2:** Comparison between STS and PCAR Spectroscopy.

## 2.5 Conclusions

In this chapter, I have described the experimental techniques including Scanning Tunneling Microscopy and Spectroscopy (STM/STS) and Point-Contact Andreev Reflection (PCAR) Spectroscopy. A complete description and working principle of Scanning Tunneling Microscope is discussed. I have also explained how to measure the transport spin-polarization by PCAR spectroscopy. These techniques are used in the experimental work which is presented in this desertion.

# Bibliography


[1] J. Tersoff, D. R. Hamann, Phys. Rev. B **31**, 805 - 813 (1985).

[2] I. Giaever, Phys. Rev. Lett. **5**, 147 (1960).

[3] I. Giaever, Rev. Mod. Phys. **46**, 245 (1974).

[4] J. Nicol, S. Shapiro, and P. H. Smith Phys. Rev. Lett. **5**, 461 (1960).

[5] J. Bardeen, Phys. Rev. Lett. **6**, 57 (1961).

[6] M. Tinkham, Introduction to Superconductivity McGraw-Hill, New York, (1996).

[7] J. Bardeen, L. N. Cooper, and J. R. Schrieffer, Phys. Rev. **108**, 1175 (1957).

[8] R. C. Dynes, V. Narayanamurti, and J. p. Garno, Phys. Rev. lett. **41**, 1509 (1978).

[9] Yu. G. Naidyuk, I. K. Yanson, Springer-Verlag New York (2005).

[10] F. Laube, G. Goll, H. V. Lohneysen, M. Fogelstrom, and F.Lichtenberg, Phys. Rev. Lett. **84**, 1595 (2000).

[11] T. Hanaguri, S. Nitaka, K. Kuroki and H. Takagi, SCIENCE VOL **328**, (2010).

[12] D. Daghero, M. Tortello, G.A. Ummarino, J.-C. Griveau, E. Colineau, R. Eloirdi, A.B. Shick, J. Kolorenc, A.I. Lichtenstein and R. Caciuffo, Nature Communication (2012).

[13] A. Wexler, Proc. Phys. Soc. **89**, 927-941 (1966).

[14] G. E. Blonder, M. Tinkham, T. M. Klapwijk, Phys. Rev. B **25**, 4515, (1982).

[15] G. Sheet, Point-Contact Andreev Reflection Spectroscopy on Superconductors and Ferromagnets, (2006).

[16] Yu. V. Sharvin, Sov. Phys. JETP **21**, (1965).

[17] Yu.G. Naidyuk, I. K. Yanson, Point-contact Spectroscopy, Springer, 2005.

[18] A. Andreev, Sov. Phys. JETP **19**, 1228.

[19] R. J. Soulen, *et al.* Science **282**, 85 (1998).

[20] I. I. Mazin, Phys. Rev. Lett. **83**, 1427 (1999).

[21] A. Sirohi, *et al.* Appl. Phys. Lett. **108** 242411 (2016).

[22] P. Raychaudhuri, A. P. Mackenzie, J. W. Reiner, & M. R. Beasley, Phys. Rev. B **67**, 020411 (2003).

Chapter 3

# STM studies on gallide compound $Mo_8Ga_{41}$

In this chapter, the nature of superconductivity is investigated in the compound of gallide family $Mo_8Ga_{41}$. A clear evidence of multiband superconductivity is observed from the direct measurement of superconducting gap in tunneling experiments. The work presented in this chapter is already published in ref [1].

## 3.1 Introduction

In the past few decades, the objective to investigate the superconductors was either to find superconductors with high critical temperatures or to find unconventional superconductors that deviates from the BCS model. Several Mo-based compounds attract attention considering both the objectives. Mo-based carbides manifest relatively higher critical temperatures e.g. $\gamma$-MoC 68 (9.3 K) [2] and $Mo_3Al_2C$ (9.05 K) [3]. Among the Mo-based compounds, the complex low-temperature behavior in $Mo_3Sb_7$ is attributed to the coexistence of superconductivity and spin fluctuations, [4, 5] thus resembling the superconductivity with strong electronic correlations. Like many other families of Mo-based superconductors, the superconductivity in gallium cluster compounds might also emerge through complex pairing mechanism and host unconventional physics. Indication of such complex pairing has already been obtained in $PuCoGa_5$ where it was argued that the antiferromagnetic fluctuations lead to the superconducting pairing [6–8]. Matthias rule predicts higher critical temperatures, [9] based on the higher density of states at the Fermi-level is partly followed by the endohedral gallide cluster compounds for lower valence counts. For higher valence counts, the architecture of the cluster packing plays a dominant role which decides the $T_c$. As the density of states goes up the $T_c$ goes down. This competition makes $Mo_8Ga_{41}$, the highest critical temperature superconductor in the family. [10, 11] Based on a number of experiments that were employed to analyze the superconducting phase of $Mo_8Ga_{41}$, it was shown that this compound manifests surprisingly high electron-phonon

coupling resulting in a large $\Delta/k_BT_c$ ratio [12]. Additionally, an indication of multiband superconductivity was also found in $\mu$SR experiments [12, 13].

## 3.2 Experimental details

### 3.2.1 Sample Details

All the samples of $Mo_8Ga_{41}$ were synthesized by solid-state reaction method. The constituent elements of Mo (99.999%) powder and Ga (99.999%) pieces were mixed in a stoichiometric ratio in a quartz ampoule. First, the quartz ampoule was evacuated down to $10^{-4}$ mbar and heated up to $850^oC$ and then cooled down to room temperature very slowly. The resulted samples appeared shiny grey. The formation of $Mo_8Ga_{41}$ in single phase was confirmed by powder X-ray diffraction and analyzed by Rietveld fitting. A superconducting transition at $T_c \sim$ 10 K was found from both temperature dependent resistivity and magnetization measurements.

#### Crystal Structure of $Mo_8Ga_{41}$

In figure 3.1 we show a theoretically obtained crystal structure of $Mo_8Ga_{41}$. The crystal structure of $Mo_8Ga_{41}$ is rhombohedral with the space group of $R\bar{3}$ (# 148). The relaxed lattice parameters are $a = b = c = 9.5788$ and $\alpha = \beta = \gamma = 94.974^o$, which are in good agreement with the experimental values reported before [11]. In the crystal structure of $Mo_8Ga_{41}$ Ga atoms are forming polyhedron by surrounding one Mo atom as shown in figure 3.1 [10].

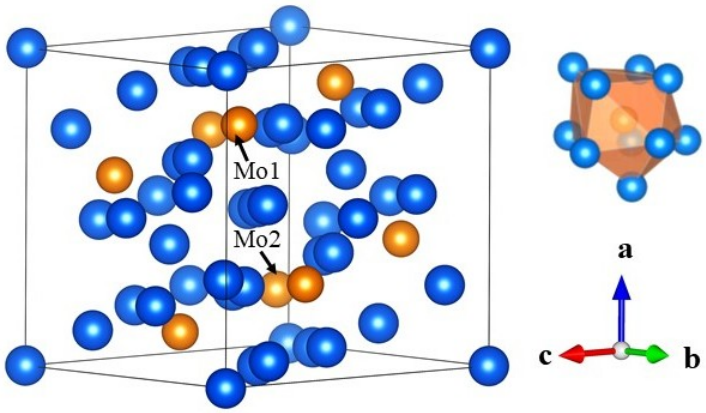


Figure 3.1: Crystal structure of $Mo_8Ga_{41}$.

### 3.2.2 Measurement Details

All the measurements were carried out by Scanning Tunneling Microscope (STM) in an ultra-high vacuum (UHV) cryostat at temperatures down to 300 mK. The STM is equipped with a

sample preparation chamber which is maintained in UHV conditions. In the preparation chamber, few layers of the sample were first removed by mild argon ion sputtering just before the STM/STS experiments. This ensured that the surface of the sample is clean and we probed the pristine surface of $Mo_8Ga_{41}$.

## 3.3 STM/STS measurements on $Mo_8Ga_{41}$

Figure 3.2 (a) displays a topographic image (20 nm x 20 nm) of the surface of $Mo_8Ga_{41}$ measured in constant current mode with $I = 150\,pA$ and $V = 1.1V$. The topographic image showing distinctly visible grains with average grain size of $\sim$ 5 nm. To extract the spectroscopic informations, the STM tip is brought close to the grains and recorded the $dI/dV$ vs. $V$ spectra. One such representative tunneling spectrum is shown in figure 3.2 (b) with two coherence peaks symmetric about $V = 0$mV. The tunneling spectrum confirms the formation of superconducting energy gap. Further, we measured a large number of spectra all over the crystal surface and fitted by the theoretical equation of tunneling current to calculate the superconducting energy gap.

In figure 3.3 we show two representative spectra with Dyne's fits [14]. First we used single superconducting gap to fit the spectra. As it is clear from the figure 3.3 that fitting deviates from the experimental spectra significantly, while, these are the best-fitted spectrum using a single gap. To fit these spectra accurately we used a tunneling current equation within the two band model [16, 17]. We show such spectra with both single and double gap fitting in figure 3.3. The green line is a theoretical fit using single gap while black solid line shows fit using two gaps.

Within the two band model, the tunneling current will have contributions from both the bands. Therefore, the total tunneling current $I_{total} = \alpha I(V,\Delta_1,\Gamma_1) + \beta I(V,\Delta_2,\Gamma_2)$, where $\Delta_1$ and $\Delta_2$ are the gaps formed in the two different bands and $\Gamma_1$ and $\Gamma_2$ are the corresponding effective broadening parameters. $\Gamma_1$ and $\Gamma_2$ also include the effective inter-band scattering, if any. $\alpha$ and $\beta$ represent the relative contribution from the two superconducting bands to the total tunneling current. Physically, $\alpha$ and $\beta$ could be associated with the crystal facet that the tip predominantly probes and how the crystallographic axis of a particular grain is oriented with respect to the direction of tunneling current. $\alpha$ and $\beta$ might vary significantly when tip moves from one particular orientation of grain to the other. As it is seen in the figure 3.3, the theoretically generated spectra within the simplistic two band model fit remarkably well with the experimentally obtained spectra revealing the existence of two gaps with the magnitude of $\Delta_1 \sim 1.6$ meV and $\Delta_2 \sim 0.9$ meV respectively.

In order to confirm further the two band nature, we explored a large number of tunneling spectra on different regions and grains. For certain grains, we were able to observe the

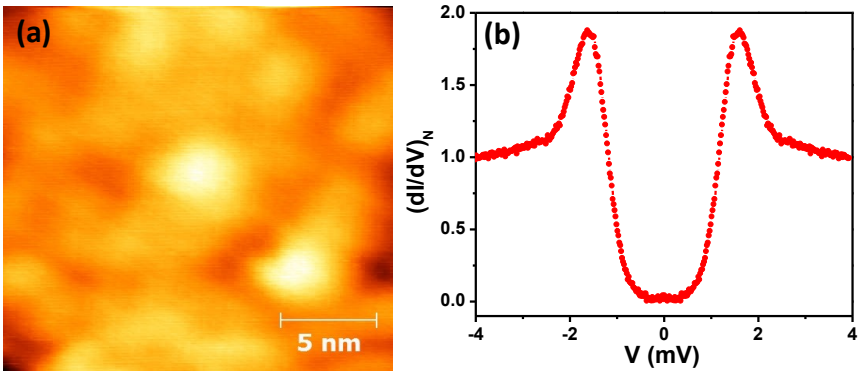


Figure 3.2: Topography of $Mo_8Ga_{41}$ **(a)** STM topographic image of the surface of $Mo_8Ga_{41}$ showing distinctly visible grains. **(b)** Tunneling spectrum ($dI/dV$ vs $V$ plot) taken on one of the grains clearly shows the formation of superconducting energy gap.

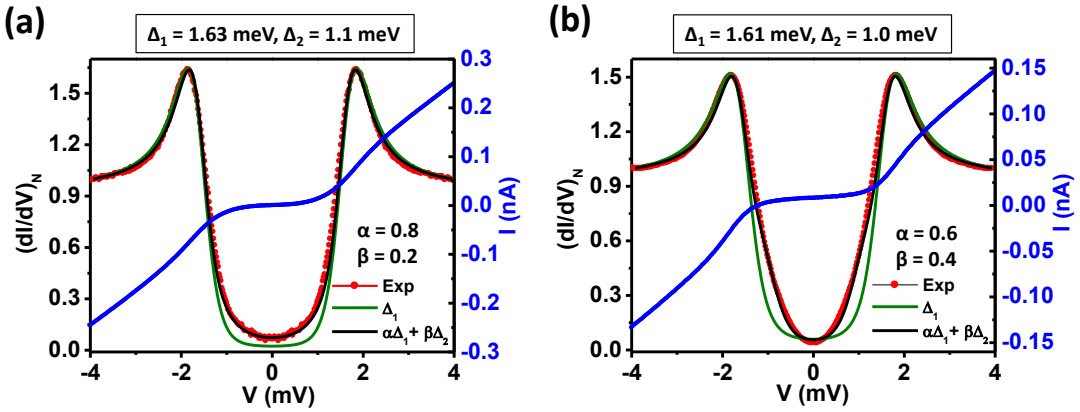


Figure 3.3: **(a, b)** Two representative tunneling spectra with Dyne's fitting. The green solid line is a fit within the single band model while the black solid line is a fit within the two band model. Red dots are the experimental data. The contributions ($\alpha$ and $\beta$) of both the gaps ($\Delta_1$ and $\Delta_2$) are given in the respective insets.

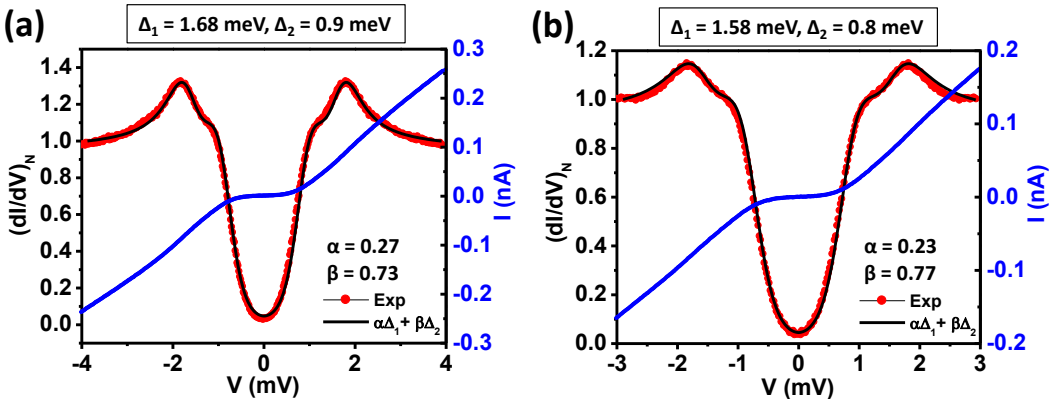


Figure 3.4: (a, b) Two representative tunneling spectra demonstrating two clear gaps. The black solid line is a theoretical fit within the two band model using Dyne's formula. The contributions ($\alpha$ and $\beta$) of both the gaps ($\Delta_1$ and $\Delta_2$) are given in the respective insets.

"two-gap" feature in a single tunneling spectrum. Two such representative spectra along with two-gap fits are shown in figure 3.4. The gap amplitude for the smaller gap and the larger gap remained approximately same as before. For these spectra, the contribution of $\alpha$ turned out to be smaller than $\beta$. These observations are consistent with the understanding that the two-gap feature can be seen in a single spectrum when the band corresponding to the smaller gap has a larger contribution to the tunneling current. These two gap features are strikingly similar to the two band superconductor $MgB_2$ [18–25].

### 3.3.1 Magnetic field dependence of $dI/dV$ vs. $dV$ spectrum

To understand the effect of the magnetic field, we now focus on the magnetic field dependence of the superconducting energy gap measured on $Mo_8Ga_{41}$. We have used the same formula that was used to fit the zero-field spectra and extracted the values of the superconducting energy gaps. The field dependence of the spectra with fittings is shown in Figure 3.5 (a). The extracted gap values are plotted as a function of magnetic field and shown in Figure 3.5 (b).

The larger gap ($\Delta_1$) decreases slowly with magnetic field and attains 53% of its zero field value at a magnetic field of 6 Tesla. Beyond 6 Tesla magnetic field, the reasonable estimate of the gap was not possible. On the other hand, the smaller gap ($\Delta_2$) decreases rapidly with increasing magnetic field. At a field of 6 Tesla, the gap $\Delta_2$ becomes 0.15 meV which is only less than 15% of the gap at zero field. This variation of the two gaps in $Mo_8Ga_{41}$ is similar to the variation of the two gaps with magnetic field in $MgB_2$. The small gap in $MgB_2$ is seen to almost disappear at a magnetic field of approximately 1 Tesla while the large gap remains almost unaffected in this range of magnetic field [22]. Furthermore, this observation is also consistent with the theoretical calculations of the vortex state of a multi-band superconductor

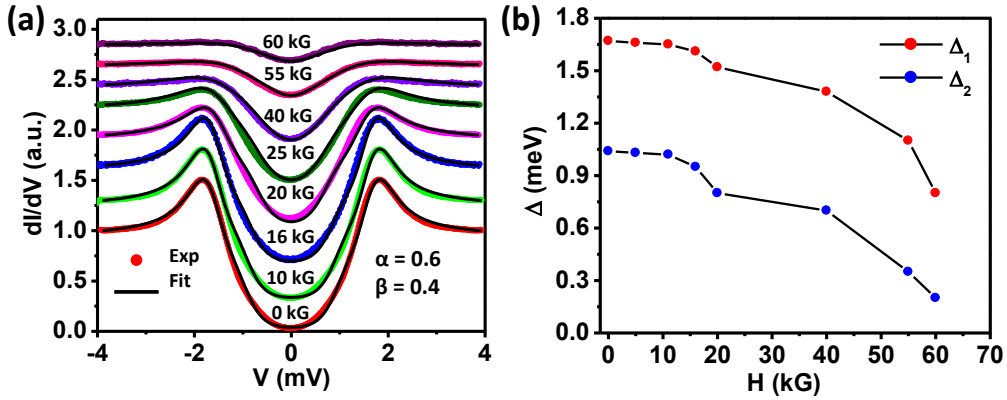


Figure 3.5: (a) Magnetic field dependence of $dI/dV$ vs. $dV$ spectrum with theoretical fittings within the two band model. (b) Extracted values of $\Delta_1$ and $\Delta_2$ are plotted as a function of $H$.

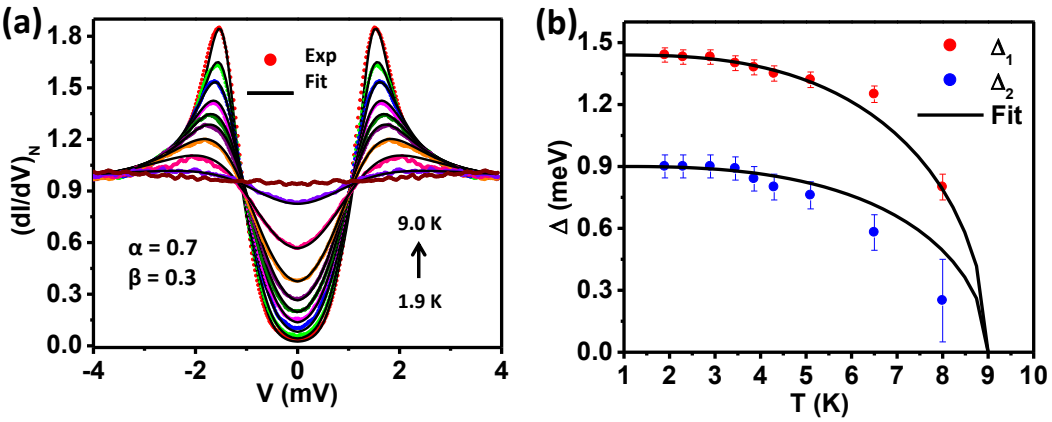


Figure 3.6: (a)Temperature dependence of $dI/dV$ vs. $dV$ spectrum with theoretical fittings within the two band model. (b) Extracted values of $\Delta_1$ and $\Delta_2$ are plotted as a function of $T$. The black solid lines in panel (b) are the theoretical temperature dependence as per BCS theory. The red and blue dots are the experimental data corresponding to $\Delta_1$ and $\Delta_2$ respectively.

with weak interband scattering [26, 27]. The estimated value of $2\Delta_1/k_BT_c$ for the larger gap of $Mo_8Ga_{41}$ is found to be 3.5 which is close to the expected value for a BCS superconductor in a weak-coupling limit [15]. This suggests that the critical temperature $T_c$ in $Mo_8Ga_{41}$ is governed by the larger gap ($\Delta_1$). This is similar to $MgB_2$ and $YNi_2B_2C$, where interband scattering is weak [28]. These observations are again consistent with the theoretical expectation for a multiband superconductor with weak interband scattering [26, 27].

### 3.3.2 Temperature dependence of $dI/dV$ vs. $dV$ spectrum

In Figure 3.6 (a), we show the temperature dependence of one representative spectrum. The colored dots represent the experimentally obtained spectra. Both the gaps gradually decrease with increasing temperature and the features associated with superconductivity disappear com-

pletely above 9 K. The values of $\alpha$ and $\beta$ remained fixed for the entire range of temperature. The two gaps are extracted (red and blue dots) and plotted as a function of temperature in Figure 3.6 (b). The black solid lines show the theoretical temperature dependence expected as per BCS theory [15] for both the individual gaps with same $T_c$. It is clear from the figure 3.6 (b) that the larger gap ($\Delta_1$) follows BCS temperature dependence whereas the smaller gap remains almost constant up to 4 K and then starts decreasing gradually. It disappears at $\approx$ 9 K and showing a slight deviation from the BCS temperature dependence (black solid line) [15]. Since both the gaps are disappearing at the approximately same temperature, therefore it excludes the possibility of stoichiometric disorder in the grains of the crystal.

## 3.4 Theoretical findings

In order to understand the origin of multiband superconductivity in $Mo_8Ga_{41}$, we investigated the theoretical band structure calculations. The first-principle calculations are performed within the framework of density functional theory (DFT) [29, 30] using generalized gradient approximation (GGA) [31] of the Perdew-Burke-Ernzerhof (PBE) [31] form for the exchange-correlation functional as implemented in the Vinea Ab-initio Simulation Package (VASP). In figure 3.7, we present the main theoretical results. We evaluated the site and orbital resolved density of states $N_\sigma(0)$ at the Fermi level and compared them in Figure 3.7 (b). It is noticeable in figure 3.7 (b) that only Mo1 and Mo2 sites contribute strongly to the Fermi surface. Among all the $d$-orbitals of the Mo atoms, $d_{xz}/d_{yz}$, and $d_{x^2-y^2}$ orbitals have strongest contributions, while the other orbitals and Mo atoms have significantly lower contributions to the low-energy states at the Fermi-level.

In figure 3.7 (a), we show the band dispersion of the paramagnetic phase along the high-symmetric momenta directions. There are four bands which are crossing the Fermi level with considerable three-dimensionality. The corresponding 3D views of the Fermi surfaces are shown in figure 3.8 with Fermi velocities plotted as a color map. There are two concentric hole pockets around the Γ-point and one tiny electron pocket around the Brillouin zone corner. In addition, we also find a large and strongly anisotropic Fermi surface all over the Brillouin zone, a typical feature in this class of materials. In superconducting iron-pnictide family, the multiple superconducting gaps originate due to the multiband Fermi surface topology [32]. By projecting the orbital weights of iron atoms onto the Fermi surface topology, recent reports found an exotic orbital selective behavior of the superconducting order parameter. This orbital selective characteristic provide important clues of the superconducting pairing interaction mediated by orbital fluctuations (or entangled spin-orbital fluctuation owing to strong Hund's coupling in iron-pnictides). On the same footing, our observation of site-selective behavior on the low-energy electronic structure paves the way for a new mechanism of site-fluctuations induced pairing interaction responsible for superconductivity in $Mo_8Ga_{41}$.

In figure 3.8, the distribution of Fermi velocity in different bands is shown as color maps on the four Fermi surfaces. We observe that the average velocity on the two pockets around the Γ-point is significantly larger than that around the other pockets. From the qualitative understanding of the phonon mediated pairing, it can be rationalized in such a way that for two different bands taking part in superconductivity, when the average Fermi velocity in a band is significantly larger than that in the other band, the superconducting gap forming on the band with higher average Fermi velocity should be lower than that forming in the other band. The band with relatively slower electrons form a stronger superconducting energy gap. A similar observation was made in case of the multiband superconductor $YNi_2B_2C$ [28].

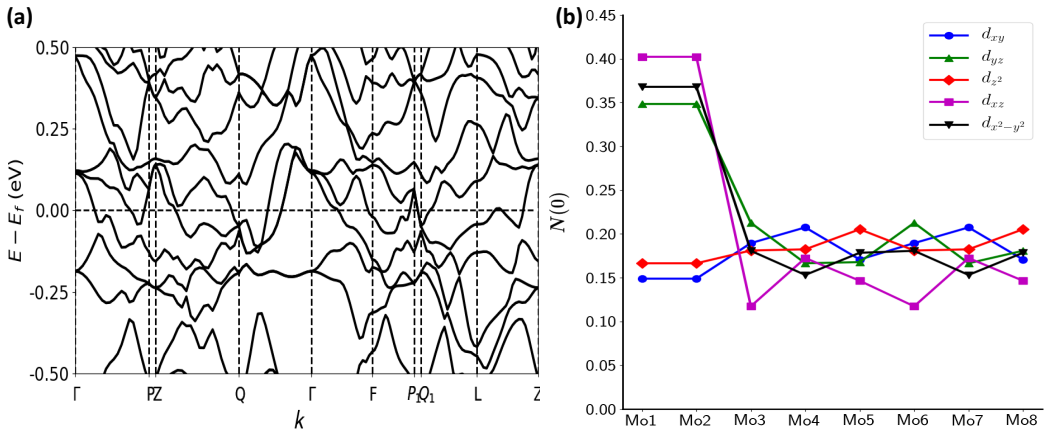


Figure 3.7: (a) Computed band structure of the paramagnetic phase along the high-symmetric momenta directions. (b) The contributions of Mo atoms and different orbitals to the total density of states at the Fermi-surface. It shows that superconductivity is site selective.

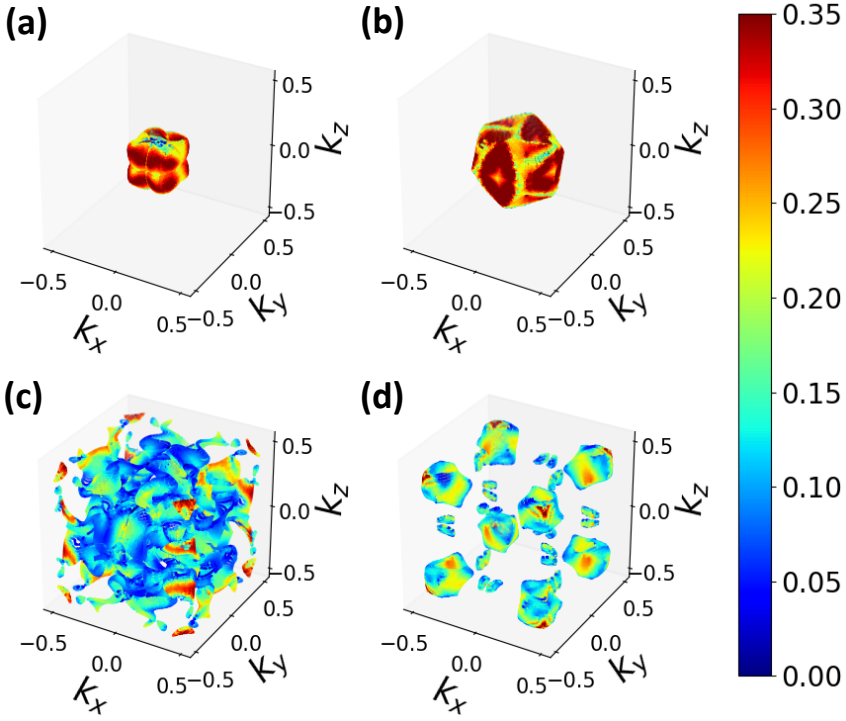


Figure 3.8: (a-d) 3D Fermi-surface with Fermi velocities plotted as a color map.

Hence, based on these theoretical analysis, it can be said that the smaller gap is forming in the bands shown in figure 3.8 (a or b) while the larger gap is forming in the bands shown in figure 3.8 (c or d). It is also noticed that the Mo1 and Mo2 sites contributes equally to the density of states at the Fermi-level. Therefore, the difference in the superconducting gaps is originating due to the difference in the Fermi velocities in the respective bands.

## 3.5 Summary

We have provided the direct spectroscopic evidence of multiband superconductivity in the endohedral gallide compound $Mo_8Ga_{41}$ with the theoretical first-principle band structure calculations. The conclusions are based on the direct spectroscopic measurements of the superconducting energy gaps and the observation of multiband superconductivity is consistent with the conclusions drawn from the $\mu$SR and specific heat measurements [12, 13]. The main findings are summarized below:

- We found two clear superconducting energy gap in the tunneling spectra which provides the direct evidence of multiband superconductivity in $Mo_8Ga_{41}$.
- Analysis of the temperature dependent data reveals that both the gaps follow temperature dependence as per BCS theory.
- The theoretical calculations revealed a unique site-selective characteristic that facilitates the observed multiband superconductivity in $Mo_8Ga_{41}$.

## 3.6 Acknowledgements

In this chapter, theoretical calculations are performed by Surabhi Saha and Dr. Tanmoy Das from IISC Bangalore. Samples are provided by Prakriti Neha and Prof. Satyabrata Patnaik from JNU Delhi.

# Bibliography


[1] A. Sirohi, S. Saha, P. Neha, S. Das, S. Patnaik, T. Das and G. Sheet, Phys. Rev. B **99**, 054503 (2019).

[2] C. P. Poole, Handbook of Superconductivity (Academic, London, 2000).

[3] E. Bauer, G. Rogl, X. Q. Chen, R. T. Khan, H. Michor, G. Hilscher, E. Royanian, K. Kumagai, D. Z. Li, Y. Y. Li, R. Podloucky, and P. Rogl, Phys. Rev. B **82**, 064511 (2010).

[4] C. Candolfi, B. Lenoir, A. Dauscher, C. Bellouard, J. Hejtmanek, E. Santava, and J. Tobola, Phys. Rev. Lett. **99**, 037006 (2007).

[5] V. H. Tran, W. Miiller, and Z. Bukowski, Phys. Rev. Lett. **100**, 137004 (2008).

[6] E. D. Bauer, M. M. Altarawneh, P. H. Tobash, K. Gofryk, O. E. Ayala-Valenzuela, J. N. Mitchell, R. D. McDonald, C. H. Mielke, F. Ronning, J.-C. Griveau, J. Phys.: Condens. Matter **24**, 052206 (2012).

[7] N. J. Curro, T. Caldwell, E. D. Bauer, L. A. Morales, M. J. Graf, Y. Bang, A. V. Balatsky, J. D. Thompson, and J. L. Sarrao, Nature **434**, 622 (2005).

[8] D. Daghero, M. Tortello, G.A. Ummarino, J.-C. Griveau, E. Colineau, R. Eloirdi, A.B. Shick, J. Kolorenc, A.I. Lichtenstein, and R. Caciuffo, Nature Communications **3**, 786 (2012).

[9] Matthias B, Phys. Rev. **97** (1), 74–76 (1995).

[10] W. Xie, H. Luo, B. F. Phelan, T. Klimczuk, F. A. Cevallos, and R. J. Cava, PNAS **112** (51), E7048-E7054 (2015).

[11] A. Bezinge, K. Yvon, M. Decroux, and J. Muller, J. Less Common Met. **99**, L27 (1984).

[12] V. Yu. Verchenko, A. A. Tsirlin, A. O. Zubtsovskiy, and A. V. Shevelko, Phys. Rev. B **93**, 064501 (2016).

[13] V. Yu. Verchenko, R. Khasanov, Z. Guguchia, A. A. Tsirlin, and A. V. Shevelko, Phys. Rev. B **96**, 134504 (2017).

[14] R. C. Dynes, V. Narayanamurti, and J. p. Garno, Phys. Rev. Lett. **41**, 1509 (1978).

[15] J. Bardeen, L. N. Cooper, and J. R. Schrieffer, Phys. Rev. **108**, 1175 (1957).

[16] H. Suhl, B. T. Matthias, and L. R. Walker, Phys. Rev. Lett. **3**, 552 (1959).

[17] E. J. Nicol, and J. P. Carbotte, Phys. Rev. B **71**, 054501 (2005).

[18] J. A. Silva-Guillen, Y. Noat, T. Cren, W. Sacks, E. Canadell, and P. Ordejon, Phys. Rev. B **92**, 064514 (2015).

[19] F. Giubileo, D. Roditchev, W. Sacks, R. Lamy, D. X. Thanh, J. Klein, S. Miraglia, D. Fruchart, J. Marcus, and P. Monod, Phys. Rev. Lett. **87**, 177008 (2001).

[20] H. Schmidt, J. F. Zasadzinski, K. E. Gray, and D. G. Hinks, Phys. Rev. Lett. **88**, 127002 (2002).

[21] P. Szabo, P. Samuely, J. Kacmar cık, T. Klein, J. Marcus, D. Fruchart, S. Miraglia, C. Marcenat, and A. G. M. Jansen, Phys. Rev. Lett. **87**, 137005 (2001).

[22] R. S. Gonnelli, D. Daghero, G. A. Ummarino, V. A. Stepanov, J. Jun, S. M. Kazakov, and J. Karpinski, Phys. Rev. Lett. **89**, 247004 (2002).

[23] F. Bouquet, R. A. Fisher, N. E. Phillips, D. G. Hinks, and J. D. Jorgensen, Phys. Rev. Lett. **87**, 047001 (2001).

[24] X. K. Chen, M. J. Konstantinovic, J. C. Irwin, D. D. Lawrie, and J. P. Franck, Phys. Rev. Lett. **87**, 157002 (2001).

[25] M. Iavarone, G. Karapetrov, A. E. Koshelev, W. K. Kwok, G. W. Crabtree, D. G. Hinks, W. N. Kang, E.-M. Choi, H. J. Kim, H.-J. Kim et al., Phys. Rev. Lett. **89**, 187002 (2002).

[26] A E Koshelev and A A Golubov, Phys. Rev. Lett. **90**, 177002 (2003).

[27] N Nakai, M Ichioka, and K Machida, J. Phys. Soc. Jpn. **71**, 23 (2002).

[28] S. Mukhopadhyay, G. Sheet, P. Raychaudhuri, H. Takeya Phys. Rev. B **72**, 014545 (2005).

[29] P. Hohenberg and W. Kohn, Phys. Rev. **136**, B864 (1964).

[30] W. Kohn and L. J. Sham, Phys. Rev. **140**, A1133 (1965).

[31] J. P. Perdew, K. Burke, and M. Ernzerhof, Phys. Rev. Lett. **77**, 3865 (1996).

[32] R. Yu, and Q. Si, Phys. Rev. B **96**, 125110 (2017).

Chapter 4

# Nature of superconductivity in $PdTe_2$

In this chapter, we present the rigorous study of superconducting phase appearing in Dirac semimetal $PdTe_2$. The observations presented in this chapter are significant in understanding the non trivial band structure of this material. The results discussed in this chapter are already published in ref [1].

## 4.1 Introduction

Superconductivity in $PdTe_2$ has been known since 1978 [2–5] but did not receive much attention from the research community because of its very low superconducting transition temperature ($\sim$ 1.7 K). The recent discovery of type II Dirac fermions in the normal state of $PdTe_2$ [6–8] attracted a lot of attention and made this material interesting to explore the superconducting phase with the existence of topological character. More recently, scanning tunneling spectroscopy (STS) experiments displayed a conventional superconducting gap which follows BCS-like nature [9] in $PdTe_2$ [10]. Further experimental evidence including STM/STS measurements by another group, [11] specific heat measurements [12] and penetration depth measurements, [13, 14] confirmed the conventional phase of superconductivity. However, it was also seen that the upper critical field has a distribution on the surface of the cleaved $PdTe_2$ crystals and this distribution varied from 220 Gauss to 4 Tesla. In order to understand the origin of the distribution of $H_c$ in $PdTe_2$ further investigations are required.

In this chapter, we present a detailed study of the superconducting energy gap by STM/STS experiments at multiple points on the pristine surface of single crystals of $PdTe_2$ in the presence of the magnetic field. All the experimental results are shown in the next section.

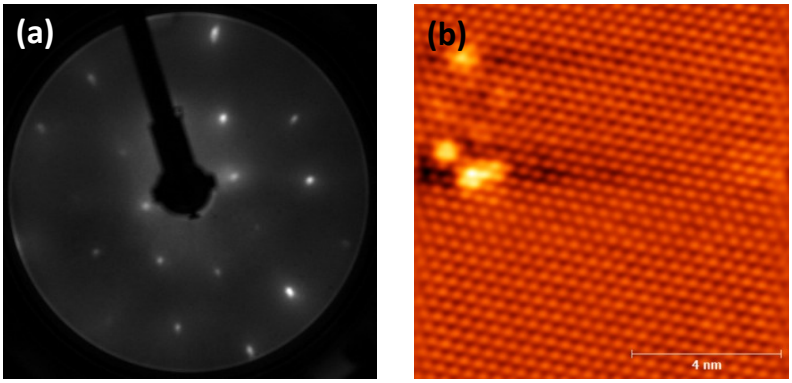


Figure 4.1: (a) shows LEED pattern of single crystalline $PdTe_2$ (b) The atomic resolution image of cleaved $PdTe_2$ crystal with surface defects shown as bright spots recorded at T = 385 mK.

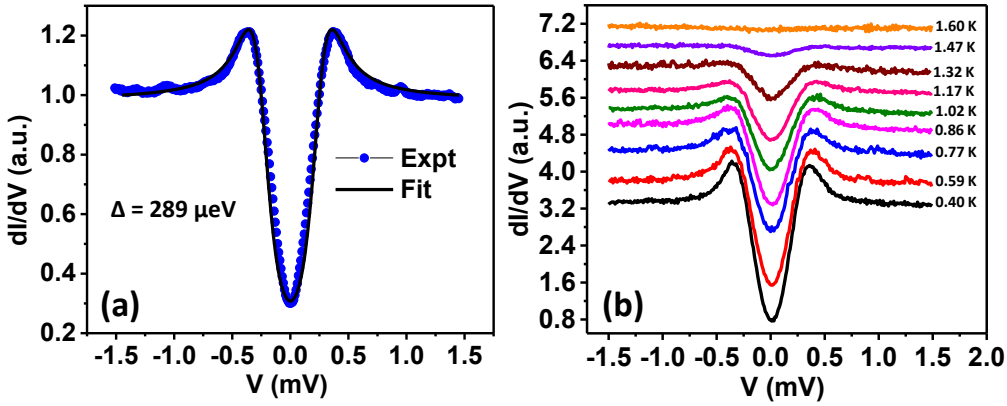


Figure 4.2: (a) A representative conductance spectrum with fit using Dyne's tunneling equation showing superconducting energy gap of 289 $\mu$eV. (b) Temperature dependence of the spectrum (as shown in (a)). The spectra at different temperatures in (b) have been vertically shifted for visual clarity.

## 4.2 Experimental details and results

On high-quality single crystals of $PdTe_2$ all experiments were performed in an UHV-STM that works down to the temperature of T = 300 mK . The crystals were cleaved at 77 K using the $in-situ$ cleaver. The quality of the pristine surface of $PdTe_2$ is confirmed by the LEED measurements (see figure 4.1 (a)) and quantum oscillation measurements performed in PPMS (Physical Properties Measurement System). [10] The unit cell of $PdTe_2$ is hexagonal same as in $CdI_2$ (space group $P\bar{3}m1$). [15] The atomically resolved image captured at 385 mK is shown in figure 4.1 (b) which shows the hexagonal topographic structure of $PdTe_2$. The bright spots are the defects on the surface of the crystal.

Figure 4.2 (a) demonstrates a tunneling conductance spectrum measured at 380 mK show-

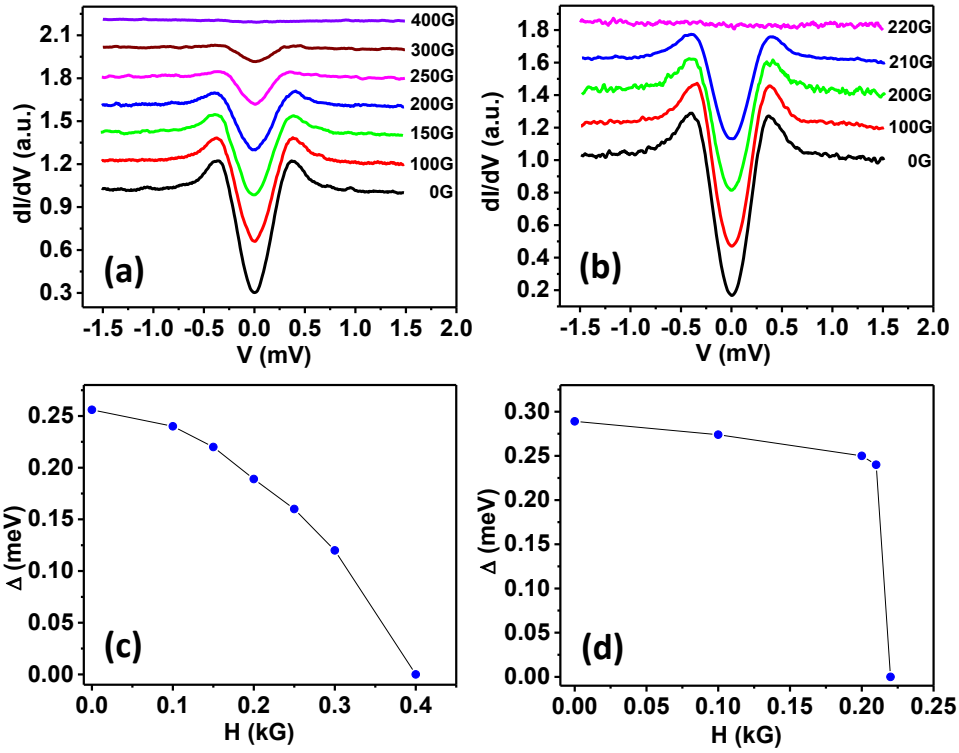


Figure 4.3: Magnetic field dependence of a spectrum (a) showing type II behaviour with $H_c$ = 400 G, and (b) showing type I behaviour with $H_c$ = 220 G. The spectra at different magnetic fields in (a, b) panels have been shifted vertically for visual clarity. (c), (d) Δ - H plots extracted from (a), (b) respectively.

ing two symmetric coherence peaks that occur at the superconducting energy gap. The typical value of the superconducting gap has been found to be $\Delta = 289\ eV$. We have used the same tunneling conductance formula that has been used in the previous chapter to fit the experimental data. [16] The temperature dependence of the spectrum is shown in figure 4.2 (b). The spectrum evolves smoothly with increasing temperature and disappears at the superconducting transition temperature of $PdTe_2$.

### 4.2.1 Investigation of superconducting phase in magnetic fields

Here, we focus on the behavior of the superconducting gap Δ in the presence of applied magnetic fields. A representative spectrum and its magnetic field dependence is shown in figure 4.3 (a) showing the critical field of 400 G. In the panel (b) another spectrum shows the critical field of 220 G. It can be seen that the spectra in panel (a) evolves smoothly while in panel (b) gap closes abruptly. Extracted Δ from (a) and (b) are plotted in panel (c) and (d) respectively. Both the spectra are acquired at different spatial local points on the surface of the sample. The smooth variation in figure (c) reflects the type II-like behavior of Δ, on the other hand, the sudden disappearance of Δ deliberates the type I like behavior of superconductivity. Statistical

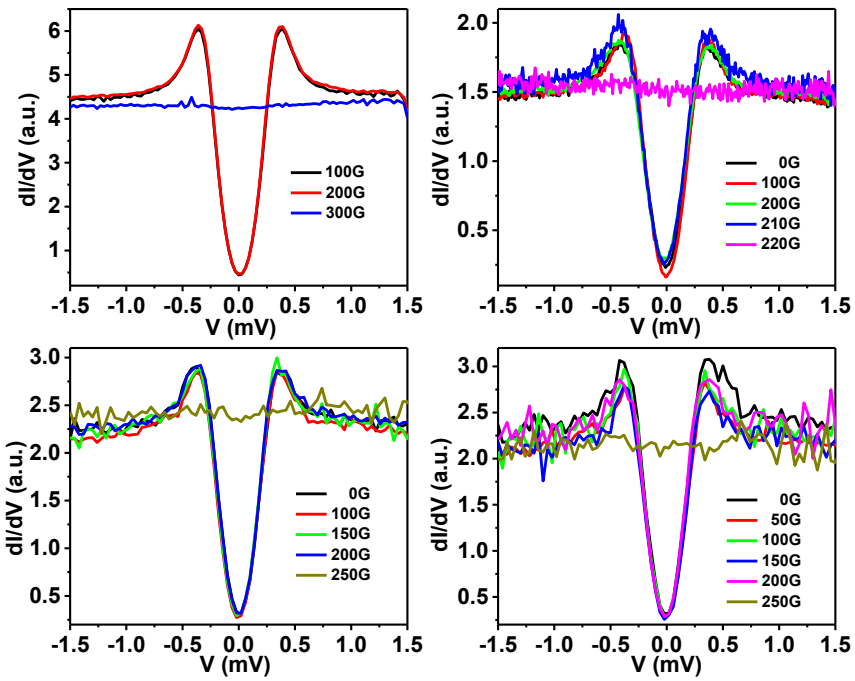


Figure 4.4: Four representative spectra showing low critical magnetic fields. These spectra also show a distribution of critical magnetic fields ranging between 220-300G.

observation of sudden disappearance of Δ at a large number of points shows the critical magnetic field in the range of 200 G to 300G. For all the spectra of critical magnetic field larger than 300 G shows type II behavior. Figure 4.4 shows four representative spectra where sudden disappearance is observed.

### 4.2.2 Conductance mapping above the critical temperature

It should be noted that such first order like transition of superconductivity is previously observed in point-contact experiments on some elemental superconductors. [17] Therefore, our observation of the mixed type of superconductivity and critical field inhomogeneity demands investigation in much more details. In order to understand the origin of such inhomogeneities in $PdTe_2$, we have investigated the normal state by the local density of states (LDOS) mapping above the critical temperature ($T > T_c$). In figure 4.5 (a), we show a large area topograph captured at 3.5 K, where a large number of defects can be seen. In figure 4.5 (b) $dI/dV$ vs $V$ spectra are shown and corresponding map sliced at 1.5 eV is shown in figure 4.5 (c). A visual inspection of the topograph (a) and corresponding LDOS map in (c) reveals that there is an additional contrast emerging in the background which is not due to the presence of defects. Such a background may originate from the intrinsic electronic inhomogeneity. To resolve clearly the contribution of the background signal alone, We have used Fourier filtering of the conductance maps. The maps of the extracted signals (figure 4.5 (d) and figure 4.5 (f)) clearly

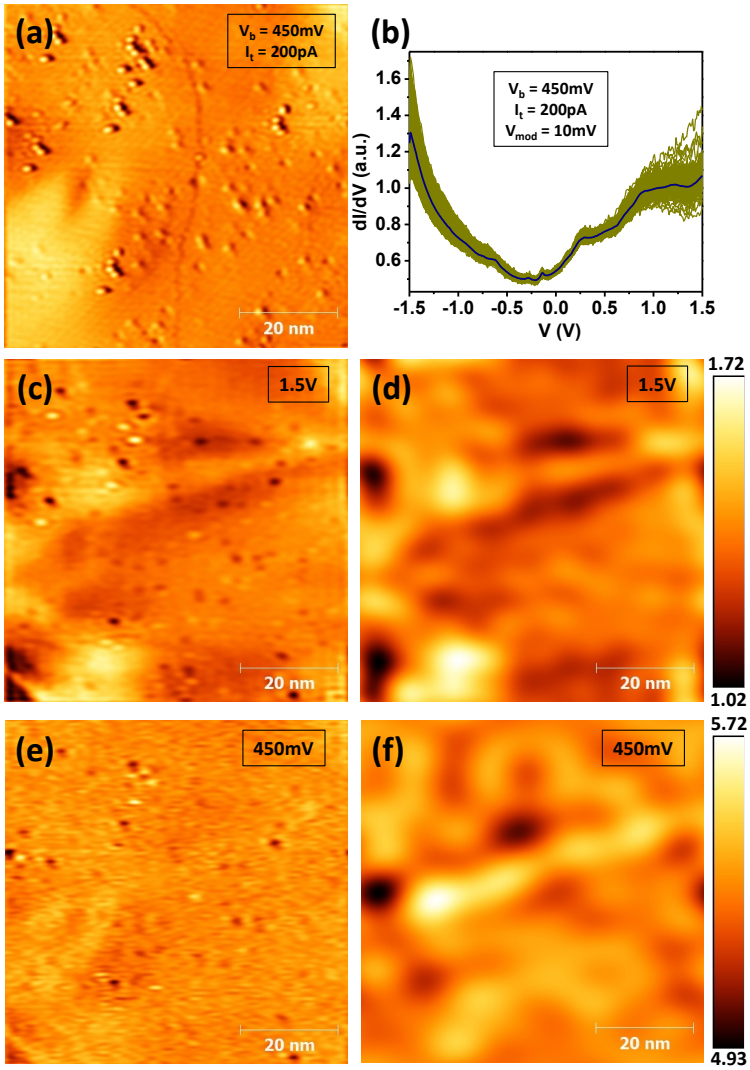


Figure 4.5: (a) Large area topograph of cleaved surface of $PdTe_2$ crystal captured at 3.5 K ($I$ = 200 pA) mode (70nm x 70nm). (b) Some representative conductance spectra over the same area as shown in panel (a). (c) and (e) shows conductance maps at 1.5V and 450mV respectively measured on the same area as shown in (a). (d) and (f) shows the variation of the Fourier filtered local density of states representing the intrinsic electronic inhomogeneities in $PdTe_2$.

show inhomogeneities of the local density of states at surface. As shown in the figure 4.5, a visual inspection of the conductance maps at different energies (1.5 eV in figure 4.5 (d) and 450 meV in figure 4.5 (f)) reveal that the inhomogeneity of the local density of states in the background also changes with energy. This electronic inhomogeneity might be originated because of puddles of electrons and holes rich areas. Earlier Such inhomogeneity was observed in certain 2-Dimensional systems [18, 19] and in topological insulators [20, 21] where Dirac point lies close to the chemical potential.

### 4.2.3 Conductance mapping in presence of magnetic field

A sudden disappearance of gap $\Delta$ may also occur if there is a vortex formation underneath the tip in presence of a magnetic field. In order to rule out this possibility we have measured the conductance maps in presence of magnetic field of more than 300 G which can derive the type I region in to the normal state. For this purpose, we applied magnetic field of 400 G and captured conductance map of 30 nm $\times$ 30 nm area. The conductance map with the spectral features have been shown in figure 4.6 (a) and (b) respectively. It can be seen in the figure 4.6 (b) that we have obtained three different spectral features depending on the position of the tip. (1) One type of spectra demonstrate no spectral features, these are corresponding to those points where superconductivity is destroyed due to type I nature. Such points are corresponding to the dark regions in the image of panel (a). (2) Second type of spectra show conductance dips at zero bias with two coherence peaks, these spectra are coming from the region where the type II superconductivity is still survive, but vortices have not formed at this field. Those regions are corresponding to the brightest spots in the conductance image (due to the presence of coherence peak). (3) Third type of spectra show shallow high-bias dips and a pronounced central peak. These along with those shown in (1) appear as relatively darker regions in the figure 4.6 (a). The variation in the normal state (high-bias) conductance is coming due to the variation of the local density of states in the distinct regions. The spectra of type (1) and (3) do not appear at zero field. Hence, it is clear that the regions where the superconductivity is suddenly destroyed (type-I regions) by applying the magnetic field, are different from the regions where clear vortex-like spectra are obtained.

In this context, we find that the surface of $PdTe_2$ is intrinsically inhomogeneous to the extent that it inherits puddles of both type-I and type-II superconducting regions, whereas the type-I behavior dominates in the bulk properties (as the bulk critical field is comparable to 300 G). More interestingly, in both regions, the superconducting gap amplitude ($\Delta(0)$) remain characteristically similar (0.25 - 0.28 meV).

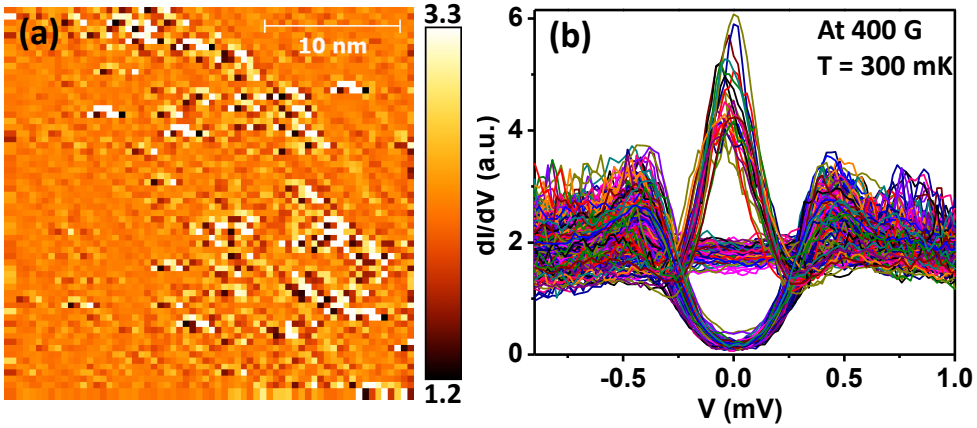


Figure 4.6: (a) Conductance map measured at 310 mK with a tip-bias of -400 $\mu$V in the presence of a magnetic field of 400 G. (b) Some of the representative $dI/dV$ vs. $V$ spectra corresponding to the different points (pixels) in (a).

### 4.2.4 Theoretical results

In order to understand such inhomogeneous nature of superconductivity in greater detail theoretically, we have studied the Ginzburgh-Landau (GL) theory. The Ginzburgh-Landau (GL) theory extended by Abrikosov and Gorkov (AG) includes the effects of the finite coherence length $\xi$ of a superconductor [22, 23]. More advanced treatment to the coherence length includes the effects of finite mean-free path ($l$) of the normal electrons given as $1/\xi = 1/\xi_0 + 1/l$, where $\xi_0$ is the intrinsic coherence length at zero temperature within the description of BCS theory [24].

As per the experimental results, the mean free path of the electrons may be inhomogeneous in the normal state of $PdTe_2$ which influence the superconducting state resulting in the inhomogeneous modulation of the GLAG parameter $\kappa$. From the GLAG theory, the relation between the mean free path $l$ and the GL parameter $\kappa$ can be given as [26]

$$\kappa(l) = \kappa(\infty)\frac{7\zeta(3)}{8S_{21}}, \tag{4.1}$$

where

$$S_{21} = \sum_{n=0}^{\infty} \frac{1}{2n+1}\frac{1}{2n+1+0.88\frac{\xi(0)}{l}}, \tag{4.2}$$

$\kappa(\infty)$ is its value for pure case where $l \to \infty$; $\kappa(\infty) = 0.96\frac{\lambda_L(0)}{\xi(0)}$. Quantum oscillation measurements estimated the Fermi velocity $v_F \sim 5.6 \times 10^5$m/s. Using the experimental estimates [13, 25] of $\xi(0) \sim 1.8\mu$m, we evaluate $\kappa$ as a function of $l$, and these results are shown in figure 4.7 for different values of $\kappa(\infty)$.

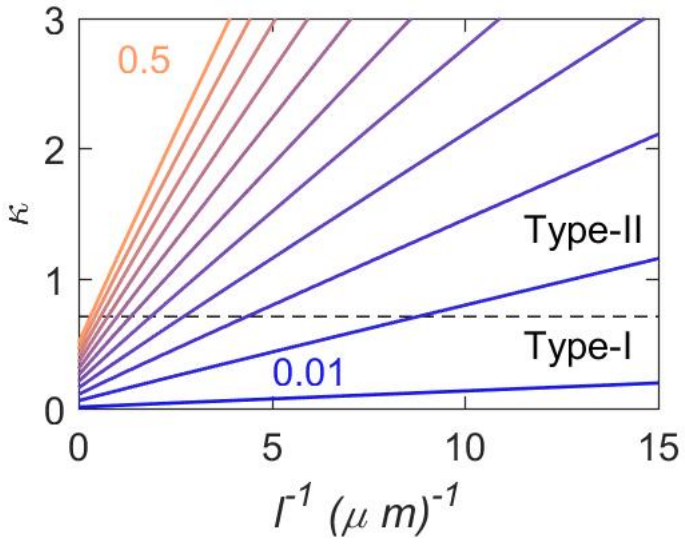


Figure 4.7: The GLAG parameter plot with respect to inverse mean-free path $l^{-1}$ for various computed values of the $\kappa(\infty)$ [13]. The horizontal dashed black line represent the critical value of $\kappa_c = 1/\sqrt{2}$, which separates between the type-I and type-II superconducting regions.

From the figure 4.7 it is clear that the GLAG parameter $\kappa$ increases almost linearly with $1/l$. We indeed find each relatives, in this range of experimental values, one starts with $\kappa(\infty) \sim 0.2 - 0.4$ in the type-I region and turns into type-II superconductor with decreasing $l$. We also determine the critical mean-free path (corresponding to $\kappa_c = 1/\sqrt{2}$ line) of 1500 nm, which is higher than average value of $l = 531nm$ obtained in bulk experimental measurements [13]. These results clearly indicate that $PdTe_2$ resides near the critical point between its type-I and type-II phases. Therefore, the regions with comparatively shorter mean-free path $l < l_c$ exhibit type-II superconductivity, while domains with larger mean-free path $l$ show type I nature of superconductivity in $PdTe_2$. This analysis also indicates that the normal state of $PdTe_2$ should also be electronically inhomogeneous.

## 4.3 Summary

In summary, we have found

- the direct observation of mixed type I and type II superconducting phase.
- the surface of the $PdTe_2$ crystals host electronic inhomogeneity in the normal state.
- the distribution of superconducting properties such as critical magnetic field, superconducting gap $\Delta$ and coherence length $\xi$.
- the spectral features of vortex but not the individual vortices

The STM studies presented here shows a distribution of critical fields on the surface of $PdTe_2$ which varies in a range starting from 200 G to 4 Tesla. The points where the critical field is low (200 G to 400 G) actually show type I like of behavior, on the other hand, the point where the critical field is larger (> 400 G) show type II-like behavior. We also observe an indication of electronically inhomogeneous surface above the critical temperature of $PdTe_2$.

In conclusion, we have shown that the surface of the single crystals of $PdTe_2$ host electronic inhomogeneities in the normal state. It might be possible that when the system undergoes superconducting transition, the inhomogeneous density of states give rise to a spatially varying superfluid density leading to variation of the coherence length $\xi$. The variation of the superfluid density on the surface is confirmed by the observation of a distribution of the superconducting energy gap ($\Delta$). Since the (upper) critical field is directly related to $\xi$, the distribution also causes a spatial distribution of the critical magnetic fields. Thereby, giving rise to the mixed nature of superconductivity.

## 4.4 Acknowledgements

In this chapter, theoretical calculations are performed by Priyo Adhikary and Dr. Tanmoy Das from IISC Bangalore. Single crystals are provided by Amit and Dr. Yogesh Singh from IISER Mohali.

# Bibliography


[1] A. Sirohi, S. Das, R. R. Chowdhury, Amit, Y. Singh, S. Gayen, and G. Sheet, J. Phys. Condens. Matter **31**, 085701 (2019).

[2] J. Guggenheim, F. Hulliger, and J. Müller, Helv. Phys. Acta **34**, 408 (1961).

[3] A. Kjekshus and W. B. Pearson, Can. J. Phys. **43**, 438 (1965).

[4] C. Raub, V. Compton, T. Geballe, B. Matthias, J. Maita and G. Hull, J. Phys. Chem. Solids **26**, 2051 (1965).

[5] B. W. Roberts, J. Phys. Chem Ref. Data **5**, 581 (1976).

[6] H. J. Noh, J. Jeong, and E. J. Cho, Phys. Rev. Lett. **119**, 016401 (2017).

[7] F. Fei, *et al.* Phys. Rev. B **96**, 041201(R) (2017).

[8] L. Yan, *et al.* Chin. Phys. Lett. **32**, 067303 (2015)

[9] J. Bardeen, L. N. Cooper, and J. R. Schrieffer, Phys. Rev. **108**, 1175 (1957).

[10] S. Das, Amit, A. Sirohi, L. Yadav, S. Gayen, Y. Singh, and G. Sheet, Phys. Rev. B **97**, 014523 (2018).

[11] O.J. Clark, *et al.*, Phys. Rev. Lett. **120**, 156401 (2018).

[12] Amit, And Y. Singh, Phys. Rev. B **97**, 054515 (2018).

[13] M.V. Salis, P. Rodière, H. Leng, Y. K. Huang, A. d. Visser, arXiv:1804.08969 (2018).

[14] S. Teknowijoyo, N. H. Jo, M. S. Scheurer, M. A. Tanatar, K. Cho, S. L. Bud'ko, P. P. Orth, P. C. Canfield and R. Prozorov, arXiv:1804.00723 (2018).

[15] L. Thomassen, Z. Phys. Chem. B **2**, 349 (1929).

[16] R. C. Dynes, V. Narayanamurti, and J. p. Garno, Phys. Rev. Lett. **41**, 1509 (1978).

[17] Y. G. Naidyuk, H. v. Löhneysen, and I. K. Yanson, Phys. Rev. B **54**, 16077 (1996).

[18] Y. Zhang, V. W. Brar, C. Girit, A. Zettl and M. F. Crommie, Nature Physics **5**, 722–726 (2009).

[19] S. Samaddar, I. Yudhistira, S. Adam, H. Courtois, and C.B. Winkelmann, Phys. Rev. Lett. **116**, 126804 (2016).

[20] N. Borgwardt, *et al.*, Phys. Rev. B **93**, 245149 (2016).

[21] T. Knispel, W. Jolie, N. Borgwardt, J. Lux, Zhiwei Wang, Yoichi Ando, A. Rosch, T. Michely, and M. Grüninger, Phys. Rev. B **96**, 195135 (2017).

[22] A. A. Abrikosov **32**, 1442 (1957); [5] Sov. Phys. JETP **5**, 1174 (1957)].

[23] L. P. Gor'kov, Zh. Eksperim. i Teor. Fiz. **34**, 735 (1958); *ibid.* **36**, 1918 (1959); [Sov. Phys. JETP **7**, 505 (1958)]; [Sov. Phys. JETP **9**, 1364 (1959)].

[24] M. Tinkham, Introduction to Superconductivity, (McGraw-Hill, New York, 1996).

[25] H. Leng, C. Paulsen, Y. K. Huang, and A. de Visser, Phys. Rev. B **96**, 220506(R) (2017).

[26] A. E. Jacobs, Phys. Rev. B **4**, 3022 (1971).

Chapter 5

# Unconventional superconductivity in $Nb_xBi_2Se_3$

In this chapter, the qualitative study of superconducting spectra reveals the presence of low-energy excitations at sufficiently low temperatures in an intercalated topological insulator. The results discussed in this chapter are already published in ref [1].

## 5.1 Introduction

In reality, it is known that the intercalation of elemental metals between the interleaved planes of a topological insulator $Bi_2Se_3$ [2, 3] leads to the superconducting phase in the resulting system. Intercalation of elemental metals like Cu and Sr intercalated in $Bi_2Se_3$ reveals the superconducting phase below 3 K [4–7]. Naturally, the appearance of topological superconductivity was suggested and explored in these systems. However, In cases of $Cu_x$-$Bi_2Se_3$ and $Sr_x$-$Bi_2Se_3$ the scanning tunneling spectroscopy experiments revealed no signature of mid gap states at low temperatures and the realization of topological superconductivity in those systems is still in doubt [5, 8, 9]. Theoretical and experimental results on these compounds have also been conflicting [10–13]. Recently, the third candidate of this family $Nb_x$-$Bi_2Se_3$ ($x$ = 0.25) was recognized as a superconductor with critical temperature of 3.5 K. Based on number of experiments, it has been realized that $Nb_x$-$Bi_2Se_3$ preserved the topological non-trivial properties even below its superconducting transition temperature [14].

Here, we present our observations of emergence of unconventional superconducting state in $Nb_x$-$Bi_2Se_3$ through STM/STS experiments. We show that the spectra deviate from a BCS-like prediction and the tunneling conductance at low-bias is quite large. Our observations of finite conductance at zero bias are consistent with the idea of nodal order parameter in $Nb_x$-$Bi_2Se_3$. Proceeding to the next section We show our experimental results [1].

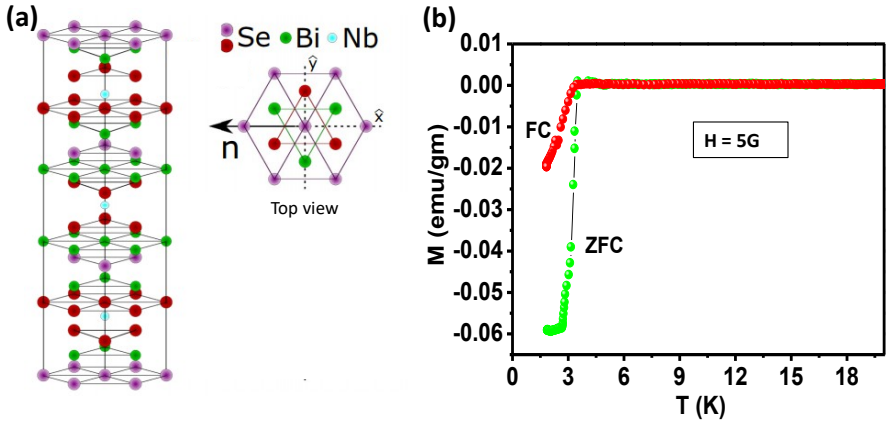


Figure 5.1: (a) Crystal structure of $Nb_xBi_2Se_3$ adopted from the ref [15]. (b) M vs. T plot ZFC (Green curve) and FC (Red curve) showing superconducting transition at 3.5 K. ZFC and FC data are corresponding to zero field cooled and field cooled data.

## 5.2 Experimental details and results

### 5.2.1 Sample details

High quality single crystals of $Nb_x$-$Bi_2Se_3$ used for the measurements were grown by a modified Bridgman technique. The crystals were characterized by structural and magnetic measurements and as shown in the magnetization vs. temperature data in Figure 5.1 (b), a superconducting transition at 3.5 K was observed. In figure 5.1 (a) we have shown the crystal structure of $Nb_x$-$Bi_2Se_3$ adopted from the ref [15]. The crystal structure shows that the Nb atoms are intercalated between the quintuple layers of Bi and Se. $Nb_x$-$Bi_2Se_3$ crystallizes into the same crystal structure as of $Bi_2Se_3$. Due to the additional Nb ions between the adjacent $Bi_2Se_3$ quintuple layers the c-axis is slightly extended.

### 5.2.2 STM/STS results

All the experiments were performed in an ultra-high-vacuum (UHV) Scanning Tunneling Microscope (STM) which works down to 300 mK on single crystals of $Nb_x$-$Bi_2Se_3$. The crystals were cleaved at 77 K in UHV ($10^{-11}$mbar) using the $in-situ$ cleaver. After cleaving, the crystal was immediately transferred into the scanning stage at low-temperature. This process minimized the possibility of contamination of the pristine surface.

In figure 5.2 we show topography of $Nb_x$-$Bi_2Se_3$. We show an atomically resolved image of an area of 10 nm x 10nm in figure 5.2 (a). In the image (figure 5.2 (b)) we observe disc-shaped bright objects with a flat background. These bright objects are the defect states due to Nb atoms/clusters [14]. These clusters are randomly distributed over the surface with a different concentration in different regions of the crystal. In Figure 5.2 (c) we show a different

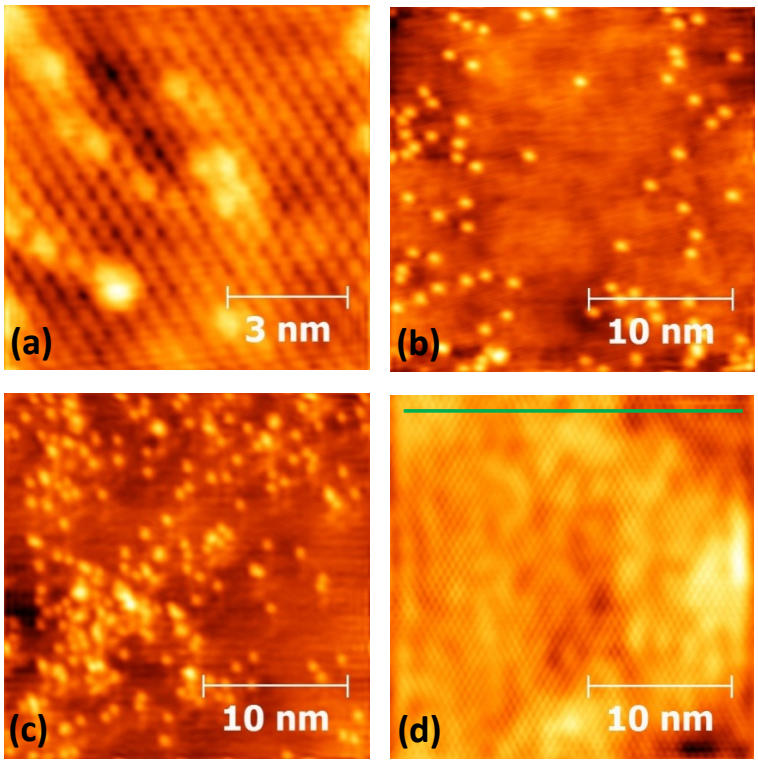


Figure 5.2: (a) STM Topographic image of an area (10 nm x 10 nm) with atomically resolved background and Nb clusters captured at 2 K ($V_b$ = 10 mV, $I_t$ = 1.2 pA). Topographic images of 25 nm x 25 nm area showing Nb clusters with (b) lower density and (c) higher density captured at 18 K ($V_b$ = 1 V, $I_t$ = 110 pA). (d) Topographic image of a cluster-free region showing atoms with an underlying bright/dark contrast captured at 400 m K ($V_b$ = 10 mV, $I_t$ = 5 pA).

area where we observe the considerably large density of the Nb clusters. We also found large areas where the Nb clusters are not resolved. Such an image we show in figure 5.2 (d) of a 25 nm x 25 nm area, where the disc-shaped clusters are not seen. Under this condition, the atoms on the surface of the crystal become clearly visible. This atomically resolved image reveals alternate bright and dark regions in the background. A comparison with the image shown in panel (a) reveals that this contrast in the background displays no correlation with the position of the clusters. Therefore, this contrast might originate from an intrinsic property of the crystal. A qualitative comparison of these features with that obtained on the compensated topological insulator $BiSbTeSe_2$, [16] suggests that this contrast might originate due to puddles of electron rich and hole rich areas on the surface.

STS spectra measured at 4 K at different points on the surface reveal a “Dirac cone" like feature with the possible Dirac point at $\sim$ 130 meV below the Fermi energy. One of such spectrum is shown in figure 5.3. Existence of the Dirac point so close to the Fermi energy indicates that the Dirac dispersion character may extend beyond the Fermi energy thereby supporting the idea of charge puddles. It also indicates that the Dirac surface states may participate in supercon-

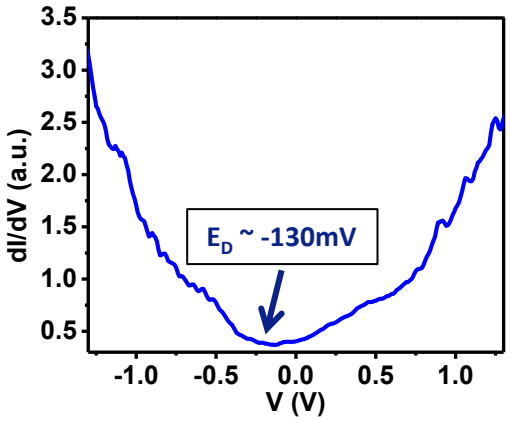


Figure 5.3: Tunneling spectrum recorded at 4 K in $Nb_x$-$Bi_2Se_3$.

ducting pairing below 3.5 K, accomplishing the requirement of topological superconductivity here.

### 5.2.3 Tunneling Spectroscopy results

The tunneling spectroscopy on the surface of $Nb_x$-$Bi_2Se_3$ below the T$c$ shown in figure 5.4. In Figure 5.4 (a) we show a typical STS spectrum measured at 400 mK. Two coherence peaks followed by a low-bias conductance dip indicates the formation of a superconducting gap in the spectrum. However, unlike a typical spectrum with a fully formed BCS gap, [17] in this case, the low-bias quasiparticle density of states are large between the coherence peaks. We reproducibly observed such spectral features without a fully formed gap at large number of points on the surface. It should be noted that in cases of $Cu_xBi_2Se_3$ [8] and $Sr_xBi_2Se_3$, [9] a fully formed superconducting gap with $dI/dV = 0$ at zero bias was seen. To confirm this, we obtained a large number of spectra at different points along the green line shown in figure 5.2 (d) and plotted in figure 5.4 (b). Along this line that cuts through dark, bright and very bright regions, as it is clear from the image (figure 5.2 (d)), the coherence peaks appeared at the same energy. It indicates the insensitivity of the superconducting phase to the intrinsic modulation of the local density of states.

Furthermore, to confirm such unusual robustness of the superconductivity, we selected an area (figure 5.4 (c)) where the Nb clusters and the dark-bright contrast with an atomically resolved background are clearly resolved. At 2 K, very close to the $T_c$, we performed local tunneling spectroscopy at some special points (points 1, 2 and 3, for example). In Figure 5.4 (d) we show the spectra obtained at points 1, 2 and 3 which did not reveal any qualitative difference. It is also interesting to note that at all these points, the spectral features related to superconductivity at a temperature close to $T_c$ not only exist but also show striking similarities with each other. This indicates that the superconducting features as well as $T_c$ are uniform all

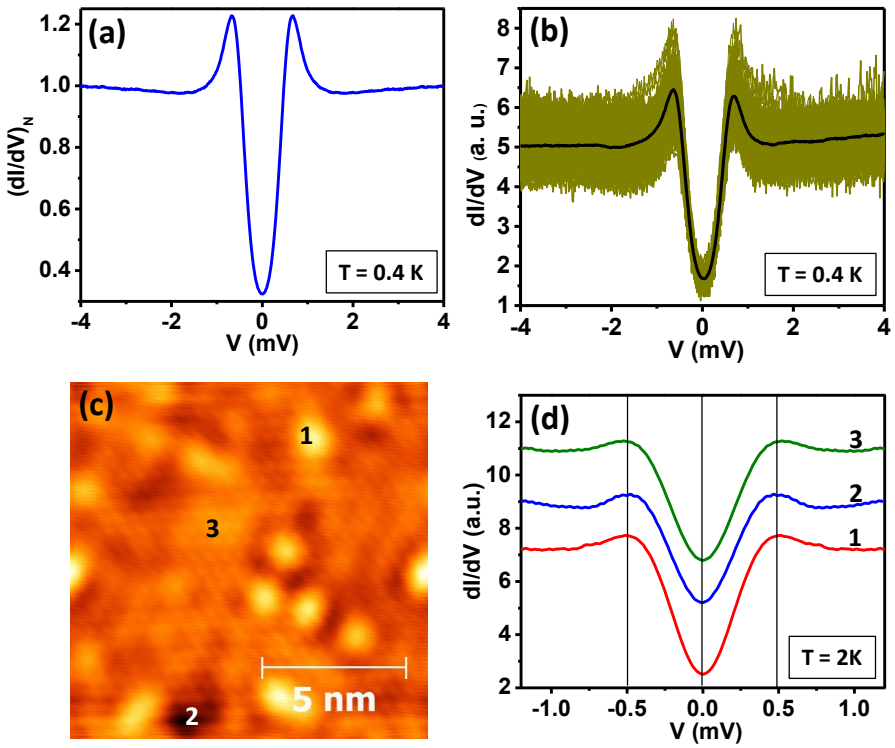


Figure 5.4: (a) A representative tunneling spectrum recorded at 400 mK temperature showing two coherence peaks corresponding to superconducting energy gap. (b) The spectra at multiple points along the green line shown in figure 5.3 (d) recorded at 400 mK. The black line is the average of all the spectra. (c) Topographic image of a 12 nm x 12 nm area showing atoms, background dark/bright contrast and Nb clusters (bright circular spots). (d) Tunneling spectra recorded at 2 K at three points "1", "2", "3" as shown in the panel (c).

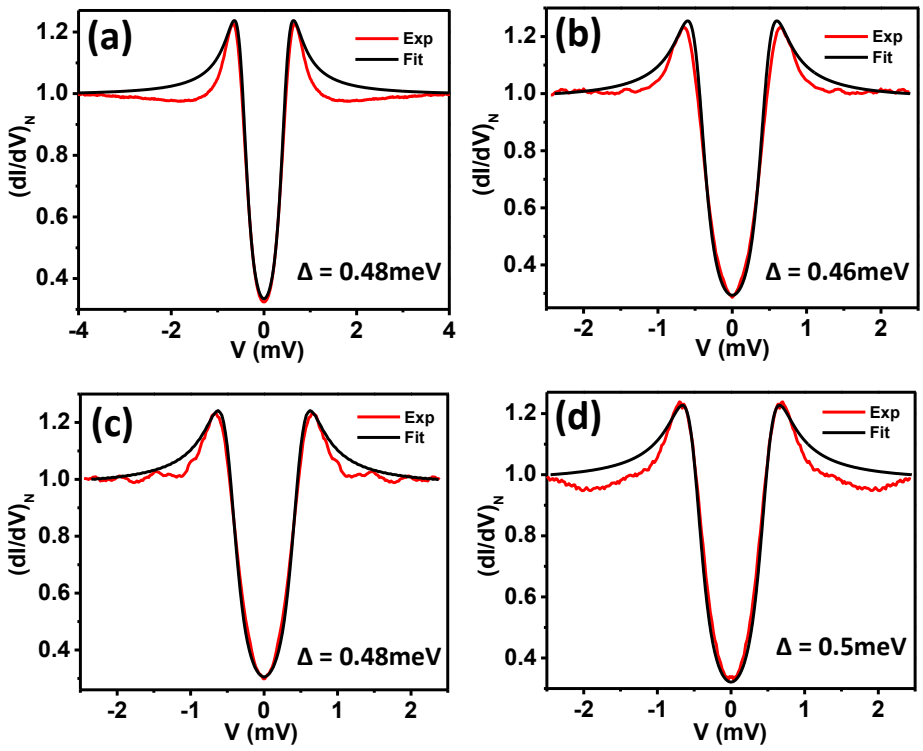


Figure 5.5: (a, b, c, d) Four representative spectra measured at 400 mK with fittings using Dyne's formula (an extended BCS theory).

over the crystal surface, despite the presence of the dark/bright contrast. Within the regions that we have explored on the surface of the crystals we did not observed any significant difference.

In Figure 5.5 (a, b, c, d) we show four representative tunneling spectra (red lines) with best possible theoretical fits (black lines) using Dyne's formalism [18]. The experimental spectral features show a shallow dip just above the coherence peak. Therefore, it is clear from the data shown in figure 5.5, that except the large density of states at low-energy, the experimental data deviate from the theoretical fits more dramatically just above the coherence peaks. These features are too common and reproducible in this system which cannot be ignored as a moderate deviation from the theoretical fit.

### 5.2.4 Temperature and magnetic field dependence

In figure 5.6, we show the evolution of spectral features with increasing temperature and magnetic fields. The spectrum obtained at 400 m K evolves smoothly with increasing magnetic field and all spectral features disappear at critical field of 3 Tesla as shown in figure 5.6 (b). In order to further investigate the nature of superconductivity, we performed temperature dependence of the spectral features. The spectral features decrease gradually with increasing temperature and disappear around 3 K slightly below the global $T_c$. We have plotted $\Delta$ extracted from the

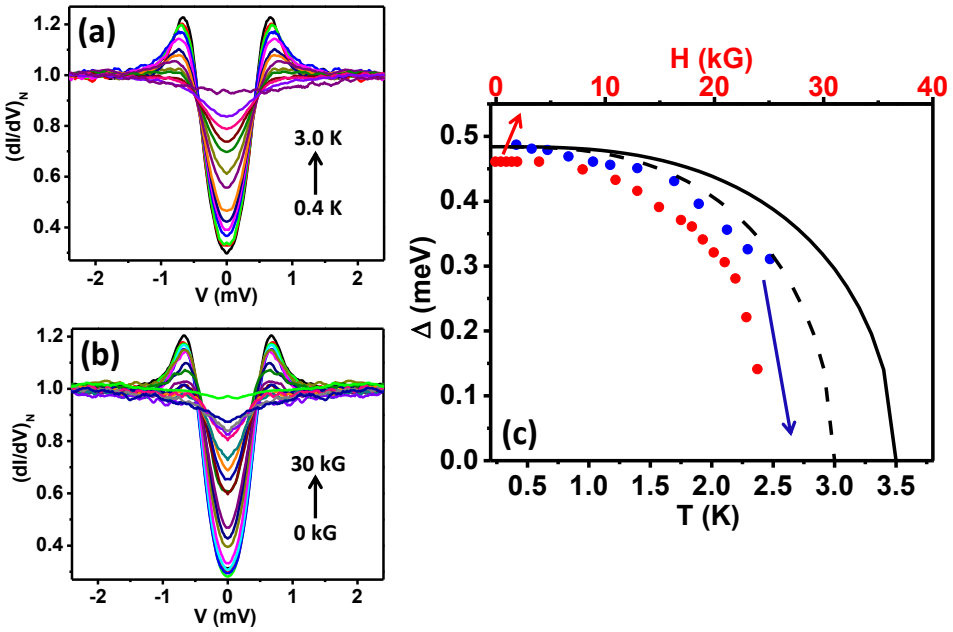


Figure 5.6: (a, b) Temperature and magnetic field dependence of a typical spectrum respectively. (c) Extracted Δ from panel (a) and (b) are plotted with respect to temperature (blue) and magnetic filed (red). The solid black line is corresponding to the BCS predictions of the temperature dependence of Δ for $T_c$ =3.5 K and the dotted line is for $T_c$ = 3 K.

best possible fitting for the spectra at different temperatures (figure 5.6 (c)). In the same panel we have also shown the expected behavior within BCS theory for $T_c$ = 3.5 K (black solid line) and for $T_c$ = 3 K (dotted line) [17]. The experimental data follows the BCS-like dependence at very low temperatures but deviates slightly from that at higher temperatures. It should be noted, since the experimental spectral features do not match with the conventional BCS theory that we have used to fit them, evaluation of the exact temperature dependence of the gap (Δ) is non-trivial.

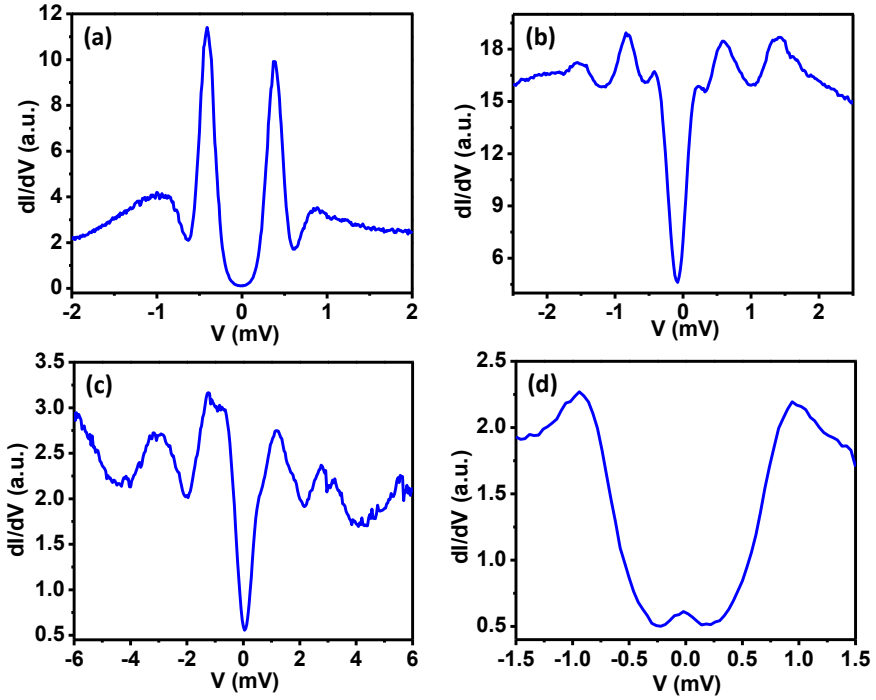


Figure 5.7: (a) A spectrum showing prominent dips above coherence peaks (as compare to the other spectra shown before). (b, c) Tunneling spectra showing multiple coherence peaks. (d) A spectrum showing a small zero-bias conductance peaks.

Majority of the conductance spectra obtained on $Nb_x$-$Bi_2Se_3$ showed deviation from the theoretical fits, other spectral features were also often obtained. We show such four spectra in figure 5.7 obtained at certain points on the surface. These spectra deviates more significantly from the theoretical fit. It should be noted that all the spectra presented in figure 5.5 deviate from the theoretical fits due to the formation of shallow dips just above the coherence peaks. Such features are predicted to appear in the tunneling spectrum between a normal metal and a superconductor where superconducting oder parameter is defined by chiral pairing [19, 20]. Hence, in this case as well, an $s + ip$ symmetry of the superconducting order parameter might be possible. An $s + ip$ symmetry of the superconducting order parameter is again consistent with earlier observations of nodal order parameter symmetry in $Nb_x$-$Bi_2Se_3$ [15].

## 5.3 Summary

The above discussed experimental results reveal that the superconducting phase realized in Nb intercalated $Bi_2Se_3$ below 3.5 K does not described well within the BCS theory for conventional superconductors. The pristine surface of the single crystal of $Nb_x$-$Bi_2Se_3$ shows charge puddles which is an indication of the existence of topological dispersion in the energy scale of superconductivity. In fact, the underlying compound unlike the other compounds of its family shows finite mid-gap states in the tunneling spectra. In addition, the spectral features show deviation from the theoretical fittings using Dyne's equation . Therefore, we attribute the above shown results of the appearance of low-energy excitations in the superconducting regime and the non-BCS nature of energy gap to the existence of unconventional/topological order of superconductivity in $Nb_x$-$Bi_2Se_3$.

## 5.4 Acknowledgements

Single crystals of the Samples are provided by Prakriti Neha, Karn S. Jat, and Prof. Satyabrata Patnaik from JNU Delhi.

# Bibliography


[1] A. Sirohi, S. Das, P. Neha, K. S. Jat, S. Patnaik and G. Sheet, Phys. Rev. B **98**, 094523 (2018).

[2] H. Zhang, C.-X. Liu, X.-L. Qi, X. Dai, Z. Fang and S.-C. Zhang, Nat. Phys. **5**, 438 (2009).

[3] Y. Xia, D. Qian, D. Hsieh, L. Wray, A. Pal, H. Lin, A. Bansil, D. Grauer, Y. S. Hor, R. J. Cava and M. Z. Hasan, Nature Physics **5**, 398 (2009).

[4] Y. S. Hor, A. J. Williams, J. G. Checkelsky, P. Roushan, J. Seo, Q. Xu, H. W. Zandbergen, A. Yazdani, N. P. Ong, and R. J. Cava, Phys. Rev. Lett. **104**, 057001 (2010).

[5] M. Kriener, K. Segawa, Z. Ren, S. Sasaki, and Y. Ando, Phys. Rev. Lett. **106**, 127004 (2011).

[6] Shruti, V. K. Maurya, P. Neha, P. Srivastava, and S. Patnaik, Phys. Rev. B **92**, 020506(R) (2015).

[7] C. Q. Han, et. al., App. Phys. Lett. **107**, 171602 (2015).

[8] N. Levy, T. Zhang, J. Ha, F. Sharifi, A. A. Talin, Y. Kuk, and J. A. Stroscio, Phys. Rev. Lett. **110**, 117001 (2013).

[9] G. Du, et. al., Nature Communications **8**, 14466 (2017).

[10] S. Sasaki, M. Kriener, K. Segawa, K. Yada, Y. Tanaka, M. Sato, and Y. Ando, Phys. Rev. Lett. **107**, 217001 (2011).

[11] X. Chen, C. Huan, Y. S. Hor, C. A. R. Sá de Melo and Z. Jiang, arXiv:1210.6054v1 (2012).

[12] T. H. Hsieh and L. Fu, Phys. Rev. Lett. **108**, 107005 (2012).

[13] T. Kirzhner, E. Lahoud, K. B. Chaska, Z. Salman, and A. Kanigel, Phys. Rev. B **86**, 064517 (2012).

[14] Y. Qiu, K. N. Sanders, J. Dai, J. E. Medvedeva, W. Wu, P. Ghaemi, T. Vojta, Y. S. Hor, arXiv:1512.03519v1 (2015).

[15] M. P. Smylie, H. Claus, U. Welp, W.-K. Kwok, Y. Qiu, Y. S. Hor, and A. Snezhko, Phys. Rev. B **94**, 180510(R) (2016).

[16] T. Knispel, W. Jolie, N. Borgwardt, J. Lux, Zhiwei Wang, Yoichi Ando, A. Rosch, T. Michely, and M. Grüninger, Phys. Rev. B **96**, 195135 (2017).

[17] J. Bardeen, L. N. Cooper, and J. R. Schrieffer, Phys. Rev. **108**, 1175 (1957).

[18] R. C. Dynes, V. Narayanamurti, and J. p. Garno, Phys. Rev. lett. **41**, 1509 (1978).

[19] T. Yokoyama, C. Iniotakis, Y. Tanaka, and M. Sigrist, Phys. Rev. Lett. **100**, 177002 (2008).

[20] Y. Asano, A. A. Golubov, Y. V. Fominov, and Y. Tanaka, Phys. Rev. Lett. **107**, 087001 (2011).

Chapter 6

# Tip-induced superconductivity in silicon

In this chapter, we present the emergence of an unexpected superconducting phase in silicon at mesoscopic length scales. The superconducting phase emerged under point-contacts of silicon and a metallic tip, such phase is known as Tip-induced superconducting (TISC) phase and has been previously reported in topologically non-trivial materials. The silicon crystals and metallic tip both are topologically trivial materials, therefore, the presented results are of significant interest. Some of the experimental results presented in this chapter are already published in ref [1].

## 6.1 Introduction

Silicon is the most inexpensive and extensively used material in the semiconductor industry. [2–8] The ability of inducing novel electronic properties in silicon made this a material of choice for technological purpose. [5, 7] Possibility of superconductivity in this material naturally attracts significant attention of scientific and technological community. In the past, theoretical investigations revealed the possibility of superconductivity in doped semiconductors like silicon [9–11] and germanium. [11] Some of the experimental observations showed superconductivity in certain phases of semiconductors depending on external applied forces and special conditions. [12, 13] It was found that the application of extremely large pressure drives the $\beta$-Sn and hexagonal (sh) metallic phases of silicon in to the superconducting phase. [14, 15] More recently, superconductivity was observed in thin layer of cubic silicon below 0.35 K only when it was doped heavily. Such superconducting phases of silicon were used to fabricate the nano-devices [8] functional only at low temperatures. However, observation of the superconducting phase in moderately-doped bulk silicon remained an unattained goal. Motivated by the recent discoveries of TISC superconducting phase in non-trivial materials [16–18] we have chosen semiconducting silicon for point-contact experiments and observed a superconducting phase which appears in moderately doped bulk silicon.

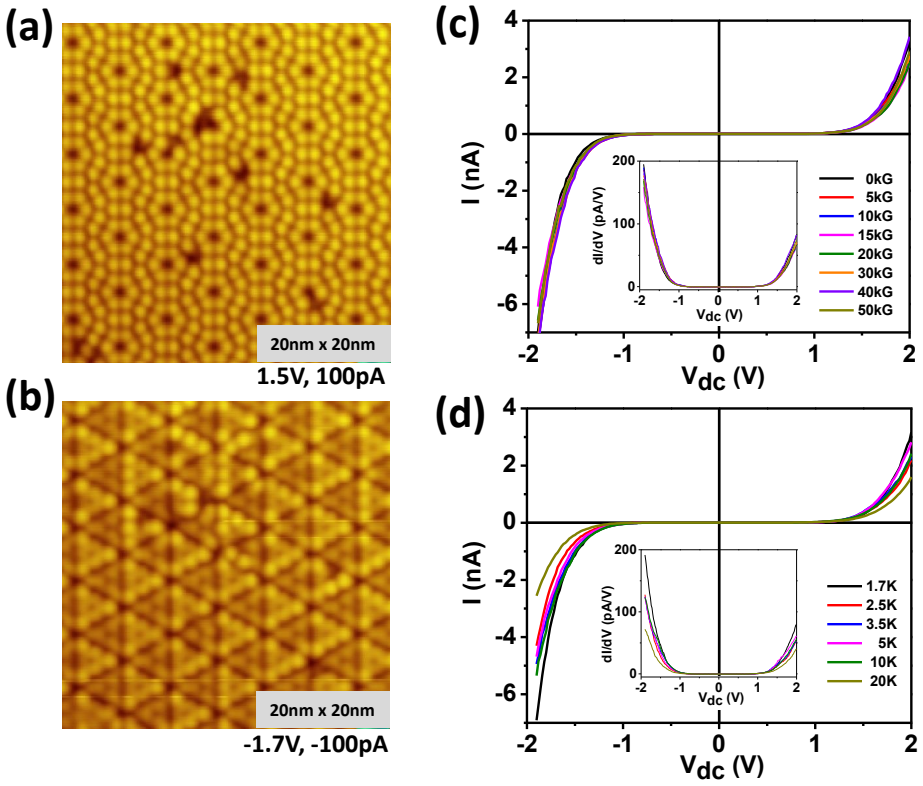


Figure 6.1: (a), (b) Atomic resolution images of silicon surface which shows 7x7 reconstruction of Arsenic-doped Silicon(111) captured at 1.6 K with positive and negative bias respectively. (c) Tunneling $I-V$ characteristics on the same and its magnetic field dependence. (d) Temperature dependence of $I-V$. $dI/dV$ vs. $V$ data are also shown in the insets of (c) and (d).

## 6.2 Experimental details and results

### 6.2.1 Sample details

We have used commercially available silicon crystals for the experiments. The type and level of doping were confirmed by in-house Hall measurements in a physical properties measurements system (PPMS) at low temperatures. The surface of the single crystals were investigated by STM and the semiconducting nature of all the crystals were further confirmed by scanning tunneling spectroscopy down to 1.6 K. In figure 6.1 (a, b) we show atomic resolution images of the 7x7 reconstruction of an As-doped silicon. We also show the $I-V$ and $dI/dV$ characteristics in the tunneling regime and their temperature (figure 6.1 (d)) and magnetic field (figure 6.1 (c)) dependence. From the data presented in figure 6.1, it is clear that the crystals are semiconducting in nature and no signature of superconductivity is observed in the bulk crystals.

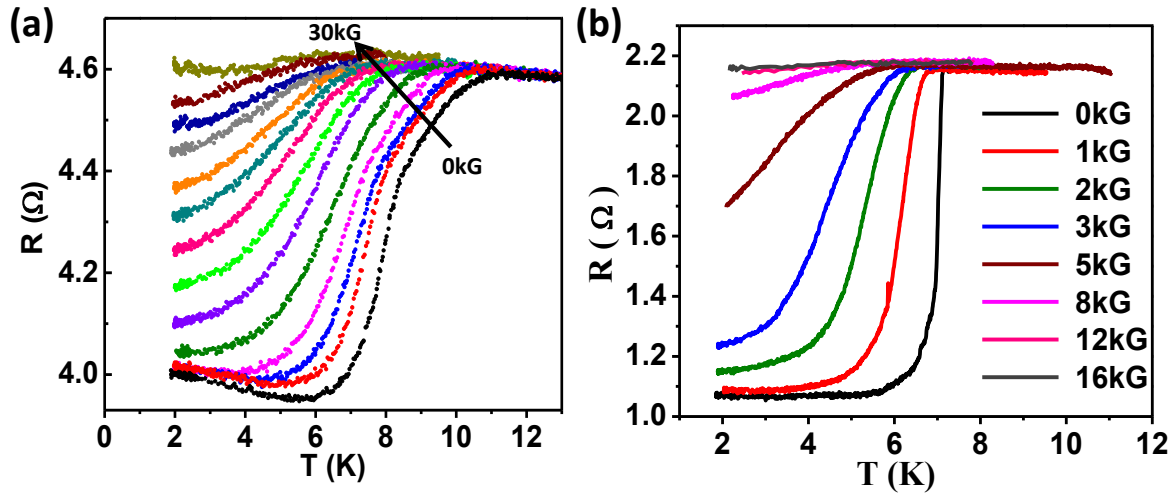


Figure 6.2: (a) Magnetic field dependence of $R-T$ showing the critical temperature of $\approx$ 11 K, the value of current sent to measure $R-T$ is 0.33 mA in silicon point-contact. (b) $R-T$ of Pb point-contact. $R-T$ data shows striking similarity with the data taken on silicon shown in panel (a).

### 6.2.2 Point-contact spectroscopy

The point contacts were made on silicon crystals using a sharp metallic tungsten (W) tip by the mechanism of an STM-like coarse approach at low temperature. When the point contact is away from the ballistic regime, contact resistance is given by the Wexler's formula [19] $R = \frac{2h/e^2}{(ak_F)^2} + \frac{\rho(T)}{2a}$ as discussed in chapter 2. As shown in figure 6.2 (a), a resistive transition is observed in $R$ *vs.* $T$ data which shows striking similarity with the data that is observed on superconducting Pb under point-contacts (see figure 6.2 (b)). The $R$ *vs.* $T$ data for silicon point-contact evolves systematically with the increasing magnetic field as expected for a superconducting transition. It must be noted that the resistance in the superconducting state does not go to zero value for point-contacts, the emerging superconducting phase needs to be confirmed by transport spectroscopic measurements. [1, 16–18]

Spectroscopic results are shown in Figure 6.3. Here, we have shown representative point contact spectra obtained from different regimes of mesoscopic transport on As-doped Si(111). In the $dI/dV$ vs. $V$ spectra shown in Figure 6.3 (a), a double-peak structure appear in $dI/dV$ that is known to originate from a ballistic superconducting point contact. Such a symmetric double-peak features are known to be trademark signatures of Andreev reflection [20] in superconducting point contacts. In the past, such structures were seen in ballistic limit [21] data obtained on the Weyl semimetal TaAs [17] and the 3-D Dirac semimetal $Cd_3As_2$. [16] Where these features were attributed to the phenomenon of tip-induced superconductivity. However, the observation of a double-peak structure in $dI/dV$ alone does not confirm the observation of TISC. In order to further confirm the TISC phase, we show a spectrum measured in inter-

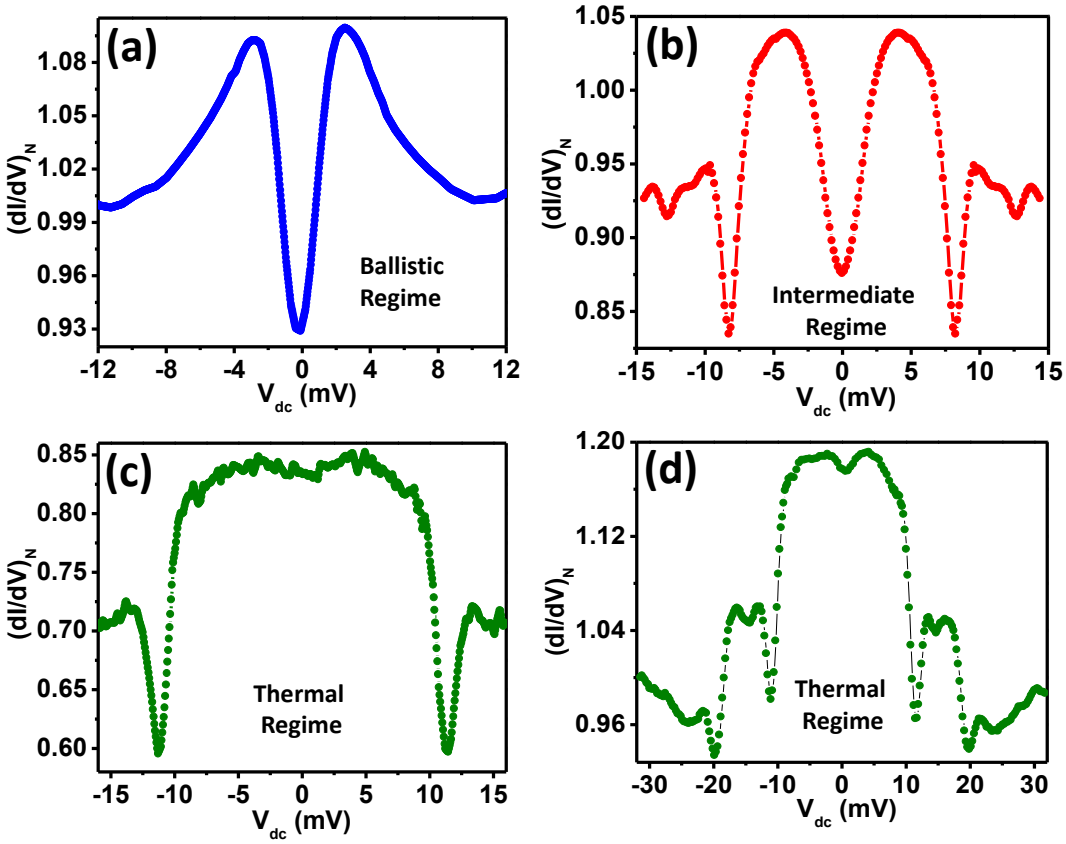


Figure 6.3: Point contact spectra close to the (a) ballistic regime (b) intermediate regime and (c) thermal regime on As-doped Si(111) using W tip. (e) A spectrum showing multiple critical current peaks recorded in thermal regime. All the spectra were measured at 1.5 K.

mediate regime of transport where distinct conductance dips along with a suppressed Andreev reflection dominated double-peak structure are observed and in figure 6.3 (c) we show a spectrum which displays only conductance dips, such a dip structure is attributed to the critical current dominated dips in superconducting point-contacts. [22] By slightly changing the point contact of thermal regime, it was also possible to observe multiple conductance dips (figure 2(d)). Multiple conductance dips are expected for superconducting point contacts which comprise of multiple micro-constrictions, where each micro-constriction showing unique critical current dips originating from its unique geometry.

To note that the conductance spectra recorded in different regimes of mesoscopic point-contacts on superconducting Pb also shows striking similarities with the data observed on silicon (see figure 6.4 (a, b, c)). [23]

Therefore, the spectroscopic data shown above confirm the appearance of a tip-induced superconducting (TISC) phase in silicon. The maximum recorded $T_c$ was $\sim$ 11 K, which is remarkably high. These observations of TISC phase are further supported by magneto-transport

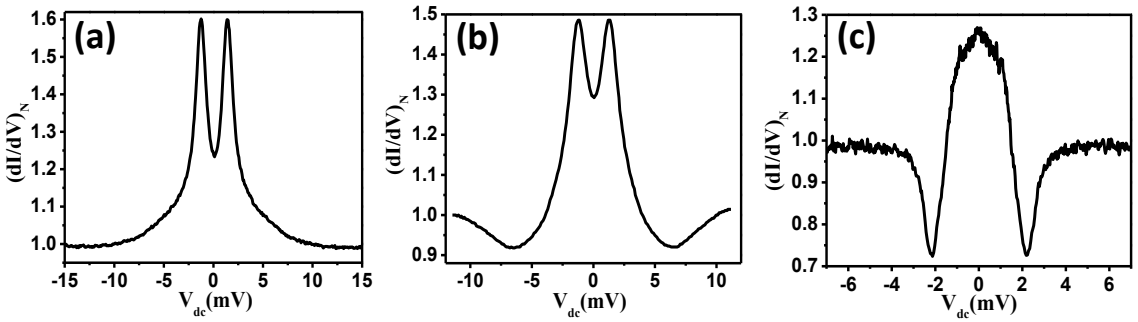


Figure 6.4: Point contact spectra recorded in (a) ballistic (b) intermediate and (c) thermal regime of transport in Pb using silver (Ag) tip.

and rigorous temperature and magnetic field dependent spectroscopic experiments as discussed below.

### 6.2.3 Evolution of spectral features with temperature & magnetic field

In order to further understand the superconducting phase emerging on silicon, we have investigated temperature and magnetic field evolution of the spectroscopic data obtained in the ballistic regime of transport. We show 3D color plots of magnetic field and temperature dependence of point contact spectra obtained on an As-doped Si(111) crystal in figure 6.5 (a) and (b) and corresponding 2D plots are shown in figure 6.5 (c) and (d) respectively. It is clear from the data shown in figure 6.5 that the superconducting energy gap closes systematically with increasing temperature and magnetic fields. We also show the theoretical fits within a modified-BTK (Blonder-Tinkham-Klapwijk) theory. [24] The low-bias parts of the experimentally obtained spectra show remarkable fits with the theoretical spectra. It indicates that the existence of an *s*-wave order parameter may be possible in this case, however, the possibility of a more complex order parameter cannot be ruled out based on this data alone. The temperature dependence of the superconducting energy gap amplitudes obtained from such fitting remain close to the dashed line which shows the expected temperature dependence for conventional superconductors within BCS theory (see figure 6.5 (e)). [25]

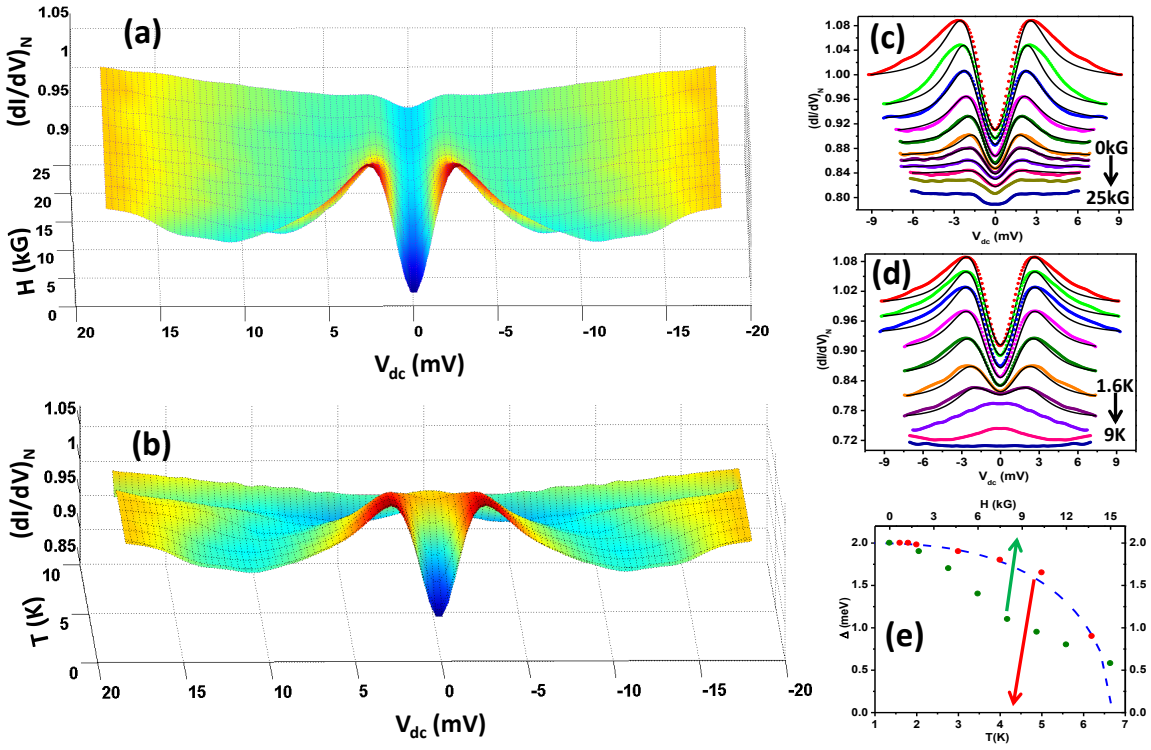


Figure 6.5: (a) 3D plot of Magnetic field dependence of a point-contact (PC) spectra in ballistic regime, (b) 3 D plot of temperature dependence of a point-contact (PC) spectra in ballistic regime. (c), (d) 2 D plots with BTK fitting (black lines) of the spectra (colored lines), (e) Superconducting energy gap ($\Delta$) vs. T and H (Green and red dots) plots extracted from the fits from (c) and (d).

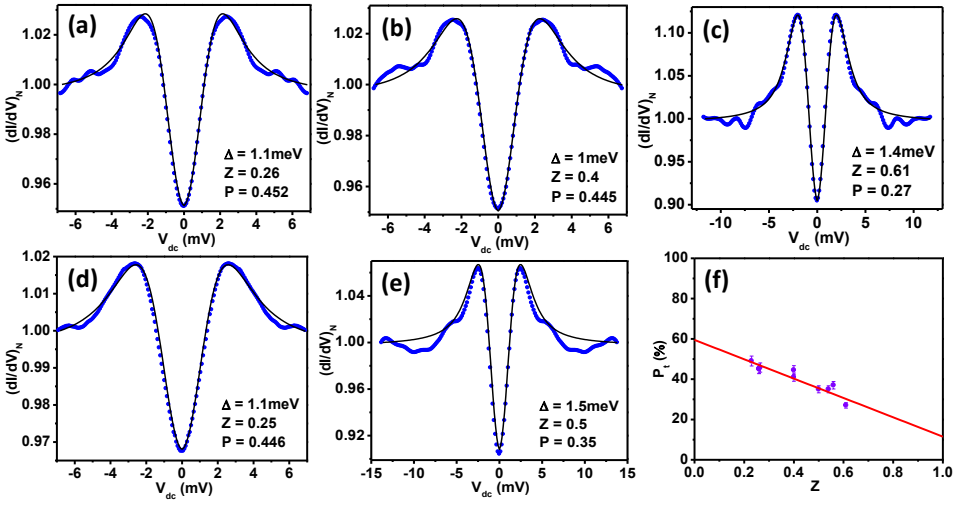


Figure 6.6: (a) - (e) Five representative spectra recorded in ballistic regime of point-contacts on Arsenic-doped Silicon (111). All the spectra are fitted using Modified BTK theory shown as solid lines. (f) Variation of transport spin-polarization $P_t$ with barrier strength $Z$. The red line shows a linear fit of data points and it is extrapolated to $Z = 0$ to extracted the exact value of spin-polarization.

### 6.2.4 Observation of transport spin-polarization

In the analysis of superconducting phase in silicon, we have observed the suppression of Andreev reflection in the measured spectra. This suppression of Andreev reflection is measured by modified BTK theory using an additional parameter which plays the same role as transport spin-polarization ($P_t$) in case of TaAs [17] and CuFeSb. [26] Therefore, it might be possible that silicon acquires a finite spin-polarized character under point-contacts. To measure the degree of such spin-polarization, [27] we acquired a large number of spectra with varying barrier strength ($z$) and analyzed using modified BTK theory [24]. Five such representative spectra are shown in figure 6.6 (a - e). The fitting parameters are listed in the inset of figure 6.6. (a, b, c, d, e). We have plotted $P_t$ as a function of $Z$ as shown in figure 6.6 (f). [17, 26] An extrapolation of the linear fit of the data points ($P_t - Z$ dependence) to $Z = 0$ gives exact value of "intrinsic transport spin polarization" which is approaching 60% (see figure 6.6 (f)). In the past, spin polarization in silicon was attempted to induce to make silicon useful for the purpose of spintronics devices. [28, 29]

### 6.2.5 Other possibilities of superconducting phase

It may also be possible that tungsten (W) is becoming superconducting under some special conditions. In order to rule out such possibilities, the experiments were repeated for W/W and W/Pt point contacts at low temperatures. we did not observed any superconducting feature in such point-contacts.

Superconductivity in silicon is reported in the past under certain special conditions like in amorphous silicon. The critical temperature up to 3 K was observed in amorphous silicon under 25 GPa pressure which is extremely high beyond that much pressure the critical temperature started decreasing. [30] However, it is non-trivial to realize such a high pressure underneath a metallic tip without bending it. If tip bends then it is impossible to obtain a ballistic regime spectra. Moreover, the critical temperature of the TISC phase in silicon is more than 3 times than the superconducting phase under high pressure. Hence, the TISC phase in crystalline silicon presented here does not emerge due to pressure alone.

Such superconducting phase has also been observed in all crystal facets of silicon with both p-type and n-type dopings. Some of the data obtained on other crystal facets with different dopings is included in the next section.

## 6.3 Facet and carrier dependence of superconductivity in silicon

Here we present the realization of TISC in commercially available Si(100) factes with As doping, Si(100) facets with boron (B)-doping and Si(111) facets with As doping. In figure 6.7 (a) we show resistance vs. temperature data at different magnetic fields for a point contact made on the (100) surface of arsenic (As)-doped silicon. At zero field a resistive transition is seen and the transition temperature is seen to decrease systematically with increasing magnetic field. A similar transition is also seen (figure 6.7 (b)) for point contacts made on the (100) facets of boron (B)-doped silicon. The corresponding $H-T$ phase diagrams for As-doped and B-doped Si(100) are shown in figure 6.7 (c) and (d) respectively. Dotted lines indicate the empirically expected $H-T$ phase separation lines for a BCS superconductor. [20] The deviation of the experimentally measured data points from the dotted lines might be due to effects of disorder under the point contacts.

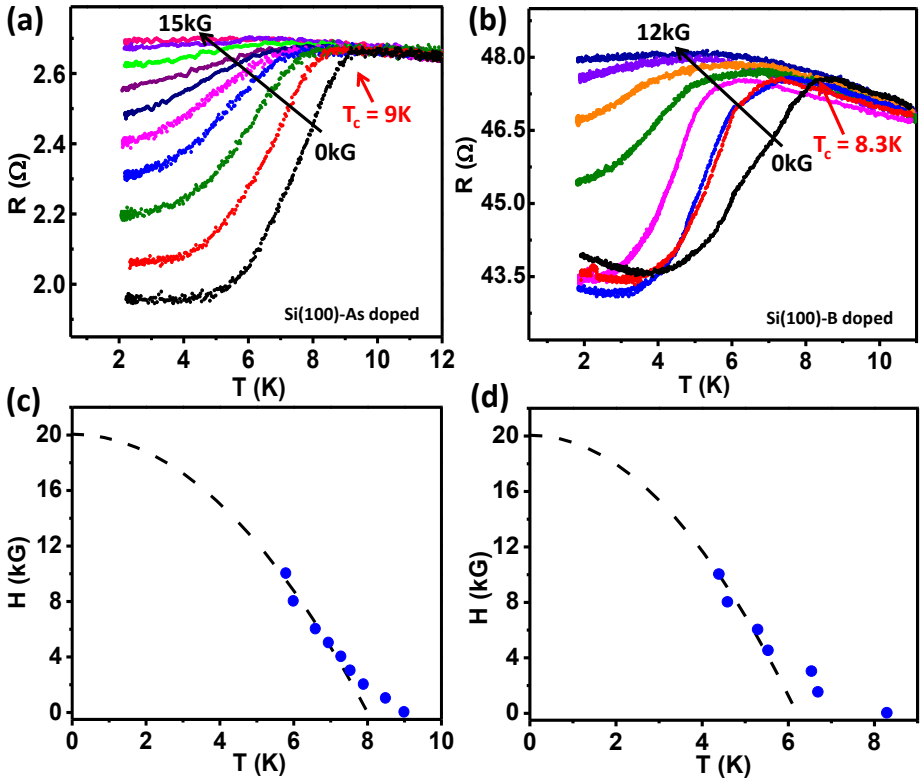


Figure 6.7: (a) Magnetic field dependence of *R*-*T*, the superconducting transition temperature is found to be (a) 9 K for As-doped Si(100) and (b) 8.3 K for B-doped Si(100). (c, d) *H*-*T* phase diagram extracted from (a, b) respectively.

### 6.3.1 Point contact spectroscopy on As-doped Si(100)

In figure 6.8 (a) we show a ballistic regime normalized spectrum on As-doped Si(100). The conductance peaks symmetric about $V$=0 indicate Andreev reflection. The spectrum is also fitted with the modified-BTK theory [24]. The analysis revealed a superconducting energy gap of 2.6 meV. In the intermediate regime, as expected for superconducting point contacts, two dip-structures in conductance also appear which indicate the coexistence of critical current dominated transport along with Andreev reflection (figure 6.8 (b)). The spectroscopic features in the ballistic regime get monotonically suppressed as an externally applied magnetic field is increased (figure 6.8 (d, e)) and the spectral features completely disappear at a magnetic field of 25 kG. The suppression of the features associated with superconductivity is also observed with increasing temperature and the spectrum becomes featureless above the critical temperature of the point contact, which is seen to be 9.5 K.

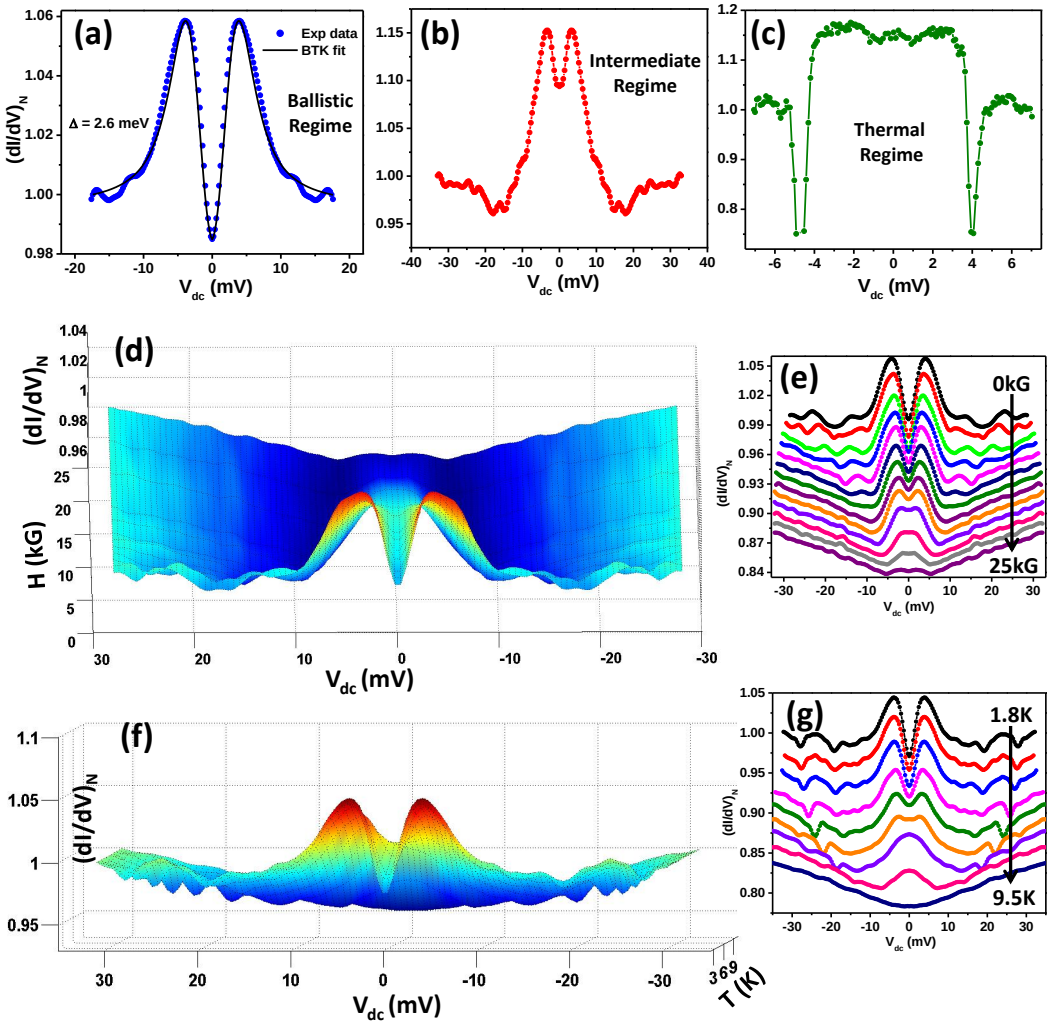


Figure 6.8: (a) A point-contact spectrum showing prominent peaks due to Andreev reflection in the ballistic regime. (b) A spectrum acquired in intermediate regime. (c) A spectrum acquired in thermal regime. (d, f) 3 D plots of magnetic field and temperature dependence of ballistic regime spectra respectively and (e, f) shows respective 2 D plots.

### 6.3.2 Point contact spectroscopy on B-doped Si(100)

When the experiments were performed on B-doped Si(100), spectroscopic signatures of superconductivity were obtained again confirming the existence of TISC. [1] Though the signature of Andreev reflection appeared in the form of two conductance peaks symmetric about $V = 0$ (figure 6.9 (a)), a clean ballistic regime spectrum could not be obtained. This limited us from exact determination of superconducting energy gap using modified BTK theory. [24] Based on an approximate fitting, the estimated energy gap was found to be 1.7 meV which is relatively small considering a critical temperature $\sim 8$ K. The critical current dominated conductance dips evolved systematically with increasing magnetic field (figure 6.9 (b)) and temperature (figure 6.9 (c)). The spectral features disappeared at 13 kG (at 1.4 K) and at 8.1 K (at zero field) respectively. In the ballistic regime, the contact size is smaller. Consequently, while the critical temperature remained to be $\sim 8.4$ K (figure 6.9 (d, e)), the critical field increased up to 20 kG (figure 6.9 (f, g)).

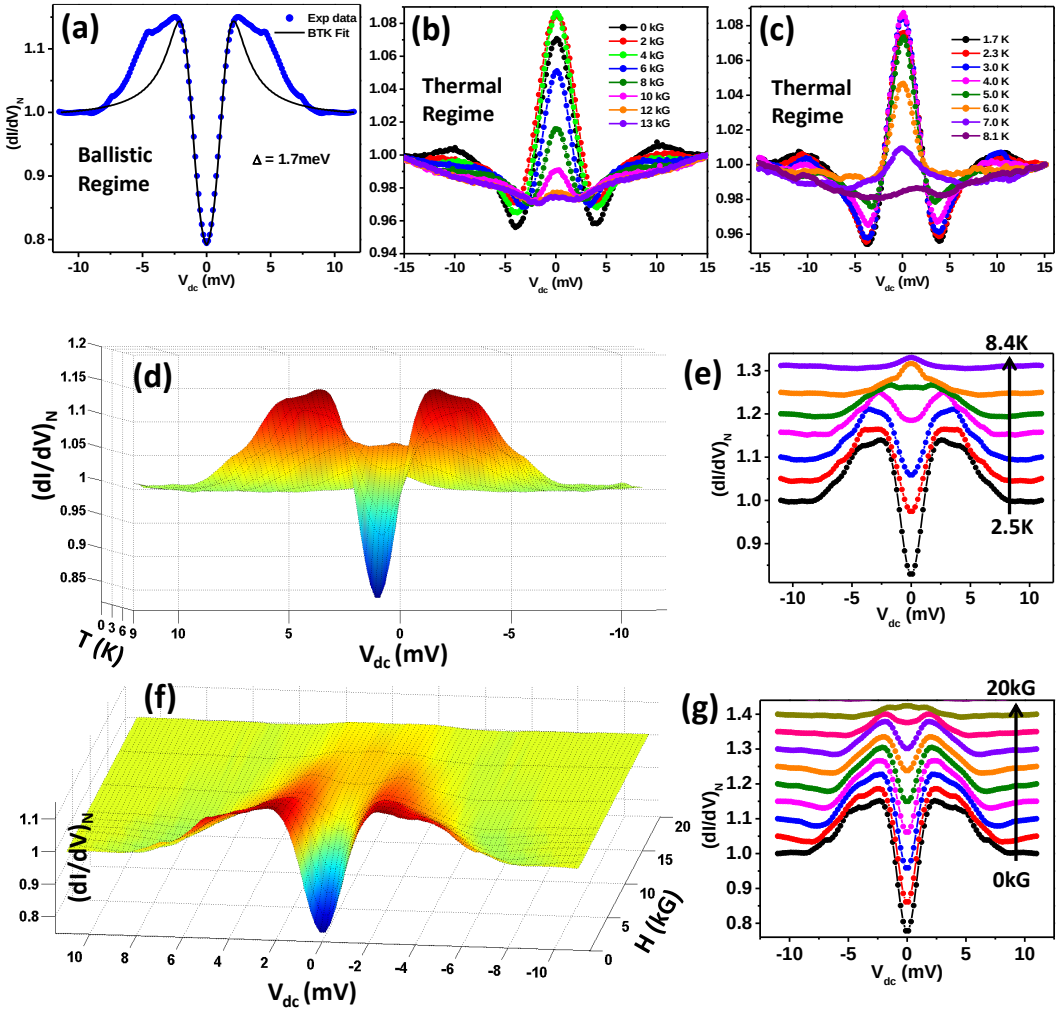


Figure 6.9: (a) Point-contact spectrum acquired on B-doped Si(100) close to the ballistic limit. (b, c) Magnetic field and temperature dependence of thermal regime spectra. (d, e) 3 D plots of temperature and magnetic field dependence of similar spectrum shown in (a) and respective 2 D plots are shown in panels (e, f).

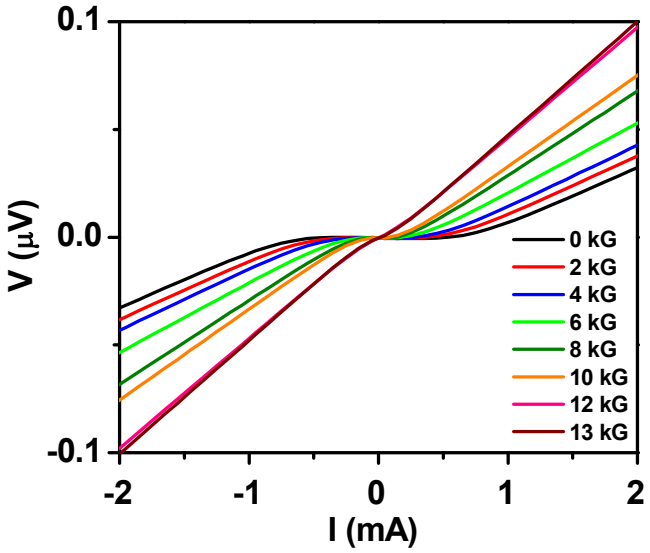


Figure 6.10: Extracted *I*-*V* corresponding to the Maxwell's contribution to the resistance only from the thermal regime *I*-*V*.

While the existence of superconductivity is clear from the field dependent $R-T$ measurements along with spectroscopic signatures in different regimes of mesoscopic transport, it is also possible to directly demonstrate the existence of a dissipationless critical current in the point contacts. [16] We have done this exercise on the point contacts made on B-doped Si(100). For that, we first obtained the $I-V$ characteristics at different magnetic fields on a point contact in the thermal regime of transport. Then we estimated the expected $I-V$ corresponding to the ballistic (Sharvin's) component [19] using BTK theory. [19, 24] After that we subtracted the calculated $I-V$ from the total $I-V$ measured experimentally in the thermal regime of transport. The resultant $I-V$ characteristics and their magnetic field dependence are shown in figure 6.10. The magnetic field dependence of the $I-V$ characteristics thus obtained is consistent with the field-dependent behavior of a critical current dominated $I-V$ of a superconductor. [16]

**Estimation of transport spin polarization**

As it was discussed before, the spectra in the ballistic regime were analyzed using a modified BTK theory. A large number of spectra were analyzed with varying strength of the interfacial barrier ($Z$ in BTK theory) and plotted $P_t$ as a function of $Z$ for B-doped Si(100)/W point contacts. The variation of ballistic regime spectra with magnetic field and temperature for such point contacts are shown in figure 6.11 (a) and (b). Few representative spectra with corresponding theoretical fits and fitting parameters are also listed in figure 6.11 (d). An extrapolation of the $P_t-Z$ dependence to $Z=0$ gives a high value of "intrinsic transport spin polarization" approaching 78% (figure 6.11 (c)).

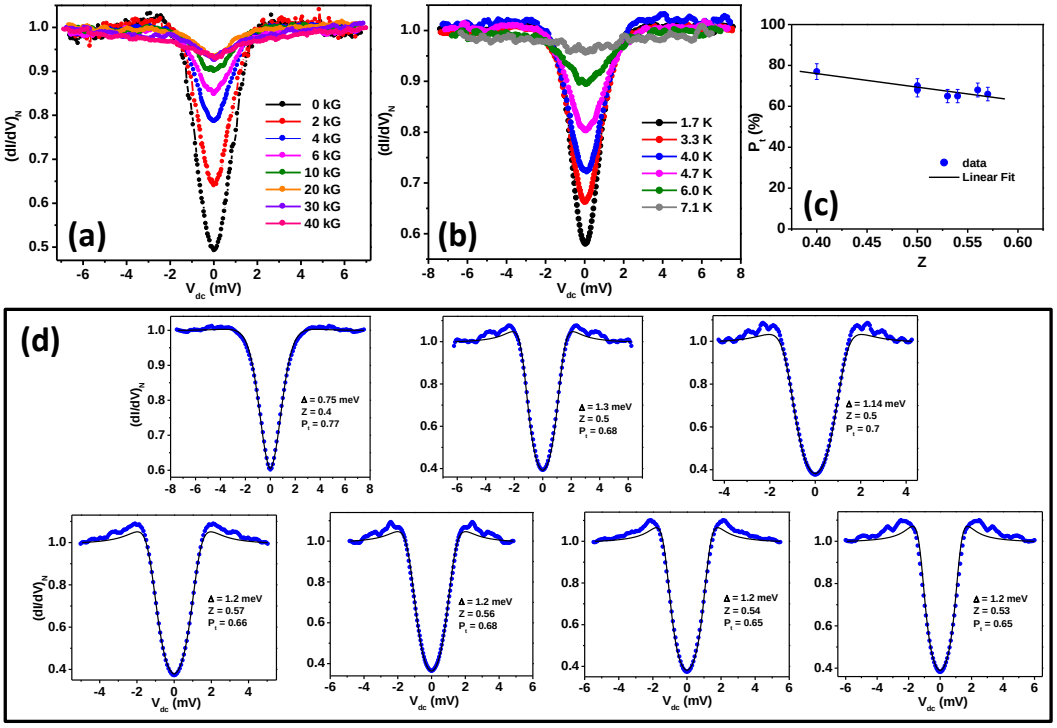


Figure 6.11: (a, b) Magnetic field and temperature dependence of the thermal regime spectra. (d) Seven representative spectra with BTK fittings, fitting parameters are mentioned in the respective insets. (C) Transport spin-polarization is plotted with respect to the barrier strength $Z$ extracted from the fittings of spectra shown in (d). The measured spin-polarization is about 78%

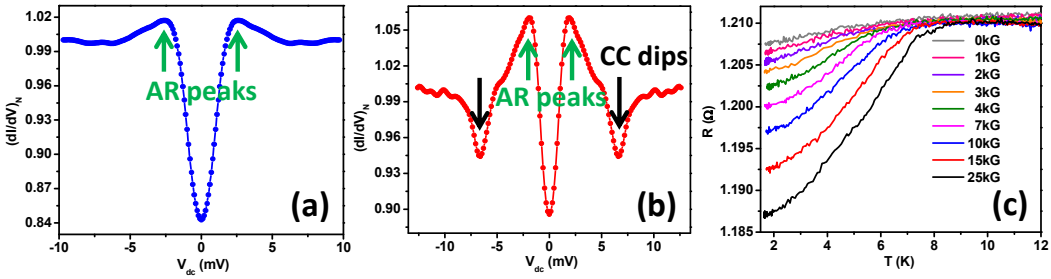


Figure 6.12: Conductance spectrum measured using Cobalt tip (a) in ballistic regime (b) in intermediate regime. (c) *R-T* graph showing superconducting transition at $\approx 8\,K$ *and its magnetic field dependence.*

### 6.3.3 TISC on Silicon with other metallic tips

The tip induced superconducting phase also emerged with other elemental metal like Cobalt and alloy Pt-Ir tips. The similar experiments were performed on As-doped Si(111)/Co and As-doped Si(111)/Pt-Ir point contacts. The spectroscopic signatures along with the resistive transition show superconductivity in silicon induced by cobalt tip. Ballistic regime spectra with the Andreev reflection peaks and intermediate regime spectra with Andreev reflection peaks as well as critical current dips are shown in figure 6.12 (a) and (b) respectively. $R-T$ data, in figure 6.12 (c) show systematic evolution of the critical temperature with magnetic field, as expected for a superconducting point contact. The detailed temperature and magnetic field dependence of the point contact spectra at different regimes of transport are presented in figure 6.13. The critical temperatures for this tip-sample combination varied between ($T_c \sim 8\,K$ *and* $10\,K$). As shown in figure 6.14, similar observations were also made with Pt-Ir tips. In case of Pt-Ir tips, the critical temperature was found to be $T_c \sim 8$ K.

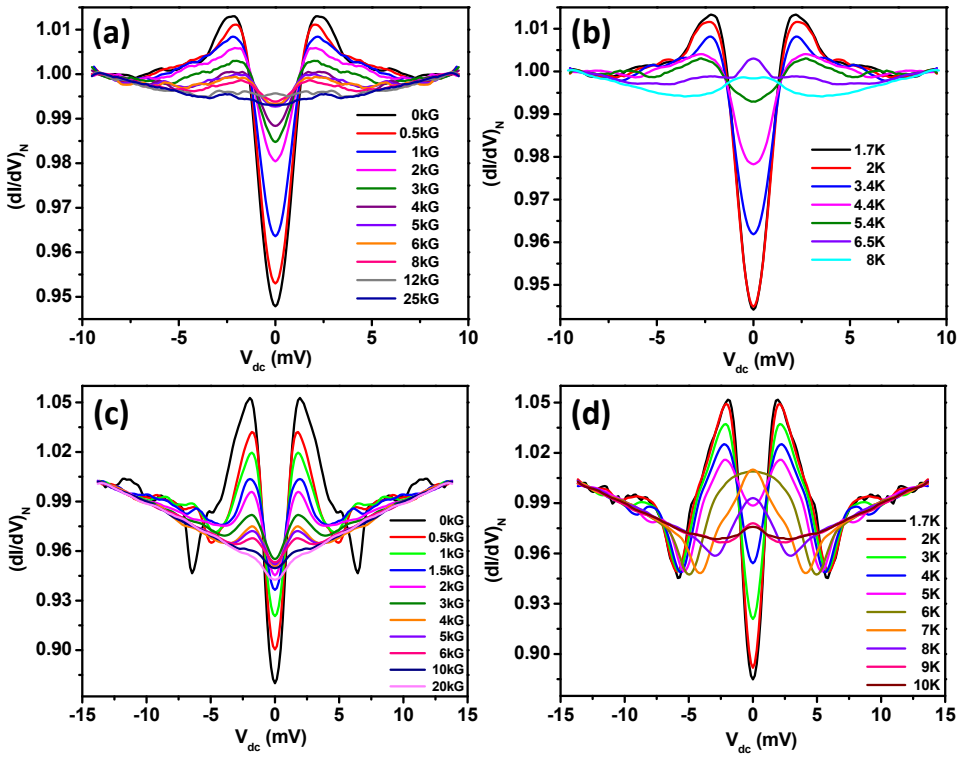


Figure 6.13: Magnetic field and temperature dependence of (a, b) ballistic and (c, d) intermediate regime spectra measured using Cobalt tip respectively.

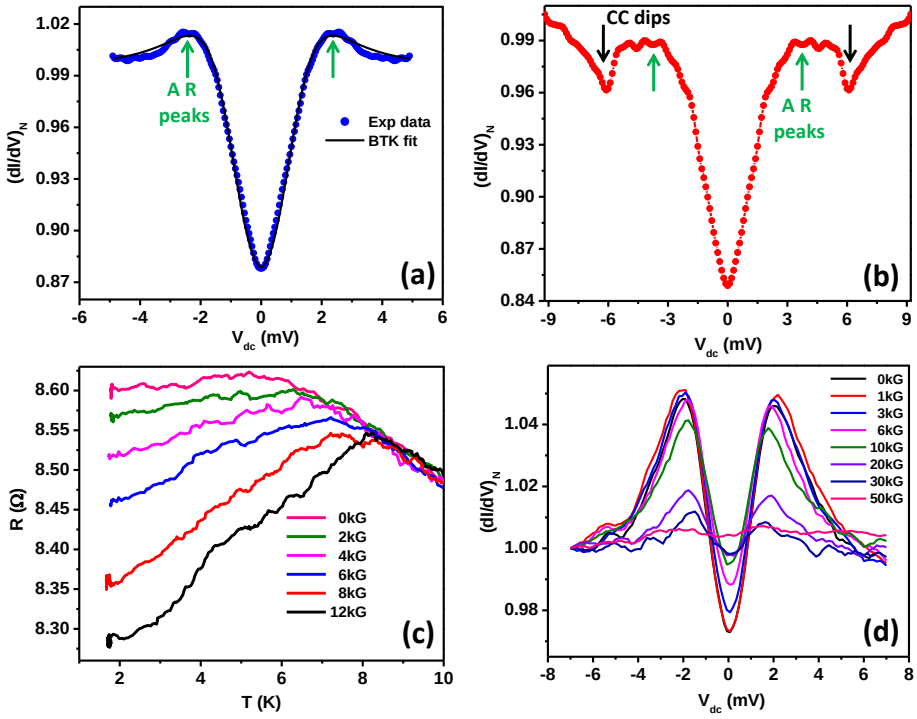


Figure 6.14: Point-contact spectra measured using Pt-Ir tip in the (a) ballistic regime and (b) intermediate regime of transport. (c) Magnetic field evolution of (c) *R-T* and (d) ballistic regime spectrum.

## 6.4 Summary

In summary, we have discovered a tip-induced superconducting phase in moderately doped silicon with the critical temperature of $\sim$ 11 K which is found to be remarkably high. Detailed analysis of temperature and magnetic field dependence of the spectra revealed a strong possibility of a conventional order parameter in the superconducting phase observed in silicon under point-contacts. These observations are expected to stimulate theoretical studies for understanding this surprisingly high temperature superconducting phase realized on silicon. We have also observed finite transport spin-polarization in silicon under point-contacts. The ballistic regime point-contact spectra can be fitted well with modified BTK theory with finite transport spin polarization $P_t$.

In this chapter, we have also shown that a TISC phase can be realized on all the facets of commercially available single crystals of silicon with different types of doping. No systematic dependence of the critical temperature was observed either on the type of carrier or on the surface on which the point contacts are made. We have also shown that the TISC phase can also be realized using tips of other metals like Pt-Ir and ferromagnetic cobalt.

Our claim of TISC phase in moderately doped silicon is based on a large amount of data which we have obtained on all crystal facets of silicon including <111>, <110> and <100> with both arsenic and boron dopings.

# Bibliography


[1] A. Sirohi, S. Gayen, M. Aslam and G. Sheet, Appl. Phys. Lett. **113**, 242601 (2018).

[2] M. Ieong, B. Doris, J. Kedzierski, K. Rim, and M. Yang, Science **306**, 2057 (2004).

[3] D. H. Kim, J. H. Ahn, W. M. Choi, H. S. Kim, T. H. Kim, J. Song, Y. Y. Huang, Z. Liu, C. Lu, and J. A. Rogers, Science **320**, 507 (2008).

[4] I. Žutić, and J. Fabian, Nature **447**, 268 (2007).

[5] M. P. Delmo, S. Yamamoto, S. Kasai, T. Ono, and K. Kobayashi, Nature **457**, 1112 (2009).

[6] T. F. Rosenbaum, K. Andres, G. A. Thomas, and R. N. Bhatt, Phys. Rev. Lett. **45**, 1723-1726 (1980).

[7] P. Dai, Y. Zhang, and M. P. Sarachik, Phys. Rev. Lett. **66**, 1914-1917 (1991).

[8] J. E. Duvauchelle, A. Francheteau, C. Marcenat, F. Chiodi, D. Debarre, K. Hasselbach, J. R. Kirtley, and F. Lefloch, Appl. Phys. Lett. **107**, 072601 (2015).

[9] D. Connétable, V. Timoshevskii, B. Masenelli, J. Beille, J. Marcus, B. Barbara, A. M. Saitta, G. -M. Rignanese, P. Mélinon, S. Yamanaka, *et al.* Phys. Rev. Lett. **91**, 247001 (2003).

[10] L. Boeri, J. Kortus, and O. K. Andersen, Phys. Rev. Lett. **93**, 237002 (2004).

[11] M. L. Cohen, Phys. Rev. **134**, A511-A522 (1964).

[12] R. J. Cava, Nature **444**, 427 (2006).

[13] E. Bustarret, C. Marcenat, P. Achatz, J. Kačmarčik, F. Lévy, A. Huxley, L. Ortéga, E. Bourgeois, X. Blase, D. Débarre, *et al.* Nature **444**, 465-468 (2006).

[14] K. J. Chang, M. D. Michel, and M. L. Cohen, Phys. Rev. Lett. **54**, 2375-2378 (1985).

[15] D. Erskine, P. Y. Yu, K. J. Chang, and M. L. Cohen, Phys. Rev. Lett. **57**, 2741-2744 (1986).

[16] L. Aggarwal, A. Gaurav, G. S. Thakur, Z. Haque, A. K. Ganguli, and G. Sheet, Nature Materials **15**, 32 (2016).

[17] L. Aggarwal, S. Gayen, S. Das, R. Kumar, V. Süß, C. Felser, C. Shekhar, and G. Sheet, Nature Communications **8**, 13974 (2017).

[18] S. Das, L. Aggarwal, S. Roychowdhury, M. Aslam, S. Gayen, K. Biswas, and G. Sheet, Appl. Phys. Lett. **109**, 132601 (2016).

[19] A. Wexler, Proc. Phys. Soc. **89**, 927-941 (1966).

[20] Y. G. Naidyuk, and I. K. Yanson, Point-contact Spectroscopy Springer Newyork, (2004).

[21] S. Datta, Electronic Transport in Mesoscopic Systems Cambridge University Press, (1995).

[22] G. Sheet, S. Mukhopadhyay, and P. Raychaudhuri, Phys. Rev. B **69**, 134507 (2004).

[23] A. Sirohi, P. Saha, S. Gayen, A. Singh, and G. Sheet, *Nanotechnology* 27, 285701 (2016).

[24] G. E. Blonder, M. Tinkham, and T. M. Klapwijk, Phys. Rev. B **25**, 4515-4532 (1982).

[25] J. Bardeen, L. N. Cooper, and J. R. Schrieffer, Phys. Rev. **108**, 1175 (1957).

[26] A. Sirohi, C. K. Singh, G. S. Thakur, P. Saha, S. Gayen, A. Gaurav, S. Jyotsna, Z. Haque, L. C. Gupta, M. Kabir, *et al.* Appl. Phys. Lett. **108**, 242411 (2016).

[27] I. I. Mazin, Phys. Rev. Lett. **83**, 1427–1430 (1999).

[28] I. Appelbaum, B. Huang, and D. J. Monsma, Nature **447**, 295-298 (2007).

[29] S. P. Dash, S. Sharma, R. S. Patel, M. P. De Jong, and R. Jansen, Nature **462**, 491-494 (2009).

[30] T. H. Lin, W. Y. Dong, K. J. Dunn, and C. N. J. Wagner, Phys. Rev. B **33**, 7820 (1986).

Appendix A

# Indication of unconventional superconducting pairing in Pb nano-islands

Here, we present the observation of unconventional superconducting pairing in Pb nano-islands under mesoscopic point-contacts. The work presented here is published in Nanotechnology. [1]

## A.1 Introduction

Nano-structures of some of the elemental superconductors show significantly different superconducting properties from the bulk [2, 3] like superconductivity in Nb nano-particles disappears below certain critical particle diameter. Such observations were attributed to the change in the electronic structure with change in the particle diameter and to the modified electron-phonon coupling strength. In fact, there are systems where superconducting properties are affected by the fundamental interaction terms like spin-orbit coupling. Superconductivity in materials with strong spin-orbit coupling is receiving renewed interest following the discovery of superconductivity in some of the topologically non-trivial materials including the topological insulators [4] and the topological Dirac semi-metals. [5–7] Elemental Pb is the unique and simplest superconducting system among those with strong spin-orbit coupling [8]. Elemental bulk Pb is a type I conventional superconductor with the critical temperature ($T_c$) of 7.2 K and the critical magnetic field ($H_c$) of approximately 800 Oe. The Cooper pairing in Pb is thought to be mediated by electron-phonon interactions [8–10]. Furthermore, experiments on Pb nano-particles and nanowires have shown non-type I nature of superconductivity where the critical field is enhanced by several orders of magnitude [11–13]. Here we present the trapping of nano-droplets of Pb under a mesoscopic point contact with silver (Ag) tip and show that the superconducting properties of such confined nano-islands are significantly different from bulk Pb and is strongly affected by the high spin-orbit coupling of Pb. We have also observed a clear indication of an unconventional pairing.

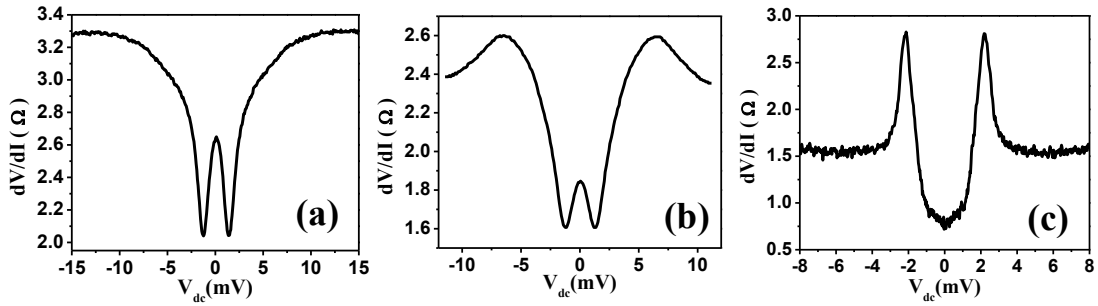


Figure A.1: (a) A $dV/dI$ vs. $V$ spectrum obtained in the ballistic regime showing two symmetric dips about $V$=0 due to Andreev reflection. (b) A spectrum obtained in an intermediate regime where the peaks due to critical current and dips due to Andreev reflection in $dV/dI$ vs. $V$ are present. (c) A spectrum in the thermal regime with sharp critical current peaks.

## A.2 Experimental details and results

The qualitative spectral features of point-contacts depend on the regime of mesoscopic transport as decided by the size of the point-contacts relative to the elastic and inelastic mean free paths [14, 15]. All such features associated with superconductivity of the point-contacts are shown in figure A.1. The spectral features associated with superconductivity also show systematic evolution with temperature and magnetic field. From our experiments, we show that the mesoscopic point-contacts involving Pb couple non-trivially with magnetic field.

In figure A.1 (c) we show a Pb-Ag point-contact spectra at zero magnetic field in the thermal regime where two strong critical current driven peaks in $dV/dI$ symmetric about $V = 0$ are observed. As shown in figure A.2 (a), when a magnetic field of 1.6 kG is applied parallel to the direction of current flow, the height of the $dV/dI$ peaks obtained in the thermal regime point-contact (figure A.1 (c)) becomes asymmetric – the peak height for positive bias is higher than that for the negative bias. When the magnetic field direction is reversed, the asymmetry in peak height also gets switched (figure A.2 (b)). This behaviour has been observed consistently and reproducibly for more than 50 point-contacts in the thermal regime.

In figure A.3 (a) we show a 3D plot of the magnetic field dependence of $dV/dI$ for the same point-contact discussed above. Surprisingly, the asymmetry in peak height is seen to oscillate until all the features associated with superconductivity disappear at 1.6 T. We have also performed the experiment with the magnetic field applied in a direction antiparallel to the direction of current flow and the critical field and other associated superconducting properties (like, coherence length) was found to be same as when the field was applied parallel to the direction of current. In figure A.3 (b) we show how the ratio of the differential resistance corresponding to the smaller peak ($R_s$) and the larger peak ($R_L$) oscillates with magnetic field. The oscillation of $R_s$ alone is shown in figure A.3 (c).

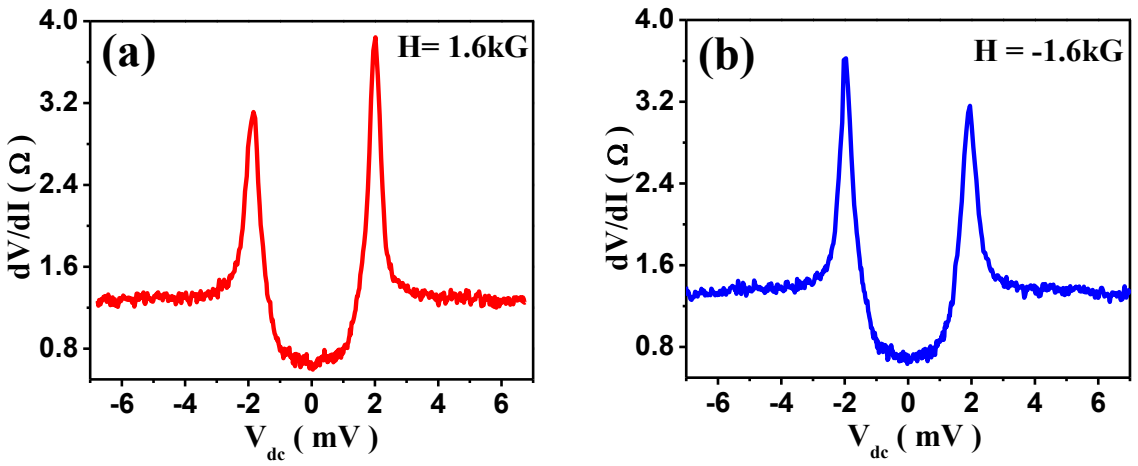


Figure A.2: A spectrum in the thermal regime with a magnetic field of 1.6 kG applied (a) parallel and (b) anti-parallel to the direction of current in a point-contact. The spectrum becomes asymmetric and switches this asymmetry with reversing the direction of magnetic field.

The superconducting transition at 7.2 K of a thermal regime point-contact (as shown in figure A.1 (c)) is clearly seen in the resistance ($R$) vs. temperature ($T$) plot at zero-bias (see figure A.4 (a)). The transition temperature is seen to systematically decrease with increasing the strength of a magnetic field applied parallel to the direction of current flow. The $H-T$ phase diagram shown in figure A.4 (b) has been extracted from the magnetic field dependent $R-T$ data. It is clear that the critical magnetic field up to which superconductivity survives in this point-contact is 1.6 T which is significantly higher than the bulk critical field of Pb (800 Oe). Therefore, when a magnetic field of strength between 800 Oe and 1.6 T is applied on this point-contact, the superconductivity of the bulk is destroyed and only a small mesoscopic region under the point-contact remains superconducting. In figure A.4 (b) we also show the empirically expected plot of the phase diagram for a conventional superconductor as a dotted line. At temperatures closer to $T_c$ it is observed that the experimentally obtained $H-T$ curve deviates slightly from the empirical curve and shows a concave curvature instead of convex. This might be due to the presence of an unconventional superconducting component in the point-contact. [5]

The magnetic field driven anisotropy of the $dV/dI$ spectra with the sign of applied bias in the thermal regime could be understood if the effective spin-orbit coupling of Pb is modified depending on the direction of the applied magnetic field with respect to the applied electric field (bias). [16] From the data it appears that when the magnetic field is parallel to the electric field, the effective spin-orbit coupling is suppressed and when the magnetic field is anti-parallel to the electric field, the effective spin-orbit coupling is enhanced thereby leading to the asymmetric $dV/dI$. The absolute values of $R_s$ and $R_L$ give an estimate of how fast or slow does the

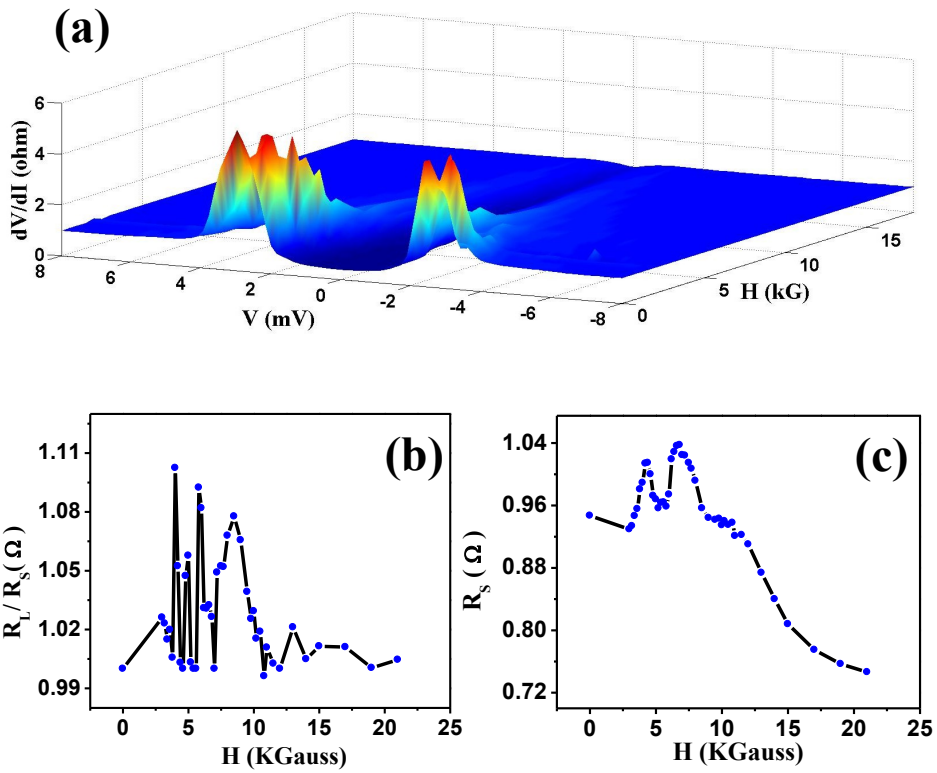


Figure A.3: (a) A 3D plot of $dV/dI$ vs. $V$ spectra in the thermal regime. (b) The oscillation of the ratio of the resistance of the higher peak and the lower peak extracted from magnetic field dependent data. (c) The evolution of the smaller peak in the magnetic field.

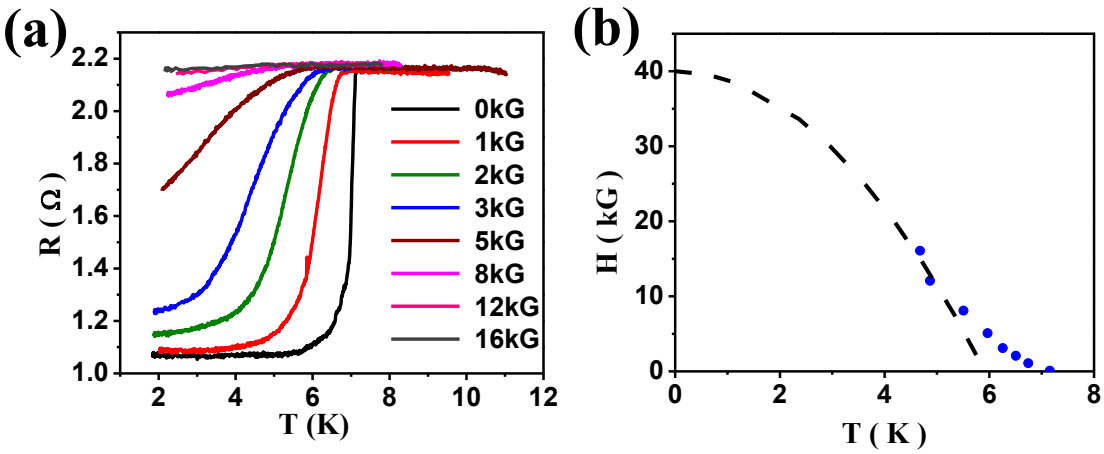


Figure A.4: (a) Resistance vs. temperature data of the point-contact showing superconducting transition and its Magnetic field dependence. (b) The extracted $H$–$T$ phase diagram from (a).

superconducting point-contact achieve its normal state resistance when the current through the point-contact is gradually increased. These values oscillate while the absolute value of the critical current as determined by the position of the peaks in the $dV/dI$ spectra does not oscillate with magnetic field. At present we cannot provide a theoretical understanding of this intriguing observation, but we believe that such non-trivial coupling of the point-contact with magnetic field could be related to the high spin-orbit coupling of Pb based on direct comparison of results on high spin-orbit coupling Pb point contacts with very low spin-orbit coupling Nb point contacts. The thermal limit spectra at different magnetic fields on Nb point contacts are shown in figure A.5. It is seen that while the sharp conductance peaks driven by critical current get suppressed, no magnetic field dependent asymmetry is observed up to a magnetic field of 5 kG.

At the surface of Pb where the point-contacts are formed, the inversion symmetry is broken and the system in principle is allowed to mix in a triplet component [17, 18], possibly with breaking time reversal symmetry ($s+ip$). Such a state could, in principle, couple with magnetic field in a non-trivial manner. The idea of the emergence of a spin triplet component in the order parameter here is further supported by earlier experimental observations where it was shown that lattice dislocation might enhance superconductivity in a spin triplet superconductor. [19] In the present case, the point contact could act like a local defect and as per the work mentioned above, the observed enhancement of the superconductivity at the mesoscopic Pb point contact might indicate the existence of a spin-triplet component in the order parameter of the superconductor forming the point contact. The spin triplet component in mesoscopic Pb which is a conventional superconductor in the bulk could be, as discussed before, due to the known high spin orbit coupling in Pb.

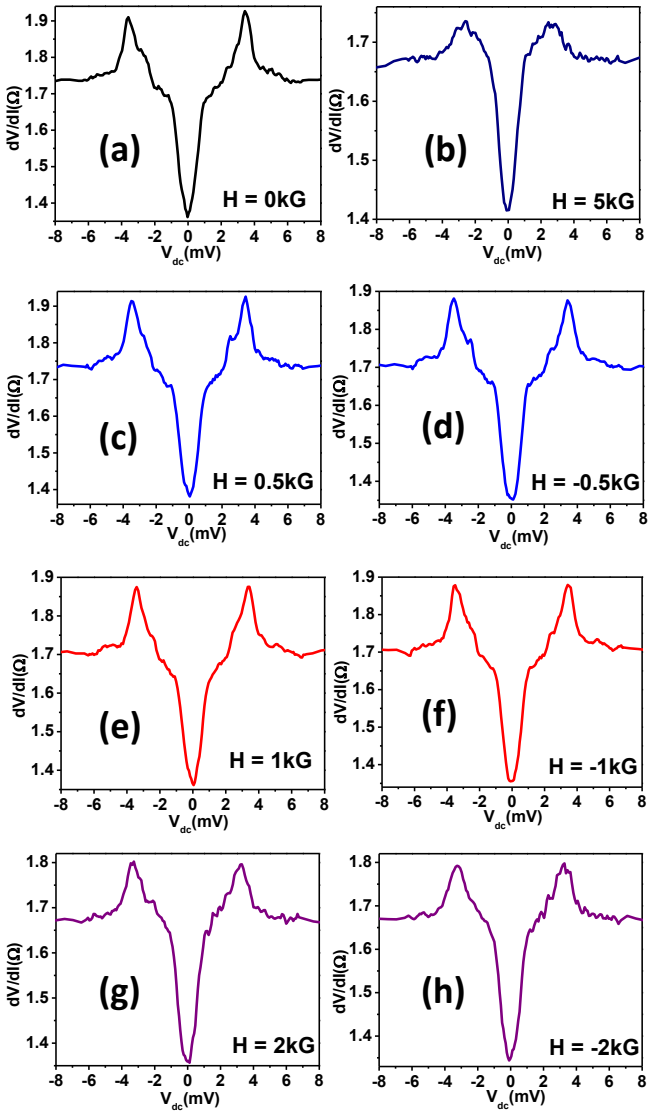


Figure A.5: Point contact spectrum obtained in the thermal regime showing critical current peaks symmetric about $V$=0 in magnetic fields, corresponding magnetic field values are given in the respective insets. The spectrum is symmetric and there is no change with reversing the direction of magnetic field.

## A.3 Conclusions

In conclusion, from the detailed magnetic field dependent studies of the transport properties of mesoscopic point-contacts formed between superconducting Pb and Ag we have shown that in mesoscopic dimensions, magnetic field induced asymmetric spectral features are observed. We surmise that such asymmetric properties can be understood if the strong spin-orbit coupling of Pb is considered. We have also discussed the possibility of an unconventional component of the order parameter for mesoscopic Pb.

# Bibliography


[1] A. Sirohi, P. Saha, S. Gayen, A. Singh and G. Sheet Nanotechnology, **27**, 285701 (2016).

[2] F. Y. Wu, C. C. Yang, C. M. Wu, C. W. Wang, & W. H. Li, J. of Appl. Phys. **101**, 09G111 (2007).

[3] S. Bose, P. Raychaudhuri, R. Banerjee, P. Vasa & P. Ayyub, Phys. Rev. Lett. **95**, 147003 (2005).

[4] Y. S. Hor, *et.al.*, Phys. Rev. Lett. **104**, 057001 (2010).

[5] L. Aggarwal, A. Gaurav, G. S. Thakur, Z. Haque, A. K. Ganguli & G. Sheet, Nature Materials **15**, 32-37 (2016).

[6] L. P. He, Y. T. Jia, S. J. Zhang, X. C. Hong, C. Q. Jin & S. Y. Li, *et.al.*, arXiv:1502.02509 (2015).

[7] S. Koyabashi, M. Sato, arXiv:1504.07408.

[8] J. R. Anderson, A.V. Gold, Phys. Rev. **139**, A1459 (1965).

[9] R. Heid, K. P. Bohnen, Phys. Rev. B **81**, 174527 (2010).

[10] I. Y. Sklyadneva, R. Heid, P. M. Echenique, K. B. Bohnen & E. V. Chulkov, Phys. Rev. B **85**, 155115 (2012).

[11] C. C. Yang, F. C. Tsao, S. Y. Wu, W. H. Li & K. C. Lee, Journal of Low Temp. Phys. **131**, 3/4 (2003).

[12] J. G. Rodrogo, V. Crespo, H. Suderow, S. Vieira & F. Guine, Phys. Rev. Lett. **109**, 237003 (2012).

[13] M. He, C. H. Wong, P. L. Tse, Y. Zheng, H. Zhang, F. L. Y. Lam, P. Sheng, X. Hu & R. Lortz, ACS Nano **7**, 4187 (2013).

[14] Yu. G. Naidyuk & I. K. Yanson, Point Contact Spectroscopy **145**, 0171 (2005).

[15] S. Dutta, Electronic Transport in Mesoscopic Systems **0521**, 41604 (1999).

[16] H. Wang, *et .al*., Scientific Reports **4**, 5817 (2014).

[17] Y. Yanase, S. Takamatsu & M. Udagawa, arXiv: 1408.6353 (2014).

[18] S. Takamatsu & Y. Yanase, arXiv: 1305.4494 (2015).

[19] Y. A. Ying, N. E. Staley, Y. Xin, K. Sun, X. Cai, D. Fobes, T. J. Liu, Z. Q. Mao & Y. Liu, Nat. Comm. **4**, 2596 (2013).

Appendix B

# High spin-polarization in CuFeSb

Here, we present the observation of high spin-polarization and unique ferromagnetic ground state in CuFeSb. The spin-polarization is measured by transport measurements of point-contacts made between CuFeSb and a superconductor (Nb and Pb). The work presented in this appendix is published in Applied Physics Letters. [1]

## B.1 Introduction

CuFeSb is isostructural to the ferro-pnictide and chalcogenide superconductors. Usually the parent compounds of the pnictide and the chalcogenide superconductors are known to be antiferromagnetic where the antiferromagnetism is thought to be promoted by spin density waves (SDW) associated with Fermi surface nesting [2–4]. More recently it has been shown that CuFeSb, which is isostructural to the iron-based layered superconductors e.g., Li(Na)FeAs [5], has a ferromagnetic ground state [6]. A close relative of this compound CuFeAs stabilizes in an antiferromagnetic ground state with a Neel temperature of 9 K [7]. The ferromagnetic order in CuFeSb is thought to originate from the large height of Sb from the Fe plane. This fact also supports the hypothesis that the competing magnetic interactions in ferro-pnictide superconductors is decided by the anion height i.e., there is a gradual change in the magnetic properties from superconductivity to antiferromagnetism to ferromagnetism on moving in the increasing order of anion height from LiFeAs to CuFeAs to CuFeSb [6–8]. CuFeSb is known to be one of the very few materials in the FeAs or FeSb family that shows a ferromagnetic ground state. Therefore it is most important to understand the Fermi surface properties of this unique system by spectroscopic measurements – particularly, the nature of the Fermi surface spin polarization and the degree of spin fluctuations.

Here, we have employed spin-resolved Andreev reflection spectroscopy using conventional superconducting tips to measure the spin polarization at the Fermi level of CuFeSb [9]. From the analysis of the Andreev reflection data between the superconductor and the ferromagnet, we

found the evidence of a high degree of transport spin polarization approaching 47% in CuFeSb.

## B.2 Experimental results

In figure B.1 (a - h) we show eight representative Andreev reflection spectra between a Nb/Pb-tip and CuFeSb. The spectra clearly show the double-peak structure symmetric about $V = 0$, which is the hallmark of Andreev reflection. For low values of $Z$, these peaks appear close to the energy gap of the superconductor. The solid lines show the theoretical fits as per the model described in chapter 2. The superconducting energy gap of niobium is found to vary from contact to contact and fall approximately between $0.8\,meV$ and $0.9\,meV$ for all the point-contacts that we have analyzed, indicating that the proximity of the ferromagnet suppresses the superconductivity of the point-contacts slightly. The value of $\Gamma$ remained zero for all the spectra, which means the broadening due to finite quasi-particle lifetime is absent at the point-contact. This fact also indicates that the spin-fluctuation in the system is not significant as strong spin-fluctuations is also known to give rise to large $\Gamma$ [10]. Therefore, the theoretical fits are obtained by essentially tuning two parameters namely $Z$ and $P_t$, this makes the fit accurate and the fitting parameters unique. It is found that the raw data deviate slightly from the fit at certain points (notice the dip structures in $dI/dV$). Such deviation is known to originate from the critical current of the superconductor when a small part of the Maxwell's resistance is also measured along with the Sharvin resistance in the point-contacts close to the ballistic regime. [11]

The experiments were repeated with superconducting Pb-tips to confirm the reproducibility (figure B.1 (a - d)). It is seen that the theoretical fitting to the experimentally obtained spectra obtained with Pb tips is very good and the critical current driven dips are absent. This is due to the existence of a thick oxide layer on the surface of Pb that is broken by the application of mechanical pressure for the formation of point contacts thereby leading to extremely small diameter contacts where ballistic transport dominates. The value of $\Gamma$ remained almost zero for all the fittings and the superconducting energy gap was found to vary approximately between $0.8\,meV$ and $1.2\,meV$ which is consistent with the superconducting energy gap of bulk Pb.

The dependence of $P_t$ on $Z$ for both Nb and Pb based point-contacts is shown in figure B.2. For most of the Nb/CuFeSb point-contacts, the value of $Z$ was found to be small ($< 0.2$) For such point-contacts, the maximum measured value of $P_t$ is found to be 47%. For both the Nb/CuFeSb and the Pb/CuFeSb point contacts $P_t$ did not change noticeably with $Z$. The conventional way of finding the intrinsic transport spin polarization is to extrapolate the $P_t$ vs. $Z$ curve to $Z = 0$. By doing this extrapolation, the intrinsic $P_t$ is found to be approximately 47% which is nearly equal to the value measured with the Nb tip.

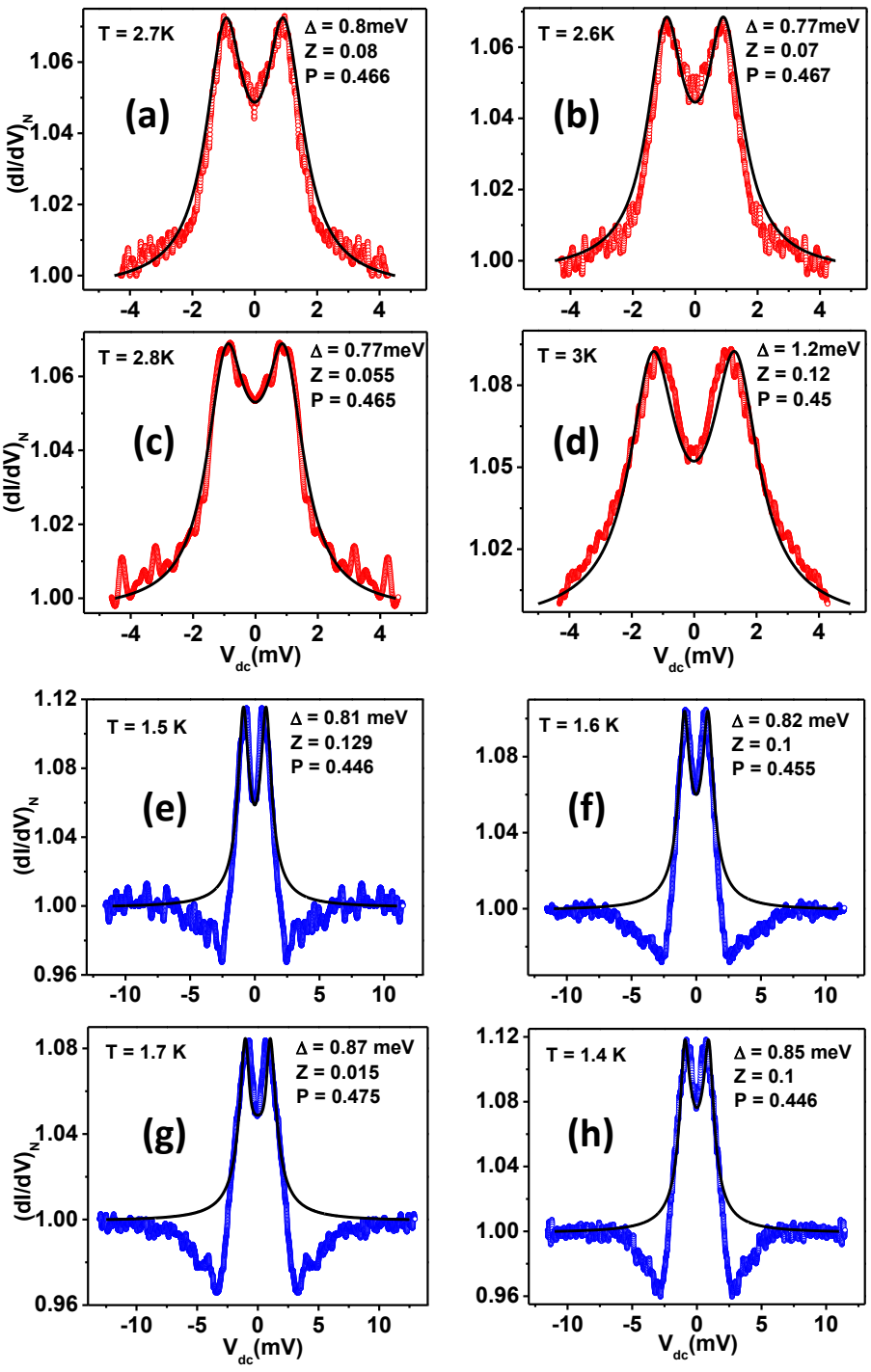


Figure B.1: Representative point-contact spectra in the ballistic regime between superconducting (a-d) Pb/CuFeSb and (e-h) Nb/CuFeSb point-contact. The fitting parameters are listed in the insets respectively.

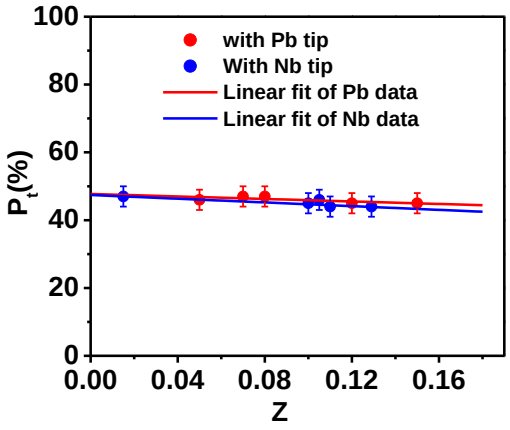


Figure B.2: The transport spin-polarization $P_t$ vs. Z plot for point-contacts on CuFeSb with Nb and Pb tips.

## B.3 Theoretical calculations

In order to understand the unique ferromagnetic ground state of CuFeSb and the origin of the observed high spin polarization, we have performed spin-polarized band structure calculation of CuFeSb. The first-principles calculations were performed within spin-polarized density functional theory using projector augmented wave formalism. [12, 13] The structural parameters of the optimized tetragonal [$P4/nmm$, shown in figure B.3 (a)] CuFeSb are in excellent agreement with the current and previous [14] experimental measurements (see table B.1). The CuFeSb crystal structure is analogous to other iron pnictides and chalcogenides, though there are some striking differences from the superconducting ones. For example, while compared with the superconducting LiFeAs, (a) the Sb–Fe–Sb angles are substantially different than As–Fe–As angles, and (b) the Fe–Sb bond length is significantly larger as shown in table B.1. Thus, the height of Sb (As) from the Fe plane is strikingly different for CuFeSb [$z_{\mathrm{Sb}}$=1.89 Å (DFT-PBE), and 1.87 Å (experiment)] and LiFeAs ($z_{\mathrm{As}}$=1.51 Å), [5] and this $z_{\mathrm{anion}}$ is predicted to play an important role in determining the electronic structure. [15] Further calculations shows that for CuFeSb the narrow $d$ band near the Fermi level and very high $N(E_F)$ the magnetic Stoner instability takes over, and the Fe-layer becomes ferromagnetic similar to the case of ferromagnetic MgFeGe.

Next we calculate the transport spin polarization $P_t$. Within classical Bloch-Boltzmann transport theory, $P_t$ can be defined in terms of spin-dependent current densities, and in general, [**?**]

$$P_t^n = \frac{\langle N(E_F)v_F^n\rangle_\uparrow - \langle N(E_F)v_F^n\rangle_\downarrow}{\langle N(E_F)v_F^n\rangle_\uparrow + \langle N(E_F)v_F^n\rangle_\downarrow},$$

where $v_F$ is the spin polarized Fermi velocity of electrons. Thus by definition $P_t^n$ is connected to the the spin polarization measured in various experiments, spin resolved photo-emission ($n = 0$) and point-contact spectroscopy in ballistic ($n = 1$) and diffusive ($n = 2$) regimes. In

Table B.1: Refined structural parameters for CuFeSb obtained at 300K, which is below the ferromagnetic transition temperature. The number in the square bracket indicates the number of symmetric bond lengths.

| | | | | | | |
|---|---|---|---|---|---|---|
| $P4/nmm$: | $a = b = 3.9117(3)$ Å, $c = 6.2619(4)$ Å (300K) | | | | | |
| | $a = b = 3.9347(2)$ Å, $c = 6.2515(4)$ Å (400K) | | | | | |
| | $a = b = 3.91$ Å, $c = 6.32$ Å (DFT-PBE) | | | | | |
| | | $x$ | $y$ | $z$ | $B$ (Å$^2$) | Wyckoff positions |
| Atomic coordicates | Cu | 0.25 | 0.25 | 0.7127(3) | 1.68(6) | 2c |
| | Fe | 0.75 | 0.25 | 0 | 1.69(1) | 2b |
| | Sb | 0.25 | 0.25 | 0.2981(1) | 1.19(4) | 2c |
| | Bond lengths (Å) | | | | Sb–Fe–Sb angles (°) | |
| | Fe–Sb [4] | Fe–Fe [4] | Cu–Sb [1] | Cu–Sb [4] | $\alpha$ | $\beta$ |
| Experiment | 2.704(1) | 2.766(1) | 2.596(3) | 2.767(2) | 92.68(2) | 118.47(2) |
| Ref. [ [**?**]] | 2.693(1) | 2.782(2) | 2.660(3) | 2.784(2) | 93.86(5) | 117.80(3) |
| DFT-PBE | 2.72 | 2.77 | 2.69 | 2.77 | 91.98 | 118.86 |

the present experimental setup, $P_t$ has been measured in the ballistic regime. We calculated the spin-polarized DOS, which is shown in figure B.3 (c), along with the spin-polarized Fermi surface [figure B.3 (d) and (e)]. Similar to the non-magnetic case, the conduction electrons at the Fermi level have Fe-$d$ character. Further, $N_\uparrow(E_F)$ is found to be 12.6% larger than $N_\downarrow(E_F)$ for ferromagnetic CuFeSb. In addition to this imbalance in $N_\sigma(E_F)$, the average Fermi velocity $\langle v_F \rangle_\sigma$ contribute to $P_t$ in the ballistic regime. We find $\langle v_F \rangle_\uparrow > \langle v_F \rangle_\downarrow$, and the calculated average Fermi velocity for the up and down channel is $6.44 \times 10^5$ and $2.68 \times 10^5$ m/s, respectively. These result into a transport spin polarization, $P_t = 46\%$, which is in excellent agreement with the present Andreev reflection spectroscopy measurement.

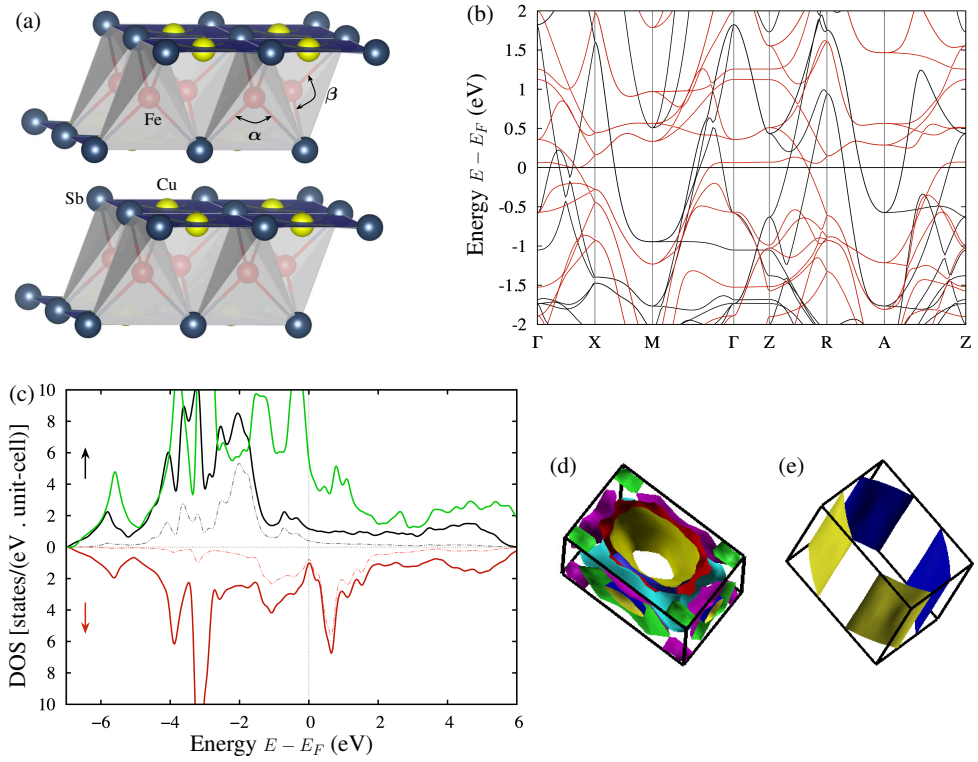


Figure B.3: (a) The crystal structure of CuFeSb showing tetragonal symmetry. (b) Calculated spin polarized band structure where black color indicates the bands corresponding to the up channel and red bands are corresponding to the spin-down channels. (c) The nonmagnetic (green line) and ferromagnetic DOS for CuFeSb. The spin-polarized Fermi surfaces are shown in (d) for up spin electrons and (e) for down spin electrons.

## B.4 Conclusions

In conclusion, we have measured the transport spin polarization of ferromagnetic CuFeSb. From the analysis of the Andreev reflection spectra we obtain a spin polarization of approximately 47%. The first principles calculations show that the spin polarization in the Fermi surface is approximately 12.5%. However, when the transport spin polarization is calculated including the role of significantly different Fermi velocities for the up and down spin bands respectively, the ballistic transport spin polarization is found to be 46% which is in excellent agreement with the experimental results. Furthermore, the band structure calculations shed light on the origin of a unique ferromagnetic ground state in CuFeSb as compared to the other compounds in the same family majority of which stabilize either in an antiferromagnetic or a superconducting ground state.

## B.5 Acknowledgements

In CuFeSb, theoretical calculations are provided by Chandan K. Singh and Dr. Mukul Kabir from IISER Pune. Samples are provided by Gohil S. Thakur and Prof. Ashok K. Ganguli from IIT Delhi.

# Bibliography


[1] A. Sirohi, et. al., Appl. Phys. Lett. **108**, 242411 (2016).

[2] F. Ma and Z.-Y. Lu, Phys. Rev. B **78**, 033111 (2008).

[3] V. Cvetkovic and Z. Tesanovic, Europhys. Lett. **85**, 37002 (2009).

[4] I. I. Mazin, Nature **464**, 183 (2010).

[5] M. J. Pitcher, D. R. Parker, P. Adamson, S. J. C. Herkelrath, A. T. Boothroyd, R. M. Ibberson, M. Brunelli, and S. J. Clarke, Chem. Comm. **45**, 5918 (2008).

[6] B. Qian, et. al., Phys. Rev. B **85**, 144427 (2012).

[7] G. S. Thakur, Z. Haque, L. C. Gupta and A. K. Ganguli, J. Phys. Soc. Jpn, **83**, 054706 (2014).

[8] C.-Y. Moonand, H. J. Choi, Phys. Rev. Lett. **104**, 057003 (2010).

[9] R. J. Soulen, Jr. et al., Science **282**, 85 (1998).

[10] S. Mukhopadhyay, P. Raychaudhuri, D. A. Joshi, and C. V. Tomy, Phys. Rev. B **75**, 014504 (2007).

[11] G. Sheet, S. Mukhopadhyay, and P. Raychaudhuri, Phys. Rev. B **69**, 134507 (2004).

[12] G. Kresse and J. Hafner, Phys. Rev. B **47**, 558 (1993).

[13] G. Kresse and J. Furthmüller, Phys. Rev. B **54**, 11169 (1996).

[14] B. Qian, et al., Phys. Rev. B **85**, 144427 (2012).

[15] C. -Y. Moon and H. J. Choi, Phys. Rev. B **104**, 057003 (2010).